

University of Tennessee, Knoxville
Trace: Tennessee Research and Creative Exchange

Doctoral Dissertations | Graduate School

12-2014

Neutron Scattering Studies of Phosphate Proton Conductors

Amal Bajes Al-Wahish
University of Tennessee - Knoxville, wahish@vols.utk.edu

This Dissertation is brought to you for free and open access by the Graduate School at Trace: Tennessee Research and Creative Exchange. It has been accepted for inclusion in Doctoral Dissertations by an authorized administrator of Trace: Tennessee Research and Creative Exchange. For more information, please contact trace@utk.edu.

To the Graduate Council:

I am submitting herewith a dissertation written by Amal Bajes Al-Wahish entitled "Neutron Scattering Studies of Phosphate Proton Conductors." I have examined the final electronic copy of this dissertation for form and content and recommend that it be accepted in partial fulfillment of the requirements for the degree of Doctor of Philosophy, with a major in Physics.

David Mandrus, Major Professor

We have read this dissertation and recommend its acceptance:

Takeshi Egami, Stephen E. Nagler, Janice L. Musfeldt, Marianne Breinig

Accepted for the Council:
Carolyn R. Hodges

Vice Provost and Dean of the Graduate School

(Original signatures are on file with official student records.)

Neutron Scattering Studies of Phosphate Proton Conductors

A Dissertation Presented for the

Doctor of Philosophy

Degree

The University of Tennessee, Knoxville

Amal Bajes al-Wahish

December 2014

© by Amal Bajes al-Wahish, 2014
All Rights Reserved.

Acknowledgements

I wish to express deep gratitude to my advisor Dr. Mandrus for giving me the freedom to perform this work on proton conductor materials, for his serious guidance, sincere encouragement and excellent research environments. Also I like to thank him for the wonderful opportunities to participate in several conferences, meeting and in particular neutron workshop at Institut Laue-Langevin, ILL, Grenoble France. I have learned from Dr. Mandrus to be strong independent researcher, have her own scientific ideas. It has been a pleasure working with him.

I am sincerely grateful to Dr. Herwig for his continuous support, guidance, encouragement, and endless hours with invaluable discussions, advice and remarks. He has been an excellent teacher, and a great, considerate and thoughtful person. For everything you've done, Dr. Herwig, I thank you.

I also owe my gratitude to Dr. Egami and Dr. Nagler for the valuable and constructive criticism, comments and suggestions during this research work. Their willingness to give their time so generously has been very much appreciated.

I would like to thank Dr. Breinig for endless support, excellent guidance, and encouragement. She is an outstanding teacher, thoughtful and patient person.

I like to thank Dr. Musfeldt for the training that I received from her within her group. Her knowledge and commitment to the highest standards inspired and motivated me.

I am grateful to my parents, Rasmyah Asaed and Bajes al-Wahish, for their support and love, may both rest in peace. I also want to thank my best friend,

my colleague, and my husband Usama al-Binni for all his support and help. I am very grateful to my daughter Leena al-Binni, she made me better a person.

At Oak Ridge national laboratory (ORNL), I would like to express my sincere gratitude to Dr. M. P. Paranthaman for hosting me in his group and lab and providing me with the resources to work in professional and efficient way.

I am deeply grateful to Dr. Craig Bridges for continuous support, invaluable discussions, positive criticism, comments and suggestions during our research collaboration.

My gratitude goes especially to Dr. Sorensen who encouraged and assisted me to overcome all the obstacles I faced through my first years at the physics department.I would like to thank Dr. Parks for his assistance and guidance in in the first two years I spent as teaching assistant at the physics department

I am very grateful to the University of Tennessee, Knoxville (UTK) that supported me over the years, specially the physics department. I thank the Center for Nanophase Materials Sciences (CNMS) and the Spallation Neutron Source (SNS) at Oak Ridge National Laboratory (ORNL) that provided me with a world-class scientific work environment, in that regard my gratitude goes especially to Niina Jalarvo, Zhonghe Bi, Souleymane Omar Diallo, Andrew Payzant, Jong Kahk Keum , Naveen Kumar Chogondahalli Muniraju, Melanie Kirkham and Rick Goyette. Also I would like to thank the National Institute of Standards and Technology and the neutron instrument scientists there for the fruitful neutron research experience, especially Dr. Craig Brown and Daniel Pajerowski.

Abstract

Proton ceramic fuel cells operating in the intermediate temperature range of $300 - 500°C$ offer potentially revolutionary advantages over existing fuel cells because expensive noble metal catalysts would not be needed, and in situ reforming of liquid bio-fuels such as ethanol or methanol would be possible. The chief obstacle facing intermediate fuel cells is the lack of a suitable electrolyte in the operating temperature range. A good electrolyte is thermally and chemically stable, inexpensive, environmentally friendly, and has a proton conductivity on the order of 10^{-2} S/cm [Siemens per centimeter] at 400°C. Acceptor-doped lanthanum orthophosphate is an attractive candidate electrolyte as it meets all of the above requirements except that its proton conductivity is 1-2 orders of magnitude too low. One of the motivations for the research presented here is to understand the microscopic mechanisms of proton transport in phosphate materials in order to suggest future synthetic approaches leading to higher performance materials. Proton transfer in orthophosphates is known to involve both localized and long-range diffusion, but the energetically favored pathways and rate limiting steps of the proton transport are not well understood. We investigated acceptor-doped lanthanum orthophosphate by means of quasi-elastic neutron scattering (QENS), neutron powder diffraction, X-ray diffraction, and electrochemical impedance spectroscopy (EIS). The conductivity of the hydrated sample was determined in the temperature range $500 - 850°C$ by EIS, and showed a clear proton-conductivity signature with activation energy of about 1.0 eV [electron volt]. The QENS experiment revealed a fast

dynamical process below 500°C that EIS did not observe. The fast proton diffusions activation energy is 0.09 eV in the temperature range from 150 to 500°C. We determined the proton mean jump length, mean residence time, atomic displacement, and self-diffusion coefficient in order to characterize the proton dynamics. This work presents the first QENS investigation of proton dynamics in a rare earth phosphate. This work has also led to the development of a new sample cell environment, allowing QENS measurements to be performed under a humid or dry gas flow. Thus materials can be studied under conditions approximating those inside an operational fuel cell.

Table of Contents

1 Introduction **1**

1.1 Motivation for and Organization of the Study 1

1.2 An overview of proton conducting in $LaPO_4$ materials 4

2 Fundamentals of Neutron Scattering **9**

2.1 Characteristics of neutrons 10

2.2 Neutron's wave-like behavior 12

2.3 Scattering length and scattering cross-sections 15

2.4 The effective Fermi pseudopotential 18

2.5 The intermediate scattering function 19

2.6 The van Hove correlation 19

2.7 The dynamic structure factor 21

3 Models of Diffusion **22**

3.1 Types of motion 22

3.2 Self-diffusion 23

3.3 Jump diffusion 25

3.3.1 Chudley and Elliott model (CE) 25

3.3.2 Singwi and Sjölander model (SS) 27

3.3.3 Hall and Ross model (HR) 28

4 Experimental **29**

4.1 Sample synthesis . . . 29
4.1.1 Solid state reaction . . . 30
4.1.2 Co-precipitation (CPT) . . . 31
4.2 X-ray powder diffraction (XRD) . . . 32
4.3 Scanning Electron Microscopy . . . 32
4.4 Thermogravimetric Analysis (TGA) . . . 32
4.5 Electrochemical Impedance Spectroscopy (EIS) . . . 33
4.6 Neutron Powder Diffraction (NPD) . . . 33
4.7 Quasi-elastic Neutron Scattering (QENS) . . . 35

5 Structure and Dynamics Investigation 37
5.1 X-ray diffraction (XRD) . . . 38
5.2 Neutron Powder Diffraction (NPD) . . . 45
5.3 Scanning Electron Microscopy (SEM) . . . 54
5.4 Electrochemical Impedance Spectroscopy (EIS) . . . 56
5.5 Quasi-elastic neutron scattering . . . 58

6 Quasi-Elastic Neutron Scattering Reveals Fast Proton Diffusion in Ca-doped $LaPO_4$ 60
6.1 Introduction . . . 60
6.2 Experimental . . . 63
6.3 Results and Discussion . . . 65
6.4 Conclusion . . . 81

7 Instrument design 82
7.1 Design Constraints . . . 83
7.1.1 Safety Regulations . . . 83
7.1.2 Risk of tightly sealed cans exploding inside the beam . . . 84
7.1.3 Multiple scattering . . . 85
7.1.4 Materials . . . 85

7.2 Sample cell design for dynamics measurements of proton conductor materials . . . 88
7.3 Sample holder . . . 88
7.4 Sample Cell . . . 89
7.5 Micas Furnace Generation I . . . 90
7.6 Portable Automated Gas Environment (PAGES) . . . 92
7.7 Experiment . . . 93
7.8 Discussion . . . 94
7.9 Summary . . . 97

8 Summary, Conclusions and Outlook **99**
8.1 Outlook . . . 103

Bibliography **105**

Vita **115**

List of Tables

2.1 The energies, wavelengths and temperatures of the cold, thermal and the hot neutrons. 12

2.2 Scattering lengths of hydrogen species and oxygen (all measured in barns). 17

5.1 The XRD cell parameters and cell volume for x%Sr/Ca-doped $LaPO_4$ ($x = 0, 1$, and 4.2) at room temperature. *$LaPO_4$ published Pearson's crystal data #383660. **$LaPO_4$ sample sintered at 1000°C; the remaining samples sintered at 1200°C. 41

5.2 The inter-ionic bond lengths (Å) between the phosphorus ions and the oxygen ions in the $LaPO_4$ samples from the XRD experiment at RT. Average bond lengths between the Lanthanum and oxygen ion as well as the distance between two phosphorus ions are listed for each sample. All the samples sintered at 1200°C, and the doped sample sintered under water vapor. 42

5.3 The NPD cell parameters and cell volume for x%Ca-doped $LaPO_4$ ($x = 0, 1$, and 4.2) at room temperature. 46

5.4 The inter-ionic bond lengths (Å) and angles (°) between the phosphorus ions and the oxygen ions in the $LaPO_4$ samples from the NPD experiment at 300 K. Average bond lengths between the Lanthanum and oxygen ion and the distance between the two phosphorus ions are listed for each sample. All the samples sintered at 1200°C. 47

5.5 The NPD cell parameters and cell volumes of $La_{0.958}Ca_{0.042}PO_4$ (D_2O) from $T = 18°C$ to 800°C under dry air. 47
5.6 The NPD cell parameters and cell volumes of $La_{0.958}Sr_{0.042}PO_4$ (H_2O) from $T = 60°C$ to 500°C under dry air. 47
5.7 $La_{0.958}Ca_{0.042}PO_4(D_2O)$ and $La_{0.958}Sr_{0.042}PO_4(H_2O)$ thermal expansion coefficients. 50
5.8 The inter-ionic bond lengths (Å) and angles (°) between the phosphorus ions and the oxygen ions in the 4.2% Ca-doped $LaPO_4(H_2O)$ samples from NPD experiment at elevated temperature from 18°C to 800°C. . 53
5.9 The inter-ionic bond lengths (Å) and angles (°) between the phosphorus ions and the oxygen ions in the 4.2%Sr-doped $LaPO_4(H_2O)$ samples from NPD experiment at elevated temperature from 60°C to 500°C. . 53
5.10 $La_{0.958}Ca_{0.042}LaPO_4$ (D_2O): x, y and z are fractional Atomic Coordinates and U is the equivalent isotropic displacement parameters ($Å^2$) at 18°C to 800°C. 55
5.11 $La_{0.958}Sr_{0.042}LaPO_4$ (H_2O): x, y and z are fractional Atomic Coordinates and U is the equivalent isotropic displacement parameters ($Å^2$) at 60°C to 500°C. 56
5.12 Hydrated and Dry $La_{0.958}Ca_{0.042}LaPO_4$ at 300 K: x, y and z are fractional Atomic Coordinates and U is the equivalent isotropic displacement parameters ($Å^2$). 57

6.1 The fit model parameters result from the first approach. The mean residence time τ(ps), mean jump distance ℓ(Å), self-diffusion coefficient $D(10^{-5}cm^2/s)$ and the activation energy E_a (eV), are listed respectively. The Q^2-dependence of the half-width-at-half-maximum (HWHM) of the Lorentzians was obtained by fitting with the isotropic Chudley-Elliott model for $T = 150, 250, 350$, and 500°C.) 76

6.2 The fit model parameters result from the second approach, the mean residence time τ(ps), mean jump distance ℓ (Å), the mean-square displacement $\langle u^2 \rangle^{1/2}$ (Å), self-diffusion coefficient $D(10^{-5}\text{cm}^2/\text{s})$ and the activation energy E_a(eV), are listed respectively. The isotropic Chudley-Elliott model directly fit to the measured $S(\vec{Q}, \omega)$. This method fit all the Q-spectra at a given temperature simultaneously, including their intensity as normalized to the vanadium standard. . . 76

7.1 presents scattering cross-sections (Dianoux and Lander (2003)) and Bragg cut-off wavelength (Gražulis et al. (2012); Gražulis et al. (2009); Downs and Hall-Wallace (2003)) of typical materials used in sample environments. 83

7.2 General specification for Micas Furnace Generation I 91

List of Figures

1.1 Schematic of a possible migration path for protons between tetrahedra (inter-tetrahedral) in $LaPO_4$. Reproduced from Yu and Jonghe (2007). 8

2.1 Typical view of a neutron scattering experiment's kinematics in real space (left) and in reciprocal space (right). 13

5.1 Left: the unit cell of $LaPO_4$ which has a monoclinic $P2_1/n$ structure containing four formula units,. The unit cell contains La^{3+} cations (yellow) and isolated PO_4 tetrahedra (O in grey and P in blue). Right: La^{3+} coordination polyhedra associated with nine oxygen ions. 38

5.2 Rietveld refinement results obtained from the X-ray powder diffraction data for hydrated $La_{0.958}Sr_{0.042}PO_4$ (no background subtraction) and $La_{0.99}Sr_{0.01}PO_4$ (after background subtraction) sintered at 1200°C. The XRD pattern at room temperature was conducted at the CNMS User Facility at ORNL. 39

5.3 Rietveld refinement results obtained from the X-ray powder diffraction data for hydrated $La_{0.958}Ca_{0.042}PO_4$ (no background subtraction) and $La_{0.99}Ca_{0.01}PO_4$ (after background subtraction) sintered at 1200°C. The XRD pattern at room temperature was conducted at the CNMS User Facility at ORNL. 40

5.4 Rietveld refinement results obtained from the X-ray powder diffraction data for $LaPO_4$ at room temperature. The XRD pattern was conducted at the CNMS User Facility at ORNL. 41

5.5 (a) Orthophosphate $[PO_4]^{3-}$ where the average calculated P−O, P−P, and La−O length is 1.564 Å, 4.187 Å, and 2.621 Å, respectively. (b) Pyrophosphate group $[P_2O_7]^{4-}$ in the doped $LaPO_4$ showing bridging oxygen ion (Ob) and P−Ob and P−P bond lengths around 1.718 Å and 3.175 Å, respectively. (c) Protonated orthophosphate group $[HPO_4]^{3-}$ in $LaPO_4$ also showing the P−O bond lengths up to 1.882 Å and that of $P-P_{adj}$ to be 4.179 Å. Reproduce from Phadke et al. (2012). . . . 44

5.6 Rietveld refinement results obtained from the neutron powder diffraction data for hydrated $La_{0.958}Ca_{0.042}PO_4$ (D_2O) at 18, 35, 500, and 800°C. The NPD patterns were conducted at POWGEN, SNS at ORNL. 48

5.7 Detailed temperature dependence of the lattice constants for $La_{0.958}Ca_{0.042}PO_4$ (D_2O). $\Delta x/x_0$ is $[x(T) - x_0(T = 291\ \mathrm{K})]/\mathrm{x_0(T = 291\ K)}$ where $x = a(\text{Å}), \mathrm{b(Å)}, \mathrm{c(Å)and V(Å^3)}$ for (a), (b), (c) and (d) respectively. The Thermal expansions are linear for cell parameters in the temperature range from RT to 800°C. 49

5.8 Detailed temperature dependence of the lattice constants for $La_{0.958}Sr_{0.042}PO_4$ (H_2O). $\Delta x/x_0$ is $[x(T) - x_0(T = 333\ \mathrm{K})]/\mathrm{x_0(T = 333\ K)}$ where $x = a(\text{Å}), \mathrm{b(Å)}, \mathrm{c(Å)and V(Å^3)}$ for (a), (b), (c) and (d) respectively. The Thermal expansions are linear for cell parameters in the temperature range from 60°C to 500°C. 50

5.9 Rietveld refinement results obtained from the neutron powder diffraction data for hydrated $La_{0.958}Sr_{0.042}PO_4$ (H_2O) at 60, 70, 180, and 260°C. The NPD patterns were conducted at POWGEN, SNS at ORNL. 51

5.10 Rietveld refinement results obtained from the neutron powder diffraction data for hydrated $La_{0.958}Sr_{0.042}PO_4$ (H_2O) at 360 and 500°C. The NPD patterns were conducted at POWGEN, SNS at ORNL. 52

5.11 The SEM images for (a) $LaPO_4$, (b) 4.2% Ca-doped $LaPO_4$, (c) 4.2% Sr-doped $LaPO_4$. 55
5.12 Conductivities of the $La_{0.958}Sr_{0.042}PO_4$ and $La_{0.958}Ca_{0.042}PO_4$ in dry and wet (2.2 mol% water content) air. 58
5.13 The diffusion (in log scale) of EIS measurement (blue symbols) and QENS measurement (red symbols) for 4.2%Ca-doped $LaPO_4$. 59

6.1 The unit cell of $LaPO_4$, which has a monoclinic $P2_1/n$ structure. The unit cell contains La^{3+} cations (blue) and isolated PO_4 tetrahedra (O in red and P in yellow). 66
6.2 Rietveld refinement results obtained from the X-ray powder diffraction data for hydrated $La_{0.958}Ca_{0.042}PO_4$ at room temperature. The XRD pattern was recorded on a Bruker AXS D2 Phaser diffractometer. . . 66
6.3 Morphology of the $LaPO_4$ sample (a) and 4.2% Ca-doped $LaPO_4$ (b) sintered at 1200°C. The bar scale in both SEM images represents 2 μm. 67
6.4 TGA data for $La_{0.958}Ca_{0.042}PO_4$ under dry and wet Ar atmospheres. The large hysteresis indicates the clear absorption of H_2O under wet atmosphere. 69
6.5 AC impedance spectra for 4.2% Ca-doped $LaPO_4$ in wet and dry air at 550°C. 70
6.6 Conductivities of the $La_{0.958}Ca_{0.042}PO_4$ in dry and wet (2.2 mol% water content) air. 72
6.7 Quasi-elastic spectra collected from the hydrated sample at a momentum transfer of 0.3 $Å^{-1}$ and $T = 150$°C. Symbols are the experimental data and the purple solid line is the total fit. The gray, aqua, and the pink solid lines are the background, delta, and Lorentzian components convoluted with energy resolution function of the instrument, respectively as described in Equation 6.7 in the text. 73

6.8 Scattering intensities (linear scale) collected on BASIS for 4.2% Ca-doped $LaPO_4$ for hydrated (color symbols) for $Q = 0.3, 0.5, 0.7$, and 0.9 Å^{-1} and for $T = 150, 250, 350$, and 500°C. For reference, the signal from the dehydrated sample is shown at $T = 150$°C. 74

6.9 The difference spectra between the "wet" and "dry" sample conditions. Symbols are data at the indicated Q-values and temperatures of 150°C (left panels) and 350°C (right panels). Solid lines are Lorentzian fits to the data. The data near the elastic ($\omega = 0$) region were suppressed and not fit due to the imperfect subtraction of the very large elastic signal from the immobile atoms in the crystal structure. 75

6.10 Q^2-dependence of the half-width-at-half-maximum (HWHM), symbols, of the Lorentzians obtained by fitting our QENS spectra with the isotropic Chudley-Elliott model, solid lines, for $T = 150, 250, 350$, and 500°C. 77

6.11 Chudley-Elliott diffusion model parameters derived from single-Lorentzian fits to the data: (a) mean jump distance, (b) and (c) are Arrhenius plots of the mean residence time and self-diffusion coefficient, respectively. . 78

6.12 Chudley-Elliott diffusion model parameters derived from direct fits to $S(\vec{Q}, \omega)$: (a) mean jump distance, (b) and (d) are Arrhenius plots of the mean residence time and self-diffusion coefficient, respectively, and (c) the mean-square displacement $\langle u^2 \rangle^{1/2}$ (Å) of the Debye-Waller factor. 79

6.13 Oscillatory proton transfer O1 $\longleftrightarrow$ O4, O3 $\longleftrightarrow$ O1, and O4 $\longleftrightarrow$ O3 with low potential barriers ≤ 0.09 eV, and jump length $\ell = 0.6, 0.46,$ and 0.41 Å respectively. Rotational migration paths are around O2, O3, and O4 with activation energy 0.05 eV $\leq E_a < 1$ eV. Inter-tetrahedral hopping paths such as: O3→O1 with $\ell \approx 2.35$ Å and 0.2 eV, O1→O1 with $\ell \approx 1.96$ Å, and 0.16 eV, O1→O4 with $\ell \approx 2.78$ Å and 0.26 eV. O2→O4 with $\ell \approx 1.89Z$Å and 0.13 eV. The mean jump lengths determined from X-ray Retrieved refinement. The mean jump lengths are correlated to the activation energies from Ref.11. Illustrated by using visualization for electronic and structural analysis software (vesta). 80

7.1 (a) The quartz tube. The Pt sample holder connected by inner quartz tube and surrounded by outer quartz tube. (b) The sample cell tube assembly installed in MICAS vacuum furnace at SNS sample environment. 84

7.2 Sample cell connected to PAGES. PAGES system is designed to deliver gas to the sample cell via three separate gas channels. 86

7.3 Niobium embrittled by water 87

7.4 (a) The sample holder is composed of three main parts; inner Pt tube wall, Pt outer wall, and quartz sample stick. The polycrystalline sample is held in the annular cylindrical geometry can. A thermocouple is around the sample to measure the equilibrium temperatures. (b) Sample holder shown in quartz tube. 89

7.5 The PAGES system is connected with three separate gas channels. These channels deliver gas to the sample cell. 92

7.6 Neutron scattering intensities (log scale) collected at BASIS for the quartz tube and the furnace at room temperature, empty Pt sample holder at 500°C and Vanadium inside the Pt sample holder at 35°C for $Q = 0.5$ Å^{-1}. No clear quasi-elastic component appears. 95

7.7 Neutron scattering intensities (linear scale) collected at BASIS for the Vanadium inside the Pt sample holder at room temperature (black line) and the empty sample holder in the gas flow system (color symbols) for $Q = 0.5, 0.7, 0.9$, and 1.3 Å^{-1} and for the temperature window from $T = 150$ to 900°C. No clear quasi-elastic component appears. The sample holder's stability is shown at elevated temperature. 96

7.8 Neutron scattering intensities (linear scale) collected at BASIS for Vanadium inside the Pt sample holder at room temperature (black line) and the empty Pt sample holder in the gas flow system (color symbols) under dry and wet He, for $Q = 0.5, 0.7, 0.9$, and 1.1 Å^{-1} at 250°C. No difference is seen between wet and dry He in the neutron signal. 97

7.9 Quasielastic spectra (log scale) collected at BASIS for the Vanadium at room temperature (black symbols), the hydrated/dehydrated 4.2%Ca-doped $LaPO_4$ sample, (cyan symbols)/(blue symbols), inside the Pt sample holder in the gas flow system under humid He/Dry He, for $Q = 0.5, 0.7, 0.9$, and 1.1 Å^{-1} at 250°C. The dark-blue solid line is the total fit. The pink, golden, and cyan solid lines are background, delta, and Lorentzian components convoluted with the instrument's energy resolution function. 98

Chapter 1

Introduction

1.1 Motivation for and Organization of the Study

High temperature proton conducting electrolytes have great potential for being useful for a variety of energy-related applications, including fuel cells, batteries, gas sensors, hydrogen pumps, and electrolyzers Burggraaf and Cot (1996). The most heavily studied materials are acceptor-doped Sr and Ba containing perovskites, which are good proton conductors at very high temperatures Steele and Heinzel (2001). Proton ceramic fuel cells (PCFCs) operating in the intermediate temperature range of 300-500°C offer potentially revolutionary advantages over existing fuel cells because expensive noble metal catalysts would not be needed and *in situ* reforming of liquid bio-fuels such as ethanol or methanol would be possible Phadke et al. (2012); Haile et al. (2001); Malavasi et al. (2010). The chief obstacle facing intermediate fuel cells is the lack of a suitable electrolyte in the operating temperature range. A good electrolyte is thermally and chemically stable, inexpensive, environmentally friendly, and has proton conductivity on the order of 10^{-2} S cm^{-1} at 400°C. Rare earth phosphates are an attractive class of materials because they fulfill most of these requirements, and are known to conduct protons in the operating temperature range.

If the proton conductivity of phosphates could be raised by 1-2 orders of magnitude, they would become viable materials for applications.

Hydrogen is incorporated into rare earth phosphates ($REPO_4$ with RE = the rare-earth ions, e.g., La, Nd, Ce) by first replacing a fraction of the trivalent rare earth with a divalent ion such as Ca, Sr, or Ba to create oxygen defects Norby and Christiansen (1995); Amezawa et al. (2005). When the material is heated in a moist atmosphere, oxygen from the water molecules fills the defects while simultaneously introducing two protons into the system. These protons cannot occupy lattice or interstitial sites, but are always embedded in an oxygen ion's electron cloud, forming hydroxide defects Kreuer (2003). Although protons were first thought to be transported via hydroxide ions, protons are now known to migrate in some materials as lone protons hopping between relatively stationary oxygen ions Cukierman (2006). Proton motion is believed to involve both localized diffusion and proton transfer. The limiting steps of the transport rate are not well understood, especially considering that quantum fluctuations have recently been shown to have a large effect on the transfer barrier Kreuer et al. (2004); Vuilleumier et al. (1998); Tuckerman et al. (1997).

Incoherent quasi-elastic neutron scattering (QENS) is a promising technique to probe diffusive motions in the 10^{-12} to 10^{-9} sec time range at length scales from $\sim$ 3 Å to 60 Å. These are the time and length scales of relevance to the diffusion of hydrogen ions and hydrogenous species. The very high neutron cross section of protons emphasizes their neutron scattering signal and enables studies of systems with relatively few protons, such as the one considered here. BaSiS, the highest resolution spectrometer at the SNS, has already been used to probe similar dynamic processes in room-temperature ionic liquids in bulk liquid and solid phases Mamontov et al. (2009). These measurements exploited the unique capability of BaSiS to measure both slow and rapid processes simultaneously. A small number of QENS experiments have been conducted on proton conducting oxides Karmonik et al. (1995); Matzke et al. (1996); Karmonik et al. (1996); Pionke et al. (1997); et al. (2009); Braun et al. (2009); Wilmer et al. (2007); Karlsson et al. (2009), and recently even spin echo has

been investigated Karlsson et al. (2010). QENS experiments are suitable to study diffusion of elements with sufficient incoherent scattering cross section for neutrons. Probing hydrogen diffusion in materials is especially suitable since hydrogen has the largest incoherent scattering cross section.

The goal of this study is to contribute to the understanding of phosphate proton conductors by studying the proton dynamic properties using QENS and electrochemical impedance spectroscopy (EIS) measurements.

This work is organized into three main sections. The first section explores the structure and defect structure of aliovalent (Sr, Ca) doping on $LaPO_4$ materials using neutron powder diffraction (NPD) and X-ray diffraction (XRD). The second section studies proton dynamic properties using QENS and electrochemical impedance spectroscopy (EIS) measurements. The last section presents the instrument sample cell design for Quasi-elastic measurement at BaSiS that was built specifically for this work.

In Chapter 1 we review some of the studies of $LaPO_4$ and present motivation for the present study. Chapter 2 is a theoretical introduction to the neutron scattering and the quasi-elastic neutron scattering (QENS). Chapter 3 presents a brief overview of motion types and diffusion models. Following that, Chapter 4 covers the sample synthesis and characterization using XRD, SEM, TGA EIS, NPD, and QENS. Then Chapter 5 analyzes data from the XRD, NPD and EIS experiments for Ca and Sr. Chapter 5 corresponds to an article in preparation. Chapter 6 introduces QENS experiment on 4.2% Ca-doped $LaPO_4$. Chapter 6 is an article that has been accepted for publication in The Journal of Physical Chemistry Part C: Quasi-Elastic Neutron Scattering Reveals Fast Proton Diffusion in Ca-doped $LaPO_4$. Chapter 7 is an account of the instrument design for the sample cell. Chapter 7 is an article that will be submitted for publication to the review of scientific instrument journal. Chapter 8 ends this work with conclusions, and outlook.

1.2 An overview of proton conducting in $LaPO_4$ materials

Proton conductor materials are considered alternative electrolyte materials for solid oxide fuel cells (SOFCs). When comparing their oxygen-ion conducting performance, proton-conducting fuel cells (PCFCs) offer higher thermodynamic efficiency with hydrogen-rich fuels. Ideally, electrolytes in fuel cells should display proton conductivity with no electronic and minimum ionic conductivity, along with long-term chemical and thermal stability. Phosphates, such as $LaPO_4$ materials, when hydrated under post-annealing-formed proton conductors are promising for future electrolytic fuel cells.

Protons in proton conductor materials are not intrinsic; the formation of protonic defects needs oxygen-ion vacancies. Creating oxygen vacancies on $LaPO_4$ can be done by changing the stoichiometry through doping, such as aliovalent (Sr, Ca) doping on $LaPO_4$ materials to have $La_{1-x}Sr_xPO_{4-x/2}$ and $La_{1-x}Ca_xPO_{4-x/2}$, respectively. Doping Ca^{2+}/Sr^{2+} (divalent atom) on the La^{3+} (trivalent atoms) affects the charged concentrations. The charges can be compensated in many ways. The oxygen-ion vacancies, $V_O^{\bullet\bullet}$, in the dry atmosphere compensate the dopants Norby and Christiansen (1995). When the sample is exposed to humid atmosphere after annealing, the charge compensation is obtained by creating protonic defects. Using the Kröger-Vink notation, this reaction can be expressed as

$$H_2O_{\,(g)} + V_O^{\bullet\bullet} + O_O^{\times} \rightleftharpoons 2\,OH_O^{\bullet} \tag{1.1}$$

$$K = \exp\frac{\Delta S^{\circ}}{R}\exp\frac{-\Delta H^{\circ}}{RT} \tag{1.2}$$

$$K = \frac{[OH_O^{\bullet}]^2}{P_{H_2O}[V_O^{\bullet\bullet}][O_O^{\times}]} \tag{1.3}$$

where $O_O^{\times}$ is oxygen sitting on an oxygen lattice site with a neutral charge, $V_O^{\bullet\bullet}$ is an oxygen vacancy, with double positive charge, $OH_O^{\bullet}$ is a protonic defect in the oxygen

site, with single positive charge, K is the equilibrium coefficient of the reaction, R is the gas constant, T is the absolute temperature, p_{H_2O} is the vapor pressure, and ΔS° and ΔH° are the standard entropy and enthalpy changes, respectively, for the reaction over the investigated temperature range.

At an elevated temperature, the water in the gas phase separates into a hydroxide ion and a proton; the hydroxide ion OH' occupies interstitially the oxygen vacancy to form a protonic defect in the form $OH_O^\bullet$, and the proton forms a covalent bond with a lattice oxygen. The formed protonic defect is two positively charged $OH_O^\bullet$ Kreuer (2003). According to Shin and Sata, infrared absorption spectra indicate that the crystal structure's oxygen ions bond protons in interstitial sites. These researchers found that the O−H stretching vibration frequency is about 3500 cm^{-1} in the perovskite-type protonic conductors. It is less than the O−H stretching vibration in the H_2O molecule by 300 to 1000 cm^{-1}. The O−H stretching vibration frequency in undoped samples is the same as that in the H_2O molecule Shin and Crystal (1990); Sata et al. (1996). The proton bonds covalently with one oxide ion, and the resulting hydrogen bonds with another oxygen ion in the crystal structure. The hydrogen bond facilitates the proton mobility in many proton conductors. The charge defects may diffuse in the oxide conductor materials when there are oxygen vacancies $V_O^{\bullet\bullet}$. The diffusion of $V_O^{\bullet\bullet}$ and $OH_O^\bullet$ may lead to ionic conductivity, which can be very useful in many application such as fuel cells. The electroneutrality conditions are

$$2[V_O^{\bullet\bullet}] + [OH_O^\bullet] = [Ca'] = \text{const} \quad \text{or} \quad 2[V_O^{\bullet\bullet}] + [OH_O^\bullet] = [Sr'] = \text{const} \tag{1.4}$$

The parentheses denote volume concentration. At a low temperature, the charges are mainly compensated by protons, which are best described by the following:

$$[OH_O^\bullet] = [Ca'] = \text{const} \quad \text{or} \quad [OH_O^\bullet] = [Sr'] = \text{const} \tag{1.5}$$

Based on equations 1.2 and 1.3, the proton concentration can be determined as

$$[OH_O^{\bullet}] = [O_O^{\times}]^{1/2}[V_O^{\bullet\bullet}]^{1/2} p_{H_2O}^{1/2} \exp\frac{\Delta S^{\circ}}{2R} \exp\frac{-\Delta H^{\circ}}{2RT} \tag{1.6}$$

Norby and Christiansen (1995) doped 5% aliovalent (Sr, Ca) on lanthanum orthophosphate ($LaPO_4$), and they investigated the conductivity as a function of temperature and water vapor partial pressure. The proton conductivity at 800°C in humid air was found to be approximately 3×10^{-4} and 6×10^{-5} S/cm for $La_{0.95}Sr_{0.05}PO_4$ and $La_{0.95}Ca_{0.05}PO_4$, respectively. Protons are the major charge carriers under humid atmosphere with maximum proton conductivity at 950°C and 850°C when the dopant is Ca and Sr, respectively. Above 950°C, the protons escape from the sample, the proton concentration decreases, and the oxygen vacancies govern the conductivity Norby and Christiansen (1995). Equation 1.4 then reduced to

$$2[V_O^{\bullet\bullet}] = [Ca'] = \text{const} \quad \text{or} \quad 2[V_O^{\bullet\bullet}] = [Sr'] = \text{const} \tag{1.7}$$

Norby and Christiansen (1995) concluded that the 5% Sr-doped $LaPO_4$ has higher conductivity compared to the 5% Ca-doped LaPO4 and that the mobile proton's activation energy is around 0.8 eV.

Amezawa et al. (2001) investigated the proton conduction and defect structures in Sr-doped $LaPO_4$ by using conductivity, MAS-NMR spectroscopy, and FT-Raman spectroscopy measurements. According to these researchers' model, oxygen vacancies resulting from doping of Sr/Ca in the monazite-type lanthanum orthophosphate, $LaPO_4$, may lead to the formation of pyrophosphate-type defects $(P_2O_7)_{2PO4}^{\bullet\bullet}$. The signature of P_2O_7 was noticed in the Sr-doped $LaPO_4$ as a result of Fourier transform Raman and magic-angle spinning nuclear magnetic resonance (MAS-NMR) spectroscopy experiments. When hydrating the pyrophosphate by post-annealing under water vapor, protons dissolve into phosphates, forming hydrogen phosphate$(HPO_4)_{PO4}^{\bullet}$. As a result, protons remain PO_4 tetrahedra in the sample.

The material's proton concentration $[(HPO_4)^{\bullet}_{PO4}]$ depends on the dopant $[Ca'_{La}]$ and on the concentration of oxygen defects $[(P_2O_7)^{\bullet\bullet}_{2PO4}]$ and is described as

$$[(HPO_4)^{\bullet}_{PO4}] + 2[(P_2O_7)^{\bullet\bullet}_{2PO4}] = [Ca'_{La}] \tag{1.8}$$

The proton content inside the sample also depends on the partial pressure of water $p(H_2O)$. Amezawa et al. (2005) reported that if the oxygen vacancies are dominant defects, the proton concentration should be proportional to $p(H_2O)^{1/2}$.

The theoretical study by Toyoura et al. (2012) of the proton conduction mechanism in $LaPO_4$ used a first-principles approach that supports proton preferential binding to sites around PO_4 tetrahedral. This study determined the energetically favorable proton sites around PO_4 tetrahedra in the crystal. Yu and Jonghe (2007) also investigated the proton-transfer mechanism in $LaPO_4$ based on density functional calculations. Since the low symmetry of $LaPO_4$ allows many possible computed transfer paths, these researchers considered the following classical proton-transfer paths: rotation around an oxygen ion, oscillatory motion between adjacent tetrahedra, transfer between oxygen ions within a single PO_4 tetrahedron (intra-tetrahedral), and jumps between tetrahedra (inter-tetrahedral) are presented in Figure 1.1. The study concluded that the intra-tetrahedral process is forbidden and that the inter-tetrahedral transfer with 0.6-1.0 eV potential barriers is the dominant proton-transfer process. The energy barrier for the forward or backward proton transfer mechanism between two adjacent PO_4 is below 0.1 eV. The interactions among an aliovalent cation dopant, Sr/Ca, and protons in $LaPO_4$ were not studied.

Further theoretical theoretical studies by Toyoura et al. (2012) and Adelstein et al. (2012) considered the aliovalent dopant's effect, which caused a wider range of activation energy barriers for proton transfer.

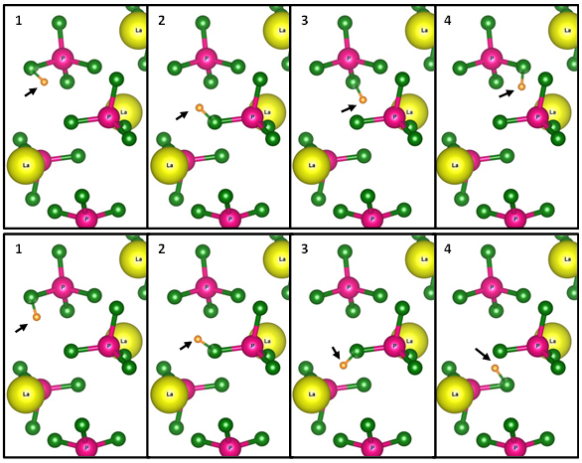


Figure 1.1: Schematic of a possible migration path for protons between tetrahedra (inter-tetrahedral) in $LaPO_4$. Reproduced from Yu and Jonghe (2007).

Chapter 2

Fundamentals of Neutron Scattering

The impact of aliovalent (Sr, Ca, Ba) doping on proton conductor lanthanum orthophosphate ($LaPO_4$) materials have been investigated experimentally in a number of macroscopic scale studies, mostly using electrochemical impedance spectroscopy (EIS), like Amezawa et al. (2001); Kitamura et al. (2005); Norby (2001).

A less commonly used but powerful technique is Quasi-elastic Neutron Scattering (QENS), which studies incoherent neutron scattering intensity between Bragg peaks, helps in understanding the dynamics of proton conductors. Incoherent scattering results from incompetent of the scattered neutron (neutron scattered from the nuclei of the sample) to interfere with each other. Thus the incoherent scattering contains important information (including geometrical information) about the single-particle dynamic inside the sample. It links correlations between the site $\vec{R}_i(0)$ of a single-particle at time zero and site $\vec{R}_i(t)$ of the same single-particle at time t. At adequate temperature the particles put through a stochastic motion (long-range diffusion, rotational). The transfer energy (gain or loss) between the neutrons and particles in each scattering event measured and recorded in the spectrum (where the x-axis is the energy transfer and the y-axis is the neutron scattering intensity). The spectrum

is broadened due to the diffusion process and the maximum of the elastic spectrum is centered at zero. However, the coherent scattering results from the interference between a scattered single neutron waves (the single neutron scattered from all the nuclei in the sample), where the scattering intensity is a function of the scattering angle. The coherent scattering gives correlations between the site of an atom, i, $\vec{R}_i(0)$ at time zero and the site $\vec{R}_j(t)$ of any atom, j, at time t. Embs et al. (2010) have reported that for cold and thermal neutrons, the wavelength and kinetic energy are similar to interatomic distances and excitation energies in solid materials, respectively. To determine proton diffusion on atomic scales of space and time simultaneously, the region of the 10^{-12} to 10^{-9} sec time range is penetrated at length scales from $\sim$ 3 Å to 60 Å. Information about single-particle dynamics, such as for a proton, can be obtained. This information includes stochastic dynamic motion, long-range diffusion, and rotation locale motion. QENS intensities are measured as a function of momentum and energy transfer. QENS experiments are suitable for studying element diffusion with sufficient incoherent scattering cross section for neutrons. Such experiments are especially suitable for probing hydrogen diffusion in materials, since hydrogen has the largest incoherent scattering cross section.

The following chapter presents an outline of fundamentals and the theoretical background of neutron scattering. A more detailed description can be found in the literature: Roe (2000); Squires (1978); Lechner (1983); Lovesey (1984); Bée (1988); Hempelmann (2000); Embs et al. (2010).

2.1 Characteristics of neutrons

A very effective technique for analyzing molecular dynamics, neutron scattering spectroscopy provides information about molecular motion on space-time correlation functions at the molecular level. The average energy related to molecules vibration and to molecules rotational and translation motion can be estimated by k_BT, where

k_B is Boltzmann's constant. The ambient temperature energy of the typical thermal neutron is approximately 20 meV.

Because neutrons have zero charge, with a mass equal to 1.675×10^{-24}g and spin 1/2, they can deeply penetrate matter with little nucleon interaction. The diameter of the nucleus is on the order of 10^{-15}m (for hydrogen it is 1.75×10^{-15}m). Neutrons consider the solid matter as essentially an empty space to travel through because the size of the nucleus (the size of the scattering domain) is 10^5 times smaller than the distance between the centers. The scattered neutrons detect the change of the atomic motion when neutrons inelastically scatter off matter and energy transfers between the motion of atoms and neutrons. That energy transfer can provide information about specific atom dynamics. For example, the time of the thermal neutron wave period and the atomic motion time period are the same, on the order of 10^{-12}s.

The neutron kinetic energy E and momentum p are

$$E = \frac{1}{2}mv^2 \tag{2.1a}$$

and

$$\vec{p} = m\vec{v} \tag{2.1b}$$

where v is the neutron velocity. Neutron sources used for the scattering experiments are nuclear reactors or spallation sources. This present work was done at the Spallation Neutron Source (SNS) facility at Oak Ridge National Laboratory (ORNL), where high-energy protons strike liquid mercury atom nuclei inside the target vessel. Approximately 20 to 30 neutrons result from this process. Neutron pulses are slowed through several collisions with atoms in the moderated materials, which are located above and below the target. The neutron velocity spectrum in the moderator approaches the Maxwell-Boltzmann distribution in a gas at equilibrium, where the

Table 2.1: The energies, wavelengths and temperatures of the cold, thermal and the hot neutrons.

	Cold Neutrons (Range)/Typical values	Thermal Neutrons (Range)/Typical values	Hot Neutrons (Range)/Typical values
Energy (meV)	(0.1-10.0)/2.2	(5.0-100.0)/28.4	(100.0-500.0)/172.0
Wavelength (Å)	(4.0-30.0)/6.2	(1.0-4.0)/1.7	(0.4-1.0)/0.7
Temperature (K)	(1.0-120.0)/25.0	(60.0-1000.0)/330.0	(1000.0-6000.0)/2000.0

distribution reaches its maximum at

$$v = \left(\frac{2k_BT}{m}\right)^{1/2} \tag{2.2}$$

The neutron average thermal energy is

$$E = \frac{3}{2}k_BT \tag{2.3}$$

Neutrons slowed by the heavy water (D_2O) at 330 K are called thermal neutrons, while neutrons slowed by passing through liquid hydrogen at 20 K are called cold neutrons. The energies, wavelengths and temperatures of the thermal and the cold neutrons are listed in Table 2.1. Neutrons guided through beam lines lead directly to instrument stations for conducting experiments.

2.2 Neutron's wave-like behavior

A Neutron has an associated de Broglie wavelength λ and, and therefore behaves as a wave according to the de Broglie relation:

$$\lambda = \frac{h}{p} = \frac{2\pi}{|\vec{k}|} \tag{2.4}$$

The plane wave, $\exp(i\vec{k}\cdot\vec{r})$, describes the neutron before scattering, and the spherical wavefront, $-\frac{b}{r}\exp(i\vec{k}\cdot\vec{r})$ Neutron calculations are generally treated as weakly interacting Born approximations, which in general simplify the calculations. The

Born approximation states that the probability of a neutron wave with wavevector $\vec{k}_1$ to change into an outgoing wave of wavevector $\vec{k}_2$ after being scattered by a nuclear interaction potential $V(\vec{r})$ is proportional to the following factor over the sample volume:

$$\left| \int e^{-i\vec{k}_1 \cdot \vec{r}} V(\vec{r}) e^{i\vec{k}_2 \cdot \vec{r}} d\vec{r} \right|^2 = \left| \int e^{i\vec{Q} \cdot \vec{r}} V(\vec{r}) d\vec{r} \right|^2 \tag{2.5}$$

When matter scatters neutrons, the process can change their momentum and energy. When neutron energy is written as

$$E = \frac{(\hbar k)^2}{2m_n}, \tag{2.6}$$

the energy transfer $\hbar\omega$ is then given by:

$$\hbar\omega = E_2 - E_1 = \frac{\hbar^2}{2m_n}(k_2^2 - k_1^2) \tag{2.7}$$

where E_1 is the incident neutron energy, and E_2 is its final energy after scattering. As for momentum transfer $\vec{Q}$ of the neutron, it is given in terms of the neutron's initial

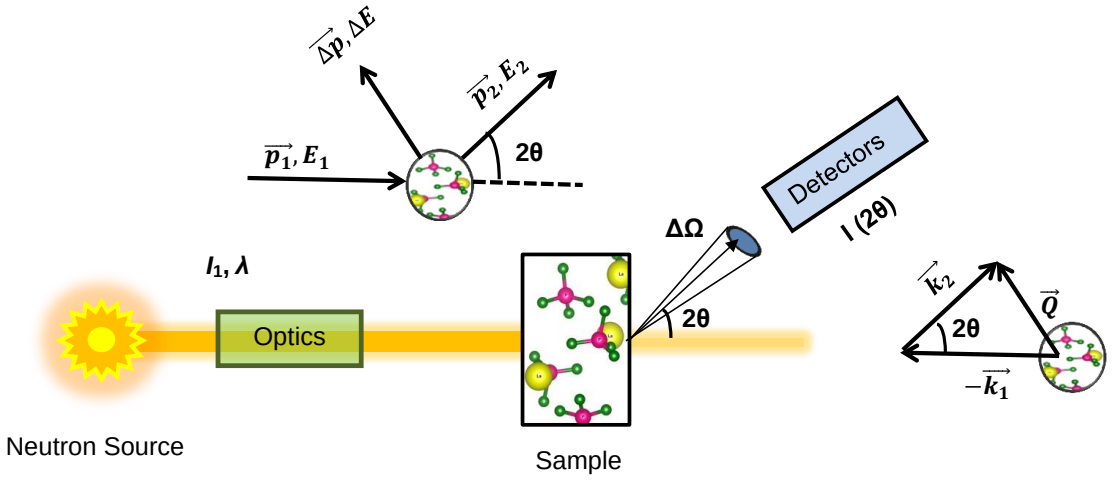


Figure 2.1: Typical view of a neutron scattering experiment's kinematics in real space (left) and in reciprocal space (right).

$\vec{k}_1$ and final $\vec{k}_2$ wave vectors:

$$\vec{Q} = \vec{k}_2 - \vec{k}_1 \tag{2.8a}$$

$$Q^2 = k_1^2 + k_2^2 - 2k_1 k_2 \cos\theta \tag{2.8b}$$

In the elastic neutron scattering the momentum transfer value is $Q = (4\pi/\lambda)\sin\theta$ (λ is the neutron's wavelength, and θ is the scattering angle). Neutron scattering can be elastic, inelastic, or quasi-elastic, depending on the interactions between the neutrons and the atoms. The scattering is called *elastic* when no change occurs in the neutron energy:

$$\hbar\omega = E_2 - E_1 = 0 \tag{2.9}$$

or *inelastic* when

$$\hbar\omega = E_2 - E_1 \neq 0 \tag{2.10}$$

When the transfer energy is near zero, it is called quasi-elastic neutron scattering (QENS), and the neutron exchanges a small amount of energy with atoms in the sample. QENS is a scattering phenomenon, which is centered at zero-energy transfer but which broadens the spectral width due to diffusive motions. The measured scattering intensity is a function of both momentum and energy transfer; atomic motions can be interpreted through this intensity.

A proton has a large incoherent scattering cross section with a thermal neutron; this type of neutron scattering is a powerful probe revealing rich information about a protonic material's dynamics. One of the neutron scattering experiment's most important applications is studying the material's dynamics mechanisms, such as diffusion, especially through QENS experiments. Matzke et al. (1996) used QENS to study proton diffusion in Yb-doped $SrCeO_3$. The study proposed a two-state model: free diffusion (where the proton jumps from one oxygen site to a new oxygen site.) and trap states (the protons are confined to low energetic sites nearby the dopant sites for a definite time). The proton migrates with successive jumps, trapping near an Yb^{3+} ion and then escaping from the trapping state due to thermal fluctuations.

This brief historical review reveals that the QENS is a powerful tool for understanding proton conductors' dynamics, and we have made extensive use of it in this work.

2.3 Scattering length and scattering cross-sections

Finding the nuclear interaction potential is not a trivial calculation. Cold/Thermal neutron scattering, with energy less than 0.1 eV, doesn't affect the internal energy of the nucleus much and can be treated as perturbation. The nuclear forces are of short range, 10^{-3} to 10^{-2} Å, in comparison to the neutron wavelength (ex. cold neutron) of 6.16 Å. The nucleus looks like a point scatterer; thus, scattering of the cold/thermal neutron and the nucleus is considered to be isotropic scattering (s-wave scattering) with equal probability in any direction and is characterized by a single parameter: b, scattering length. This parameter depends on the details of the nuclear structure and independent of the incident neutron energy and the momentum transfer Q; in other words, it is not a function of the scattering angle because the neutron wavelength is much larger than the size of the nucleus (10^{-15} m).

Reflecting the strength of the interaction between the neutron and the nucleus, the scattering length can be positive or negative, depending on the nucleus and the neutron interaction potential, expressed by the neutron's eigenfunction phase shifts upon scattering from the nucleus. A negative phase shift occurs from repulsive potentials. A negative value of b means that the phase is shifted by 180°.

There are two types of scattering length: the coherent scattering b_i^{coh} and the incoherent scattering length b_i^{inc}. The samples are composed of many atoms, where the nuclear species (i) have many isotopes with scattering lengths $b_1, b_2, b_3, ...$ with respective abundances $n_1, n_2, n_3, ...$ The average scattering length of several atomic species (i) by $\langle b_i \rangle$ over all the isotopes and spin states is called the coherent scattering

length:

$$b_i^{\text{coh}} = \langle b_i \rangle = \sum_i n_i b_i \tag{2.11}$$

The coherent neutron scattering cross-section is

$$\sigma_{\text{coh}} = 4\pi \langle b_i \rangle^2 \tag{2.12}$$

where b depends on the details of the nuclear structure and varies greatly among elements/isotopes, which the incoherent scattering length can represent. The incoherent scattering length is defined the root mean square deviation of b_i from the average

$$b_i^{\text{inc}} = \sqrt{\langle b_i^2 \rangle - \langle b_i \rangle^2} \tag{2.13}$$

and the incoherent neutron scattering cross-section given by

$$\sigma_{\text{inc}} = 4\pi \left(\left\langle b_i^2 \right\rangle - \langle b_i \rangle^2 \right) \tag{2.14}$$

describes the square fluctuation of the scattering length due to the difference in isotope species. The total scattering cross-section is then equal to

$$\sigma_T = \sigma_{\text{coh}} + \sigma_{\text{inc}} \tag{2.15}$$

The hydrogen has an interesting scattering length, where the incoherent scattering cross-section is extremely larger than the coherent part. Both the proton and the neutron have spin 1/2, where the total spin of the neutron and proton system is $S = 1$ ((p, n) triplet state of scattering) and $S = 0$ ((p, n) singlet state of scattering) with statistical weights, $2S + 1$, equal to 3 and 1, respectively. The triplet state is bound with the positive scattering length, while the singlet state is unbound with the negative scattering length. The singlet's scattering length is four times that of the triplet, resulting in the coherent scattering length being negative and the incoherent scattering length being large. The difference between the cross section of the hydrogen

Table 2.2: Scattering lengths of hydrogen species and oxygen (all measured in barns).

${}^{Z}\text{Symbol}_{A}$	σ_{coh}	σ_{inc}	σ_{scatt}	σ_{abs}
${}^{1}\text{H}$	1.757	80.260	82.020	0.333
${}^{1}\text{H}_{1}$	1.758	80.270	82.030	0.333
${}^{1}\text{H}_{2}$	5.592	2.050	7.640	0.001
${}^{1}\text{H}_{3}$	2.890	0.140	3.030	$< 3.0 \times 10^{-6}$
${}^{8}\text{O}$	4.232	0.000	4.232	0.000

and that of deuterium plays an important role in isotope labeling. Table 2.2 presents the scattering lengths of hydrogen species and oxygen.

The neutron-nucleus scattering process is a quantum mechanical transition, where the neutron scattered intensity I in QENS signal is proportional to double-differential cross section. This intensity is given by

$$I = I_0 n_0 V \left(\frac{\mathrm{d}^2\sigma(E_1, E_2, \theta)}{\mathrm{d}\Omega\, \mathrm{d}\omega} \right) \Delta\Omega\Delta\omega \tag{2.16}$$

where I_0 is the intensity of neutrons from a monochromatic beam, $\Delta\Omega$ is the scattered solid angle, V is the sample's volume and n_0 is atomic number density of the sample. The differential cross-section, calculated as $\mathrm{d}^2\sigma(E_1, E_2, \theta)/\,\mathrm{d}\Omega\,\mathrm{d}\omega$, and gives the probability that a neutron with incident energy E_1 leaves the sample in the solid angle element $d\Omega$ about the direction Ω at angle θ with an energy exchange given by $\hbar\omega = E_2 - E_1$ and $\hbar(\omega + d\omega)$. During the scattering process, the sample's energy change is related to the neutron's energy change. The Hamiltonian of the neutron beam and the sample is

$$H = H_0 + \frac{p_n^2}{2m} + V \tag{2.17}$$

in which, H_0 is the unperturbed Hamiltonian, $p_n^2/2m$ is the neutron's kinetic energy, and V is the interaction potential between the neutron and the sample's nuclei.

2.4 The effective Fermi pseudopotential

The range of the interaction between the thermal/cold neutron with nuclei is very small compared to the thermal/cold neutron's wavelength in the experiment. In this case, the nucleus looks like a point scatterer. By assuming that the scattering between the neutron and nuclei is s-wave scattering (spherically symmetric scattering), and with the neutron at $\vec{r}$ and a nucleus at $\vec{R}_j(t)$, then the position of the nucleus will be time-dependent. With the scattering length b_j, the effective Fermi pseudopotential can be used. For all nuclei j in the sample, the Fermi pseudopotential is given as a sum of δ-functions for all individual neutron-nuclei interactions. The potential is given as a function of radius, $\vec{r}$ and one parameter, the scattering length, b_j, of each nuclei.

$$V(\vec{r}) = \sum_j V(\vec{r} - \vec{R}_j) = \left(\frac{2\pi\hbar^2}{m_n}\right) \sum_j b_j \delta(\vec{r} - \vec{R}_j) \tag{2.18}$$

where m_n is the neutron mass. The scattering process is a quantum mechanical transition. A first-order perturbation approximates the system's total wavefunction to determine the transition probabilities from the initial state to the final state, and the double differential cross-section formula can finally be obtained:

$$\begin{aligned} \frac{\mathrm{d}^2\sigma}{\mathrm{d}\Omega\,\mathrm{d}\omega} = \left(\frac{k_2}{k_1}\right) \frac{1}{2\pi\hbar} \Bigg[\langle b \rangle^2 \sum_i \sum_j \int_{-\infty}^{\infty} e^{-i\omega t} dt \left\langle e^{-i\vec{Q}\cdot\vec{R}_i(0)} e^{i\vec{Q}\cdot\vec{R}_j(t)} \right\rangle \\ + \left(\langle b^2 \rangle - \langle b \rangle^2 \right) \int_{-\infty}^{\infty} e^{-i\omega t}\,\mathrm{d}t \sum_i \left\langle e^{-i\vec{Q}\cdot\vec{R}_i(0)} e^{i\vec{Q}\cdot\vec{R}_i(t)} \right\rangle \Bigg] \end{aligned} \tag{2.19}$$

The first term is the coherent scattering, which provides information on spatial correlation and collective motion. The second term describes the incoherent scattering, which provides information about single particles. The factor k_2/k_1 arises from the detector velocity-dependence. Equation 2.19 can be rewritten as

$$\frac{\mathrm{d}^2\sigma}{\mathrm{d}\Omega\,\mathrm{d}\omega} = \left(\frac{\mathrm{d}^2\sigma}{\mathrm{d}\Omega\,\mathrm{d}\omega}\right)_{\mathrm{coh}} + \left(\frac{\mathrm{d}^2\sigma}{\mathrm{d}\Omega\,\mathrm{d}\omega}\right)_{\mathrm{inc}} \tag{2.20}$$

2.5 The intermediate scattering function

Based on 2.19, the coherent and incoherent (self-term) of the intermediate scattering functions can be defined:

$$I(\vec{Q},t) = N^{-1}\sum_{i=1}^{N}\sum_{j=1}^{N}\left\langle e^{-i\vec{Q}\cdot\vec{R}_i(0)}e^{i\vec{Q}\cdot\vec{R}_j(t)}\right\rangle \tag{2.21}$$

The self-intermediate scattering function

$$I_S(\vec{Q},t) = N^{-1}\sum_{i=1}^{N}\left\langle e^{-i\vec{Q}\cdot\vec{R}_i(0)}e^{i\vec{Q}\cdot\vec{R}_i(t)}\right\rangle \tag{2.22}$$

The double differential cross section reads:

$$\begin{aligned}\frac{\mathrm{d}^2\sigma}{\mathrm{d}\Omega\,\mathrm{d}\omega} = \left(\frac{k_2}{k_1}\right)\frac{N}{2\pi\hbar}\Bigg[\left\langle b^2\right\rangle\int_{-\infty}^{\infty} I(\vec{Q},t)e^{-i\omega t}dt \\ + \left(\left\langle b^2\right\rangle - \left\langle b\right\rangle^2\right)\int_{-\infty}^{\infty} I_S(\vec{Q},t)e^{-i\omega t}dt\Bigg]\end{aligned} \tag{2.23}$$

where N is the number of nuclei in the sample. The intermediate function is dimensionless. Spin echo experiment measures the intermediate scattering function.

2.6 The van Hove correlation

As mentioned above, the scattering process is a quantum mechanical transition. A first-order perturbation approximates the system's total wavefunctions to determine the transition probabilities from the initial state to the final state. It should be noted that particle diffusion in condensed matter will be treated in terms of statistical physics. The interface between the scattering process and the classical particle diffusion will be determined by thermal averages and expressed in van Hove correlation functions as described next. In equation 2.19, the nucleus i is located at $\vec{R}_i$ at time zero, while the nucleus j is located at $\vec{R}_j$ at time t. It should be noted that $\vec{R}_i$ and $\vec{R}_j$

are quantum mechanical operators. The first term of equation 2.19 is a double sum over all the nuclei positions in the sample as shown in equation 2.24. The angular brackets $\left\langle e^{-i\vec{Q}\cdot\vec{R}_i(0)}e^{i\vec{Q}\cdot\vec{R}_j(t)}\right\rangle$ gave van Hove the idea of doing a thermodynamic average over all the sample's possible configurations. The coherent double differential cross-section configuration is as indicated below:

$$\frac{\mathrm{d}^2\sigma}{\mathrm{d}\Omega\,\mathrm{d}\omega} = \left(\frac{k_2}{k_1}\right)\frac{1}{2\pi\hbar}\left[\left\langle b^2\right\rangle\sum_i\sum_j\int_{-\infty}^{\infty}e^{-i\omega t}dt\left\langle e^{-i\vec{Q}\cdot\vec{R}_i(0)}e^{i\vec{Q}\cdot\vec{R}_j(t)}\right\rangle\right] \tag{2.24}$$

The van Hove correlation, or the time-dependent pair correlation function $G(\vec{r},t)$, is the inverse Fourier transform of the intermediate scattering functions in space:

$$G(\vec{r},t) = \frac{1}{2\pi^3}\int I(\vec{Q},t)e^{i\vec{Q}\cdot\vec{r}}\,\mathrm{d}\vec{Q} \tag{2.25}$$

$$G(\vec{r},t) = \frac{1}{N}\sum_{i,j}\delta(\vec{r}-[\vec{R}_i(0)-\vec{R}_j(t)]) \tag{2.26}$$

The time-dependent pair correlation function describes how the correlation between nuclei positions changes as a function of time. The dimension of the van Hove correlation function is 1/volume. Equation 2.26 is zero unless the distance between $\vec{R}_i(0)-\vec{R}_j(t)$ equals $\vec{r}$, meaning the van Hove Correlation function gives the probability nucleus at the origin at time zero in the same time a probability of a nucleus at position $\vec{r}$ at time t. The double differential cross section can be written in terms of the van Hove Correlation function as the following:

$$\frac{\mathrm{d}^2\sigma}{\mathrm{d}\Omega\,\mathrm{d}\omega} = \left(\frac{k_2}{k_1}\right)\frac{Nb^2}{2\pi\hbar}\int_{-\infty}^{\infty}G(\vec{r},t)e^{-i(\vec{Q}\cdot\vec{r}-\omega t)}\,\mathrm{d}\vec{r}\,\mathrm{d}t \tag{2.27}$$

Equation 2.27 gives the probability of finding two nuclei at separation distance $\vec{r}$.

2.7 The dynamic structure factor

The dynamic structure factor $S(\vec{Q},\omega)$ is a Fourier transform in space and time of the van Hove Correlation function. The dimension of the $S(\vec{Q},\omega)$ is time.

$$S(\vec{Q},\omega) = \frac{1}{2\pi}\int_{-\infty}^{\infty}\int G(\vec{r},t)e^{-i(\vec{Q}\cdot\vec{r}-\omega t)}\,\mathrm{d}\vec{r}\,\mathrm{d}t \tag{2.28}$$

The double differential cross section is proportional to the scattering function or dynamic structure factor $S(\vec{Q},\omega)$, which can be calculated for typical diffusive processes:

$$\frac{\mathrm{d}^2\sigma}{\mathrm{d}\Omega d\omega} = \frac{k_2}{k_1}\left(\frac{\sigma_{\mathrm{coh}}}{4\pi}S_{\mathrm{coh}}(Q,\omega) + \frac{\sigma_{\mathrm{inc}}}{4\pi}S_{\mathrm{inc}}(Q,\omega)\right) \tag{2.29}$$

Equation 2.29 shows that the coherent and incoherent dynamic structure factors depend on Q and the energy transfer $\hbar\omega$, which, in turn, depends on the sample's nature. The self-correlation function's Fourier transform gives the incoherent scattering function, which does not exhibit any interference phenomena. The van Hove self-correlation function is the probability of finding an atom at $\vec{r}$ at time t when the same atom is located initially at the origin. The van Hove self-correlation describes translation diffusion or rotational diffusion or combination of both.

The following provide information about the sample: the time-dependent pair correlation function, $G(\vec{r},t)$; the intermediate scattering function, $I(\vec{Q},t)$; and the dynamic structure factor, $S(\vec{Q},\omega)$, gives information about the sample. Only $I(\vec{Q},t)$ and $S(\vec{Q},\omega)$ can be measured experimentally.

Chapter 3

Models of Diffusion

Quasi-elastic neutron scattering facilitates studying self-diffusion in condensed matter. In many studies, the diffusion coefficients can be obtained without a model when the particle motion obeys Fick's law of diffusion. By using jump diffusion models, microscopic dynamic information can be obtained, such as the elementary jump's relaxation time, self-diffusion, and jump length. In this study, the QENS result for Ca-doped $LaPO_4$ has been modeled using the isotropic Chudley-Elliott model, whereby the proton's self-diffusion, jump length, and time residence have been determined. This chapter briefly describes the Chudley-Elliott model as well as other jump models. More detailed descriptions can be found such studies as Chudley and Elliott (1961); Chathoth et al. (2011); Singwi and Sjölander (1960); Hall and Ross (1981); Roe (2000); Embs et al. (2010); Fitter et al. (2006).

3.1 Types of motion

Neutron scattering spectra consist of three energy-transfer ($\Delta E = \hbar\omega$) regions: elastic ($\hbar\omega = 0$), inelastic region ($\hbar\omega \neq 0$), and quasielastic ($\hbar\omega$ near to zero). Typical types of motion found in complex systems include vibrational motion, orientation of the particle about its center of mass, and the particle's translational diffusion. These motions' time scales are distinguishable from each other. The elastic component's

width reflects the instrument resolution and gives information about the translational motion and the proton's slow diffusional motion inside the sample at fixed Q. The inelastic region gives information about the vibration (V), translation diffusion (T), and rotation (R). High-resolution QENS measurements at small amounts of energy transfer around zero give information about the rotational and translational diffusion. The proton position changes $\vec{r}$ by translational, rotational, and thermal vibrational motions. These motions are usually assumed uncorrelated. This working hypothesis can be justified in some systems; however, in this study, a correlation exists among these motions. The dynamic structure factor can be written as a product of the three motions:

$$S(\vec{Q},\omega) = S^{\mathrm{T}}(\vec{Q},\omega) \times S^{\mathrm{R}}(\vec{Q},\omega) \times S^{\mathrm{V}}(Q,\omega) \tag{3.1}$$

where $S^{\mathrm{T}}(\vec{Q},\omega)$, $S^{\mathrm{R}}(\vec{Q},\omega)$ and $S^{\mathrm{V}}(\vec{Q},\omega)$ are the dynamical structure factors due to translational, rotational, and vibration motions, respectively. $S^{\mathrm{V}}(\vec{Q},\omega)$ is related to the vibrational Debye-Waller factor, which is effective only as the quasi-elastic intensity's multiplicative factor. The scattering intensity's Q-dependent attenuation is presented later in this work. Equation 3.2 includes the influence of the proton's vibrational motion for all Q-values at a fixed temperature:

$$S_{\mathrm{exp}}(\vec{Q},\omega) = e^{-Q^2\langle u^2\rangle/3} S_{\mathrm{ideal}}(Q,\omega) \tag{3.2}$$

where $\exp(-Q^2\langle u^2\rangle/3)$ is the Debye-Waller factor, and $\langle u^2\rangle$ is the atomic mean square displacement.

3.2 Self-diffusion

Long-range self-diffusion (small Q values) can be obtained from the self-correlation function that follows Fick's second law of diffusion:

$$\frac{\partial}{\partial t} G_S(\vec{r},t) = D_S \nabla^2 G_S(\vec{r},t) \tag{3.3}$$

A proton starts at a fixed point and zero time:

$$G_S(\vec{r}, 0) = \delta(\vec{r}) \tag{3.4}$$

Equations 3.3 and 3.4 give the probability that if a proton is at the origin at time zero, it will be at position $\vec{r}$ at time t with diffusion coefficient D_S.The solution of 3.3 with the initial condition 3.4 is

$$G_S(\vec{r}, t) = \frac{1}{(4\pi D_S|t|)^{3/2}} \exp\left(-\frac{r^2}{4D_S|t|}\right) \tag{3.5}$$

The Fourier transformation of the van Hove in space gives the intermediate scattering function's self-part:

$$I_S(\vec{Q}, t) = \exp(-Q^2 D_S t) \tag{3.6}$$

and the relaxation time is

$$\tau = \frac{1}{D_S Q^2} \tag{3.7}$$

In the case of long-range translation diffusion, the $I_S(\vec{Q}, t)$ goes to zero after a very long time ($t \to \infty$); while if the motion is localized (such as rotation or diffusion inside a confinement; for example, water diffusion inside carbon nanotubes; Chathoth et al. (2011)), the intermediate scattering function approaches a finite value at $t \to \infty$. The Fourier transformation of the van Hove in space and time gives the incoherent scattering function:

$$S_S^T(\vec{Q}, \omega) = \frac{1}{\pi} \frac{D_S Q^2}{(D_S Q^2)^2 + \omega^2} \tag{3.8}$$

Based on equation 3.8, the dynamic structure factor is a pure Lorentzian in long-range diffusion with half width at half maximum (HWHM) equal to $D_S Q^2$. The HWHM increase with increase Q^2 is direct.

3.3 Jump diffusion

Jump diffusion is a stochastic process in which a particle or a proton has many sequential jumps in the matter which finally lead to particle diffusion. Three jump-diffusion models give dynamic microscopic information, such as the mean jump length in crystals, residence time, and diffusion coefficient:

- Chudley and Elliott model (CE)
- Singwi and Sjölander model (SS)
- Hall and Ross model (HR).

3.3.1 Chudley and Elliott model (CE)

Chudley and Elliott (1961) calculated the slow neutrons incoherent inelastic scattering cross-section for liquid. The liquid is assumed to have considerable short range order in a quasi-crystalline configuration. Where a regular spatial arrangement of atom sites on a liquid's lattice. The CE model also becomes a model for atomic diffusion within crystalline interstitial lattices. This model assumes that diffusive motion occurs via large discrete jumps, whereby the particle resides for a time interval τ at a given site and then jumps in a relatively short (essentially instantaneous) time to a new location a distance ℓ away. $P(\vec{r},t)$ is the probability to find a diffusing atom or particle on a position $\vec{r}$ on the lattice at time t where it resides an average time τ. If the jump occurs between one site to the neighbor $\vec{r}+\mathrm{d}\vec{r}_i$ where $\vec{r}_i$ $(i=1,2,...,n)$ is a set of jump vectors, the jump can be from the first site to another according to this distribution:

$$\frac{\partial P(\vec{r},t)}{\partial t} = -\frac{1}{\tau}P(\vec{r},t) + \frac{1}{n\tau}\sum_{i=1}^{n} P(\vec{r}+\mathrm{d}\vec{r},t) \tag{3.9}$$

On the right side of equation 3.9, the first and second terms are the loss and gain rates because of the jumps to and from adjacent sites, respectively. The $G_S(\vec{r},t)$ is

the solution of equation 3.9 with the boundary condition

$$P(\vec{r}, 0) = \delta(0) \tag{3.10}$$

and the Fourier transform is

$$G_S(\vec{r}, t) = \int_{-\infty}^{\infty} I_S(\vec{Q}, t) e^{-i\vec{Q}\cdot\vec{r}} \, \mathrm{d}\vec{Q} \tag{3.11}$$

If $I_S(\vec{Q}, t) = e^{-\Gamma(\vec{Q})|t|}$, then the Fourier transform of $I_S(\vec{Q}, t)$ is a Lorentzian

$$S_S(\vec{Q}, \omega) = \frac{1}{\pi} \frac{\Gamma(\vec{Q})}{\omega^2 + \Gamma(\vec{Q})^2} \tag{3.12}$$

In this model, $S(\vec{Q}, \omega)$ is a Lorentzian whose width varies in Q and the half width half maximum (HWHM) is $\Gamma(\vec{Q})$. For small $\vec{Q}$ ($Q \ll 1/d$, d is the length of jump vector), information can be obtained about long-range diffusion, where the HWHM is

$$\Gamma(\vec{Q}) = \frac{\ell}{6\tau} Q^2 = D_S Q^2 \tag{3.13}$$

In polycrystalline samples, an orientational averaging of the theoretical scattering function $S_S(\vec{Q}, \omega)$ or the width function can be averaged and the isotropic approximation obtained by

$$\Gamma(\vec{Q}) = \frac{1}{\tau} \left(1 - \frac{\sin(Q\ell)}{(Q\ell)} \right) \tag{3.14}$$

and the diffusion coefficient, $D = \ell^2/6\tau$. From equation 3.14, the average jump length ℓ can be determined from the Q-dependence of the measured quasi-elastic HWHM Fitter et al. (2006).

The CE model with a single jump distance can describe the Q-dependence of the Lorentzian half-widths. The coupling between the stochastic motion and the vibrational motion is often neglected in the theoretical description. This

approximation can work for very small momentum transfers; but for large transfers, overlapping between the vibration and diffusive motion occurs.

3.3.2 Singwi and Sjölander model (SS)

Singwi and Sjölander (1960) created a model that expresses the jump as an alternation between oscillatory motion and directed motion. It shows the Mössbauer-type experiment can potentially be used to obtain information about the diffusive motion of atoms in solids and liquids. Using a model of liquid water in which a molecule oscillates for a mean time τ_0 and then diffuses as a free particle through continuous motion for a mean time τ, the motion exchange between oscillation and translation is continually repeated with $\tau \ll \tau_0$. The SS model calculates cold neutrons differential scattering cross section. Cold neutron scattering in water can determine not only the diffusion coefficient but also the diffusion mechanism. A calculation for the van Hove correlation function and its Fourier transform is presented in this model. The shape of the quasi-elastic peak, is found to be Lorentzian with the HWHM:

$$\Gamma(\vec{Q}) = \frac{2}{\tau_0}\left(1 - \frac{e^{-2W}}{1 + D\tau_0 Q^2}\right) \tag{3.15}$$

$$2W = \frac{1}{6}Q^2R^2 \tag{3.16}$$

$2W$ is the Debye-Waller factor in a solid, R^2 is the mean square radius from its equilibrium positions. If $D\tau_0 Q^2 \ll 1$, the HWHM reads

$$\Gamma(\vec{Q}) = 2Q^2 D_S \tag{3.17}$$

The result is the same for long-range diffusion, which simple diffusion theory can obtain. If $D\tau_0 Q^2 \gg 1$, the HWHM value or quasi-elastic line width broadening

approaches the asymptotic value

$$\Gamma(\vec{Q}) = \frac{2}{\tau_0} \tag{3.18}$$

3.3.3 Hall and Ross model (HR)

The Hall and Ross (1981) (HR) calculates the incoherent neutron scattering function, $S_{\text{inc}}(\vec{Q}, \omega)$, and the van Hove self-correlation function $G_S(\vec{r}, t)$ of geometrically restricted diffusion. Naturally, the host materials form geometrical boundaries that limit a particle to diffuse inside its network. An example is the confined system in which structural cages, particles, or molecules are located in pores. $S_{\text{inc}}(\vec{Q}, \omega)$ is calculated from the random walk theory, assuming a Gaussian distribution of jump lengths for unbounded jump diffusion. Where the Gaussian distribution of jump length reads

$$\rho(r) = \frac{2r^2}{r_0^3\sqrt{2\pi}} \exp\left(-\frac{r^2}{2r_0^2}\right) \tag{3.19}$$

the mean square displacement is

$$\left\langle r^2 \right\rangle = \int_0^\infty r^2 \rho(\vec{r})\, \mathrm{d}\vec{r} \tag{3.20}$$

$$\left\langle r^2 \right\rangle = 3r_0^2 \tag{3.21}$$

HWHM is

$$\Gamma(\vec{Q}) = \frac{\hbar}{\tau}\left(1 - e^{-Q^2 r_0^2/6}\right) \tag{3.22}$$

The HR can be applied to calculate the neutron scattering function for bound diffusion jump in one and three dimensions.

Chapter 4

Experimental

High phase purity polycrystalline monazite (monoclinic $LaPO_4$) and aliovalent (Sr, Ca) doping on lanthanum orthophosphate ($LaPO_4$) were synthesized via solid state reaction (SSR) and co-precipitation (CPT). The samples were characterized by X-ray powder diffraction (XRD), thermogravimetric analysis (TGA), scanning electron microscope (SEM), electrochemical impedance spectroscopy (EIS), and neutron powder diffraction (NPD) from room temperature to 800°C. Macroscopic and microscopic dynamics were studied using EIS and quasi-elastic neutron scattering (QENS). This chapter briefly introduces the experimental parts.

4.1 Sample synthesis

Monazite in general and lanthanum orthophosphate ($LaPO_4$) specifically are essential materials in disposing of actinides technology. The orthophosphate materials are used as host waste containers to store high-level radioactive waste (Boatner (2002)). Recently, orthophosphate materials have attracted much attention due to their possible application as high-temperature proton conductors for dominant protonic conduction and high chemical stability, *e.g.* Amezawa et al. (2005).

Monazite (monoclinic $LaPO_4$) and aliovalent (Sr, Ca) doping on lanthanum orthophosphate ($LaPO_4$) were synthesized using two methods: solid state reaction

(SSR) and co-precipitation (CPT). According to Amezawa et al. (2005), Sr-doped $LaPO_4$ has higher conductivity than Ca-doped $LaPO_4$; but both conductivities are in the same order of magnitude. These researchers concluded that the differences in the conduction features can be determined from the solubility difference between the Sr and Ca in the lanthanum orthophosphate. They also found the solubility limit of Ca and Sr in the $LaPO_4$ lattice to be 4.2 and 1.9 mol%, respectively, where they used the solid state reaction method. Whereas Gallini et al. (2005) have found that using the co-precipitation (CPT) method increased the solubility limit of Sr up to 10 mol%. Similiarly, Hatada et al. (2011), also using the precipitation method, reported an increase in the solubility limit of Sr up to 20 mol%.

4.1.1 Solid state reaction

The solid state reaction is also called the ceramic method or "heat & beat" or "shake & bake," and involves the stoichiometric reaction of powders, which are mixed and calcined at high temperature in air or under vacuum or in inert (Noble gases, N,) or in reactive gases such as (CO,O_2,..). Calcination is a thermal treatment on the sample below the melting point of the material under gas (such as air, oxygen, or He..). Applying calcination, the material can go through thermal decomposition or phase transition or dehydration.The solid state reactions happen only at the two components' interface, and the reactants diffuse from the bulk to the interface. Consequently, it is very important to mix and grind the powder adequately and to elevate the temperature to increase the reactants' diffusion toward the interface. Mixing, grinding, and heating increase the chances of getting more homogeneous crystalline material and increased crystallinity. Pelletizing the powder under suitable pressure is also important to reduce the sample's porosity and to have more compact dense material after sintering the powder at 2/3 of the melting temperature. Briefly, sintering is a thermal treatment that leads to particles agglomeration and to pores reduction. It enhances properties of material such as strength.

For the present work, using conventional solid-state reaction, $La_{0.958}Ca_{0.042}PO_{3.979}$, $La_{0.99}Ca_{0.01}PO_{3.995}$ and $La_{0.99}Sr_{0.01}PO_{3.995}$ powders were synthesized. For the $La_{0.958}Ca_{0.042}PO_{3.979}$, the starting materials were calcium phosphate dibasic dihydrate (Fisher Scientific) and lanthanum (III) phosphate hydrate (Strem Chemicals Inc.). The $LaPO_4 \bullet nH_2O$ powder was first dried at 1000°C for 48 h. Mixed stoichiometric amounts of $CaHPO_4 \bullet_2 H_2O$ and $LaPO_4$ powder were calcined at 1000°C for 5 h. The material was finely crushed using an agate mortar, followed by dry ball milling for 45 min.; this process was repeated 4 times to ensure homogeneous mixing. After pelletizing a 12 mm diameter pellet under a load of 7 metric tons, the samples were sintered at 1200°C in air for 5 h. Pellets with a relative density of 94% of the X-ray density were obtained.

With $La_{0.99}Sr_{0.01}PO_{3.995}$, the starting materials were $LaPO_4$ and $SrHPO_4$, using the same procedures as described above.

4.1.2 Co-precipitation (CPT)

$La_{0.958}Sr_{0.042}PO_{3.979}$, $La_{0.92}Sr_{0.08}PO_{3.96}$, and $La_{0.9}Sr_{0.1}PO_{3.95}$ samples were prepared by using the following precursors: Lanthanum (III) nitrate hexahydrate (99.9%-La (REO), Strem Chemicals) $La(NO_3)_3 \bullet_6 H_2O$, Strontium nitrate (99+%, ACS, Acros Organics) $Sr(NO_3)_2$ and Ammonium phosphate (99+%, Acros Organics) $(NH_4)_2HPO_4$. Precursor solutions (0.2 M) were prepared. The $(NH_4)_2HPO_4$ solution was mixed drop by drop with speed 5 ml/min, at room temperature with the solution of the lanthanum and strontium nitrates (constantly stirred). After filtering the gel, the product was dried at 105°C for two days. The dried material was crushed using an agate mortar. The powders were calcined at temperatures 800°C in air, for 12 h at a heating rate of 2°C/min in Pt crucible. The material was finely crushed using an agate mortar, followed by dry ball milling a 15 minutes and repeated several times. After pelletizing under a load of 7 metric tons, the samples were sintered at 1200°C in air for 4 h. Dense pellets were obtained. For the $La_{0.958}Sr_{0.042}PO_{3.979}$

a relative density of 97% of the X-ray density obtained. Another batch from the, $La_{0.958}Sr_{0.042}PO_{3.979}$, $La_{0.92}Sr_{0.08}PO_{3.96}$, and $La_{0.9}Sr_{0.1}PO_{3.95}$ samples were sintered at 1400°C for comparison between two different sintering temperature.

4.2 X-ray powder diffraction (XRD)

Powder X-ray diffraction (XRD) was used to study the samples for phase identification and structure refinement. The samples' initial structural characterization was conducted using a Bruker AXS D2 Phaser diffractometer with Cu Kα radiation (λ = 1.541 Å) and a range of 10°-90° with a scan rate of 0.02°s^{-1}. Data for Rietveld refinement were collected for the samples using a Panalytical X-pert Pro diffractometer with Cu Kα1 radiation in the range of 5°-130° with a scan rate of 0.0167°s^{-1} at center for nanophase materials sciences (CNMS) ORNL.

4.3 Scanning Electron Microscopy

Scanning Electron Microscopy (SEM) was performed, at CNMS, on the samples with Zeiss ULTRA-55 FEG SEM in SE2 detection mode at voltage 10 kV and 5 kV for higher resolution. Sintered pellets similar to those used in EIS measurements prior to electrode fabrication were examined.

4.4 Thermogravimetric Analysis (TGA)

Thermogravimetric analysis (TGA) was performed using Netzsch STA 409 PC Luxx, with 76 mg of hydrated sample contained in an alumina crucible. The samples were subject to the following procedure: (1) dehydration by treating the powder in a high-purity dry Ar (99.99%) inside the TGA instrument from room temperature to 1266°C, with a heating rate of 5°C/min and a flow rate of 50 ml/min, followed by an isothermal dwell at 1266°C for 4 h under dry Ar atmosphere; (2) hydration using an

isothermal dwell at 1266°C for 1 h under humid Ar atmosphere, followed by slowly cooling the powder in a humid Ar atmosphere to room temperature at a rate of 2 K/min.

4.5 Electrochemical Impedance Spectroscopy (EIS)

For the electrochemical impedance spectroscopy (EIS) measurements, the sintered pellets were polished to a thickness of 1 mm using SiC paper. The pellets were washed with acetone and then dried at 200°C using a hot plate. The resulting surface was smooth and even. Electrodes were prepared by applying 7 mm diameter circle of Pt paint to each side of the 12 mm diameter pellet and firing at 900°C for 0.5 h in air. The cell was connected by pressing a Pt mesh with Pt wire lead on the surfaces of the two symmetrical porous Pt electrodes. The cell was heated in dry air up to 1000°C for 12 h inside a quartz reactor which was supported in a tube furnace. The dry air was obtained by passing the air gas through the silica-gel dryer with a flow rate of 50 ml/min. Impedance spectra were recorded for one hour at each temperature from 1000°C to 500°C in dry air with cooling rate 5°C/min. The dry air was then switched to hydrated air, with 2.2 mol% water, with a flow rate of 50 ml/min. The cell was heated to 1000°C with heating rate of 5°C/min and held for another 15 h to hydrate the samples. Impedance spectra were recorded in humid air from 1000°C to 500°C with cooling rate of 5°C/min in the frequency range 10^{-2}-10^{6} Hz with signal amplitude of 100 mV using VersaSTAT 4 (Princeton Applied Research) with an internal frequency response analyzer (Bi et al. (2011)).

4.6 Neutron Powder Diffraction (NPD)

To investigate the crystal structures, accurate information about the following is needed: atomic displacement parameters (ADPs), structural parameters, and interatomic distances and angles for the samples. Also needed is an examination of the

chemical and thermal stability of the doped and undoped lanthanum orthophosphate ($LaPO_4$) samples.

Time-of-flight (TOF) powder neutron diffraction data were collected using the POWGEN (BL-11A) diffractometer at the Spallation Neutron Source facility, Oak Ridge National Laboratory in Oak Ridge, Tennessee. The samples were run in two beam times. In the first beam time, two samples of $La_{0.958}Ca_{0.042}PO_4 \bullet nD_2O$ and $La_{0.958}Sr_{0.042}PO_4 \bullet nH_2O$ with masses of 10.15 g and 10.36 g, respectively, were run. The experiment was conducted using an ILL-furnace with vanadium heating elements and with a quartz insert that allows air flow through the sample. A Portable Automated Gas Environment (PAGES) was connected to the quarts insert that allows many different gas mixtures to flow through the sample. The samples were loaded in different quartz basket with frit at the bottom and with an open top to permit gas to flow through the sample. The ILL furnace, with a quartz insert, can heat up to 850°C. This sample cell used is explained in detail in Chapter 7 and in a paper, al-Wahish et al. (2014a), submitted recently for publication.

The data were collected using center wavelengths (CWLs) of 1.333 Å that cover d-spacing from 0.41 to 3.8 Å. Data were collected at 18°C, 26°C, 35°C, 500°C, 800°C and at 60°C, 70°C, 180°C, 260°C, 360°C, 500°C, and 310°C for $La_{0.958}Ca_{0.042}PO_4 \bullet nD_2O$ and $La_{0.958}Sr_{0.042}PO_4 \bullet nH_2O$, respectively.

In the second beam time, the following six samples were loaded in separate 6 mm diameter vanadium cans sealed under He: $LaPO_4$, $La_{0.958}Ca_{0.042}PO_4 \bullet nD_2O$, $La_{0.958}Ca_{0.042}PO_4$, $La_{0.99}Ca_{0.01}PO_4 \bullet nD_2O$, $La_{0.958}Sr_{0.042}PO_4 \bullet n\ D_2O$ and $La_{0.958}Sr_{0.042}PO_4$ with masses of 7.7 g, 7.8 g, 7.4 g, 7.5 g, 9.5 g and 8.8 g, respectively. The data were collected at 300 K for all the samples using the same center wavelengths (CWLs) of 1.333 Å covering the same d-spacing (from 0.41 to 3.8 Å) as above. Rietveld refinement of the data was performed using FullProf suite (Carvajal (1993)). The NPD and XRD explored the structure and defect structure of aliovalent (Sr, Ca) doping on $LaPO_4$ materials.

4.7 Quasi-elastic Neutron Scattering (QENS)

The quasi-elastic neutron scattering data collected using the BASIS (BL-2) backscattering spectrometer at the Spallation Neutron Source (SNS), Oak Ridge National Laboratory (ORNL), Oak Ridge, Tennessee (Mamontov and Herwig (2011)). The energy resolution at the elastic line (full width at half-maximum) was 3.4 μeV. Prior to the QENS experiment, the samples were charged with protons by post-annealing in oxygen atmosphere with a water vapor pressure of 2.2 kPa from a bubbler at 19°C; the samples were then held in a dry oxygen atmosphere at 200°C for several hours to remove any surface water. The samples were kept in sealed container in a vacuum desiccator to avoid any contact with ambient air until the time to conduct the experiment. The samples were mounted in a platinum cylindrical sample holder of annular geometry shortly prior to the QENS experiment. In order to minimize multiple scattering the mass and thickness of the sample were limited to $\sim$ 10 g and about 0.24 cm, for $La_{0.99}Ca_{0.042}PO_{3.979} \bullet 0.021H_2O$, to ensure approximately 90% neutron transmission. The initially hydrated sample, $La_{0.99}Ca_{0.042}PO_{3.979} \bullet 0.021H_2O$, was heated inside the QENS sample cell at 150°C under dry gas for several hours to guarantee there was no surface water on the sample. To maintain sample hydration level during QENS measurements, a wet gas flow system was used. The wet (or subsequently dry) He gas entered the inner quartz tube through the inlet and was delivered to the sample inside the Pt sample holder. The energy spectra were collected at different scattering angles and combined into nine groups resulting in averaged Q values from 0.3 Å^{-1} to 1.9 Å^{-1}. Spectra were taken at 4 temperatures between 150°C and 500°C. The sample was then fully dehydrated by dwelling for 10 hours at 950°C under dry He flowing gas conditions. Spectra were again recorded at the same 4 temperatures in a dry He atmosphere. For background measurement, an empty platinum can inside the flow gas system was measured at 30°C and 500°C under wet and dry He conditions. The data was reduced with BASIS in-house routines. Measured data were normalized to an annular vanadium standard. The

DAVE software package (Azuah et al. (2009)) and an in-house routine were used to analyze the data.

The goals of this work were not only to find the correlation between the aliovalent alkaline-earth oxide's local structure and the phosphate family's measured dynamics properties but also to model the proton dynamics and proton transfer path in the lanthanum orthophosphate ($LaPO_4$).

Chapter 5

Structure and Dynamics Investigation

Monoclinic monazite $LaPO_4$ crystallizes in space group $P2_1/n$ (No.14) with a melting point of 2072°C (Hikichi and Nomura (1987)). According to Boatner (2002), the name monazite is originally from the Greek word *monazein*, meaning "to be alone".The crystal structure is composed of isolated PO_4 tetrahedra (Figure 5.1) and La^{3+} coordination polyhedra associated with nine oxygen ions. Mogilevsky et al. (2007) and Kim et al. (2011) reported $LaPO_4$ has high temperature stability, low thermal conductivity, and a high thermal expansion coefficient, and the structure of $LaPO_4$ is related to these features. In this chapter we will present and discuss the results of structure and dynamics investigation we conducted using X-ray diffraction (XRD), Neutron powder diffraction (NPD), Scanning Electron Microscopy (SEM), Electrochemical Impedance Spectroscopy (EIS), and Quasi-elastic neutron scattering (QENS).

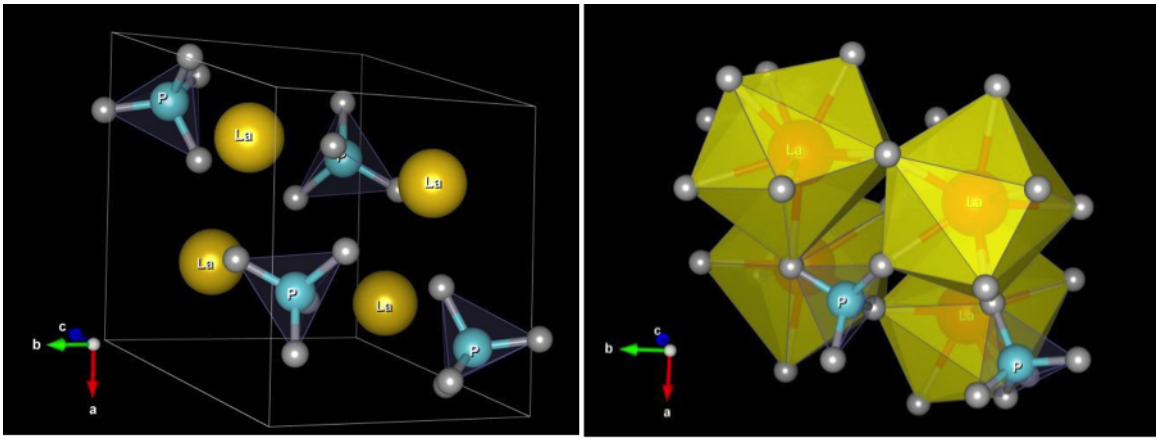


Figure 5.1: Left: the unit cell of $LaPO_4$ which has a monoclinic $P2_1/n$ structure containing four formula units,. The unit cell contains La^{3+} cations (yellow) and isolated PO_4 tetrahedra (O in grey and P in blue). Right: La^{3+} coordination polyhedra associated with nine oxygen ions.

5.1 X-ray diffraction (XRD)

The X-ray diffraction (XRD) data we obtained are showin in figures 5.2, 5.3 and 5.4, and they demonstrate the phase purity of the $LaPO_4$, $La_{0.99}Sr_{0.01}PO_4$, $La_{0.958}Sr_{0.042}PO_4$ (QENS sample); $La_{0.99}Ca_{0.01}PO_4$; and hydrated $La_{0.958}Ca_{0.042}PO_4$ (QENS sample) samples, respectively. The lack of observed impurity phases in the XRD data suggests that calcium/strontium has been successfully doped into the lattice. The patterns were indexed according to the monoclinic structure of the parent compound $LaPO_4$ (PDF 00-032-0493), and the lattice parameters were derived from a Rietveld refinement of the data using FullProf software Carvajal (1993). The refined unit cell's parameters, volumes, and densities are listed in Table 5.1. The values of the cell parameters agree with the values of the published Pearson's crystal data $LaPO_4$ (database code #383660) up to 0.1% percent difference. The obtained values of the lattice parameters of the doped are similar to those of the parent sample ($LaPO_4$) up to 0.08% percent difference. The lattice parameters are similar to those of $LaPO_4$, as expected from the similar ionic radii of the La^{3+} and Ca^{2+}/ Sr^{2+} cations. The Ca-doped $LaPO_4$ samples have interesting volume and density cell percentage differences

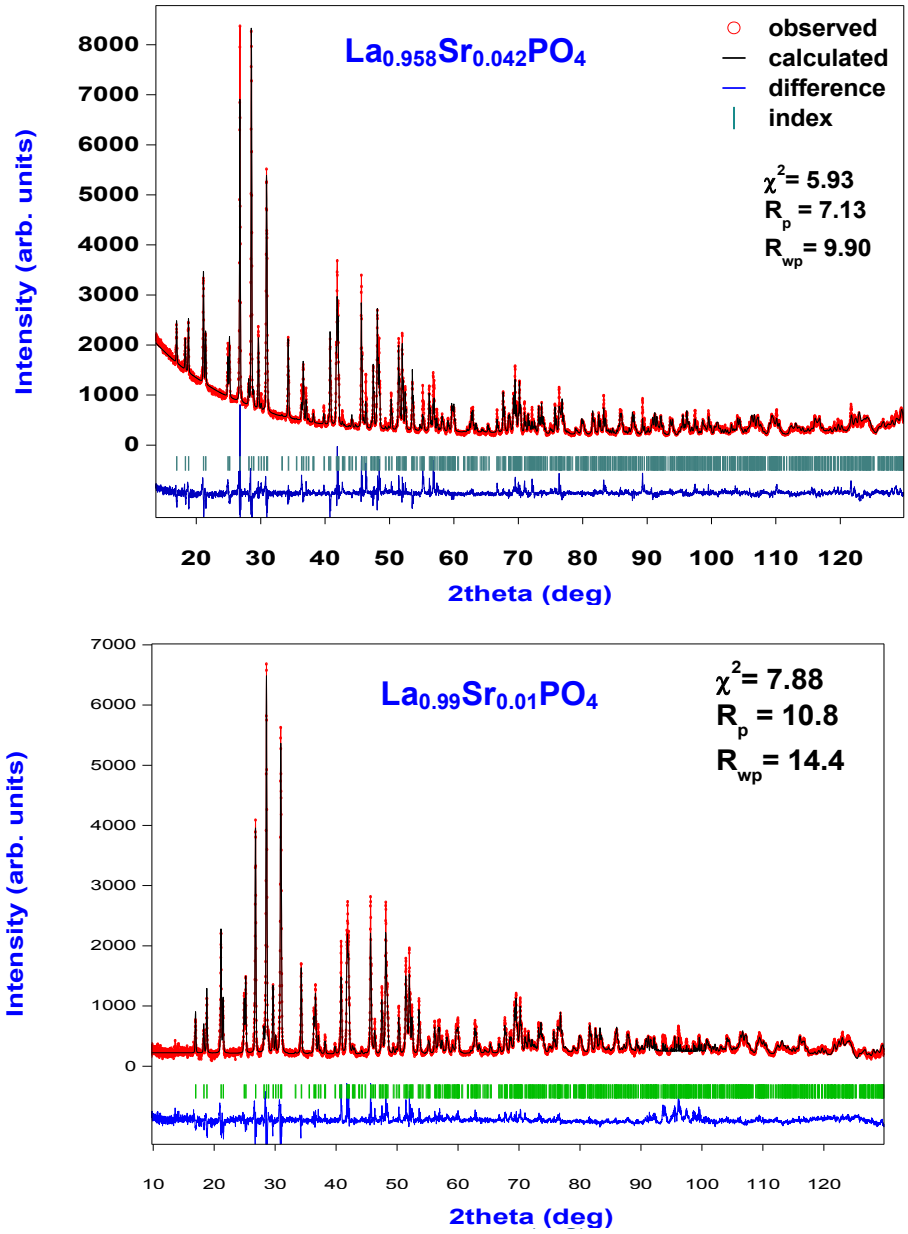


Figure 5.2: Rietveld refinement results obtained from the X-ray powder diffraction data for hydrated $La_{0.958}Sr_{0.042}PO_4$ (no background subtraction) and $La_{0.99}Sr_{0.01}PO_4$ (after background subtraction) sintered at 1200°C. The XRD pattern at room temperature was conducted at the CNMS User Facility at ORNL.

compared to those of the $LaPO_4$ sample. The $La_{0.99}Ca_{0.01}PO_4$ and $La_{0.958}Ca_{0.042}PO_4$ have a volume cell and density cell comparable to $LaPO_4$ with 0.07% and 0.49% and 0.05% and 1.72% percent difference, respectively. The $La_{0.958}Sr_{0.042}PO_4$ (synthesis by

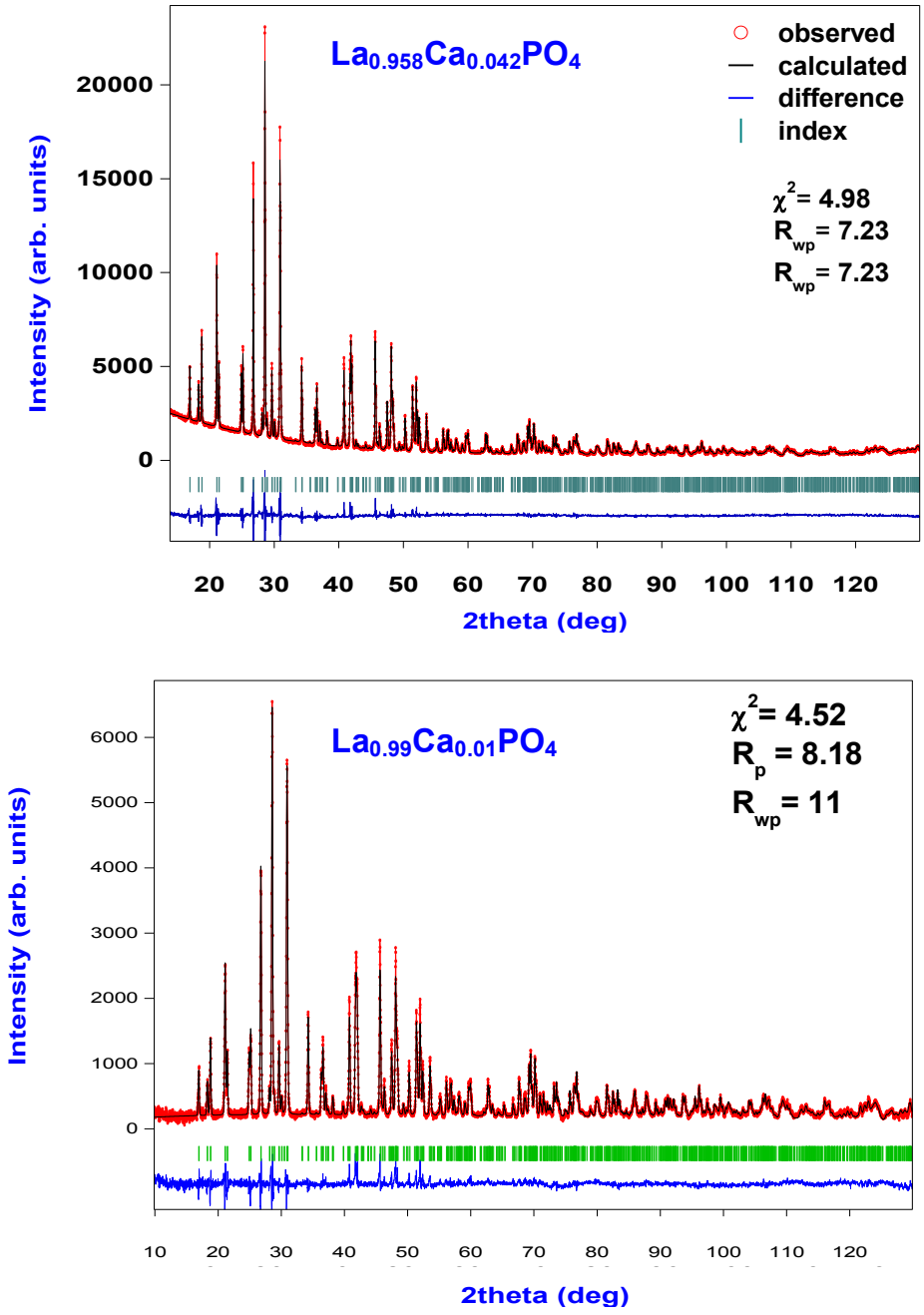


Figure 5.3: Rietveld refinement results obtained from the X-ray powder diffraction data for hydrated $La_{0.958}Ca_{0.042}PO_4$ (no background subtraction) and $La_{0.99}Ca_{0.01}PO_4$ (after background subtraction) sintered at 1200°C. The XRD pattern at room temperature was conducted at the CNMS User Facility at ORNL.

Table 5.1: The XRD cell parameters and cell volume for x%Sr/Ca-doped $LaPO_4$ ($x = 0, 1$, and 4.2) at room temperature. *$LaPO_4$ published Pearson's crystal data #383660. **$LaPO_4$ sample sintered at 1000°C; the remaining samples sintered at 1200°C.

Samples	a (Å)	b (Å)	c (Å)	β(°)	V (Å^3)	ρ(g/cm)
*$LaPO_4$	6.8370(10)	7.0770(10)	6.510(1)	103.2400(0)	306.620(0)	—
**$LaPO_4$	6.8377(16)	7.0745(2)	6.50890(2)	103.2765(16)	306.443(12)	5.069
$LaPO_4$	6.8396(0)	7.0761(0)	6.5099(0)	103.2746(11)	306.644(7)	5.066
4.2%Sr	6.8388(05)	7.0760(05)	6.5117(06)	103.2893(6)	306.673(4)	5.096
1%Sr	6.8394(0)	7.0722 (0)	6.5122 (0)	103.3067(11)	306.538(7)	5.057
4.2%Ca	6.8389(4)	7.0718(04)	6.5119(04)	103.2954(4)	306.498(3)	4.979
1%Ca	6.8409(0)	7.0752(0)	6.5149 (0)	103.3051(7)	306.866(5)	5.041

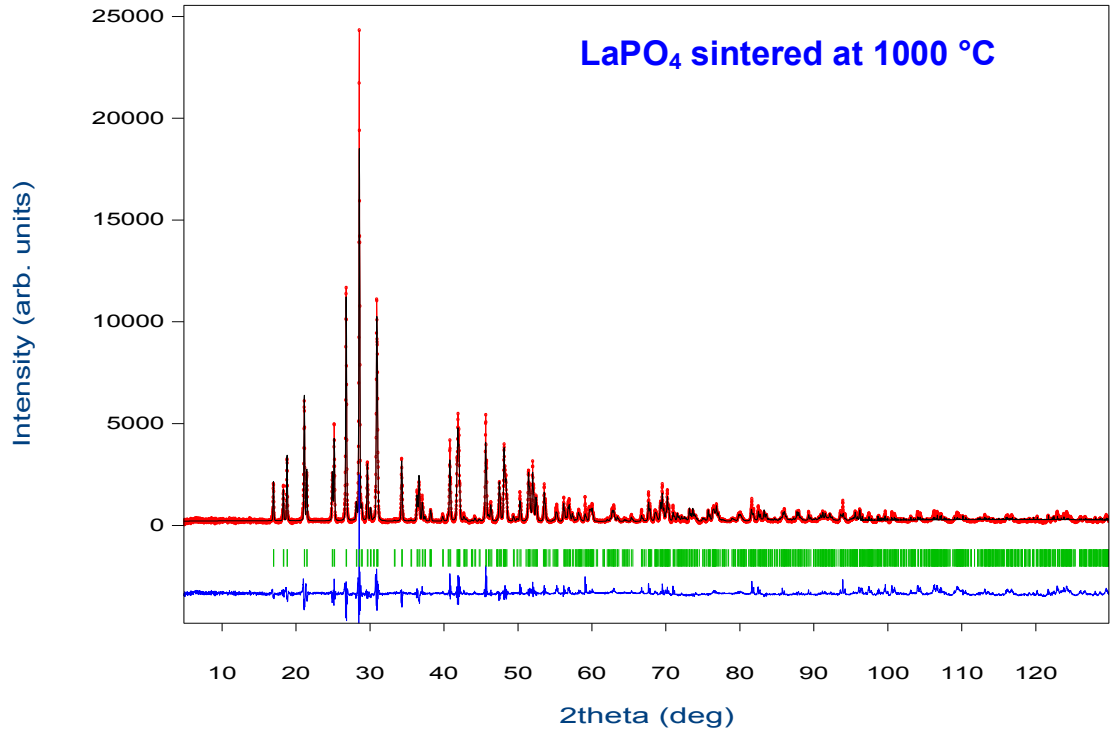


Figure 5.4: Rietveld refinement results obtained from the X-ray powder diffraction data for $LaPO_4$ at room temperature. The XRD pattern was conducted at the CNMS User Facility at ORNL.

CPT) and $La_{0.958}Ca_{0.042}PO_4$ (synthesis by SSR) have the higher and lower density value, respectively. Given the similar size of the cations, it seems that there is not

a clear trend. The differences are noted, they are within the variation of the values due to the small size differences.

According to Amezawa et al. (2001), oxygen vacancies resulting from Ca/Sr doping in the monazite-type lanthanum orthophosphate, $LaPO_4$, may lead to the formation of pyrophosphate-type defects. The signature of P_2O was noticed in Sr-doped $LaPO_4$ by Fourier transform Raman and magic-angle spinning nuclear magnetic resonance spectroscopy experiments.

When hydrating the pyrophosphate by post-annealing under water vapor, protons dissolve into phosphates, forming hydrogen phosphate. As a result, protons stay at PO_4 tetrahedra in the sample Amezawa et al. (2001); Yu and Jonghe (2007); Toyoura et al. (2012); Phadke et al. (2012); Solomon et al. (2014).

To explore the structure and defect structure of aliovalent (Sr, Ca) doping on $LaPO_4$ materials, the inter-ionic bond lengths (Å) and the angles (°) between the phosphorus ions and the oxygen ions in the $LaPO_4$ samples from the XRD experiment at RT were determined. Also, each sample's average bond lengths between the Lanthanum and oxygen ion as well as the distance between two phosphorus ions were obtained and are listed in Table 5.2. All the samples sintered at 1200°C, and

Table 5.2: The inter-ionic bond lengths (Å) between the phosphorus ions and the oxygen ions in the $LaPO_4$ samples from the XRD experiment at RT. Average bond lengths between the Lanthanum and oxygen ion as well as the distance between two phosphorus ions are listed for each sample. All the samples sintered at 1200°C, and the doped sample sintered under water vapor.

	$LaPO_4$	1%Ca	4.2% Ca	1% Sr	4.2% Sr
P−O1 (Å)	1.500(20)	1.534(11)	1.494(11)	1.458(14)	1.426(18)
P−O2 (Å)	1.480(30)	1.567(14)	1.609(13)	1.633(17)	1.613(19)
P−O3 (Å)	1.470(30)	1.589(14)	1.549(13)	1.640(30)	1.580(30)
P−O4 (Å)	1.629(18)	1.576(10)	1.547(10)	1.573(13)	1.591(14)
La−O (Å)	2.570(11)	2.620(13)	2.603(11)	2.654 (15)	2.449(21)
P−P (Å)	4.110(9)	4.110(9)	4.105(7)	4.127(13)	4.113(12)

the 1 and 4.2% Sr/Ca doped $LaPO_4$ samples sintered under water vapor. Several studies, like Amezawa et al. (2001); Yu and Jonghe (2007); Toyoura et al. (2012);

Phadke et al. (2012); Solomon et al. (2014), have shown the proton sitting on the PO_4 tetrahedron.

Inter-ionic bond length between the phosphorus ion and the oxygen ion might reveal significant information about the proton-oxygen bond length. According to Phadke et al. (2012), the presence of charged defects (oxygen vacancies or protonic defects) in a lattice can cause displacement or relaxation of the positions of the surrounding lattice ions Phadke et al. (2012). The influence of the displacement or relaxation is demonstrated by inter- ionic bond length changes of the ions Phadke et al. (2012). The oxygen vacancies are equivalent to the formation of P_2O_7 pyrophosphate groups in the doped $LaPO_4$ structure by post annealing under dry atmospheres Amezawa et al. (2001); Phadke et al. (2012). In this case, an oxygen ion is shared between two adjacent PO_4 tetrahedra. When the oxygen ion is in the vertex between two PO_4 tetrahedra, the inter-ionic P−O bond length is defined as a bridging oxygen bond (Ob) Phadke et al. (2012). According to Phadke et al. (2012) the oxygen sharing induces remarkable distortion of the PO_4 tetrahedra participating in the sharing process; thus, significant stretching of the bridging P−Ob bonds has been observed as illustrated in Figure 5.5. Phadke et al. (2012) calculated average bond lengths P−O, P−P and La−O length 1.564 Å, 4.187 Å and 2.621 Å, respectively, in the orthophosphate $[PO_4]^{3-}$ and compare it with XRD result obtained previously by the same group Phadke et al. (2012); Phadke and Nino (2011). The pyrophosphate group $[P_2O_7]^{4-}$ in the doped $LaPO_4$ showed bridging oxygen ion (Ob) and P−Ob and P−P bond lengths around 1.718 Å and 3.175 Å, respectively. For the protonic defect, the protonated orthophosphate group $[HPO_4]^{3-}$ in $LaPO_4$ also showed the P−O bond lengths up to 1.882 Å.

To investigate if proton oxygen preference sites were on the samples, the bond length between the phosphorus ions and the oxygen ions was examined in $LaPO_4$, $La_{0.99}Ca_{0.01}PO_4$ (wet), $La_{0.958}Ca_{0.042}PO_4$ (wet), $La_{0.958}Sr_{0.042}PO_4$ (wet) and $La_{0.99}Sr_{0.01}PO_4$ (wet) samples. The theoretical study of Phadke et al. (2012) will be compared to the present study's XRD results and later to our NPD results. For the

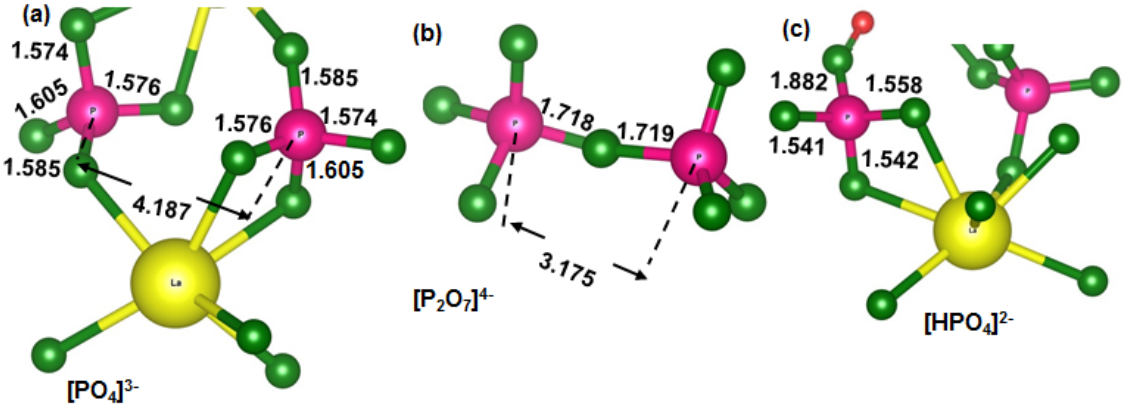


Figure 5.5: (a) Orthophosphate $[PO_4]^{3-}$ where the average calculated P−O, P−P, and La−O length is 1.564 Å, 4.187 Å, and 2.621 Å, respectively. (b) Pyrophosphate group $[P_2O_7]^{4-}$ in the doped $LaPO_4$ showing bridging oxygen ion (Ob) and P−Ob and P−P bond lengths around 1.718 Å and 3.175 Å, respectively. (c) Protonated orthophosphate group $[HPO_4]^{3-}$ in $LaPO_4$ also showing the P−O bond lengths up to 1.882 Å and that of P−P_{adj} to be 4.179 Å. Reproduce from Phadke et al. (2012).

$LaPO_4$ sample, the calculated average bond of La−O is 2.621 Å; the bond length distance between two phosphorus ions is 4.187 Å; and the values of the bond length between phosphorus ion and oxygen ion O1, O2, O3, and O4 are 1.574, 1.576, 1.585 and 1.605 Å, respectively.

Based on this study's results, the average $LaPO_4$ bond of La−O is 2.57(11) Å, the bond length distance between two phosphorus ions is 4.110(9) Å; and the values of the bond length between phosphorus ion and oxygen ion O1, O2, O3, and O4 are 1.500(20), 1.480(30), 1.470(30) and 1.629(18) Å, respectively. This study's results of La−O, and P−P bond lengths agree with those from the calculated ones Phadke et al. (2012). The difference between the calculated and the experimental results for the phosphorus ion and oxygen ion bond lengths are $\Delta_1 = 0.054$ Å, $\Delta_2 = 0.066$ Å, $\Delta_3 = 0.085$ Å, and $\Delta_4 = 0.042$ Å. The inter-ionic bond lengths between the phosphorus ions and the oxygen ions in Table 5.2 show the minimum value at P−O1 for each doped sample. P−O1 value is up to 1.53 Å. The maximum inter-ionic bond length for 4.2%Ca-doped $LaPO_4$ is P−O2 = 1.609(13) Å.

The maximum inter-ionic bond length for 4.2%Sr-doped $LaPO_4$ is for P−O2 = 1.613(19) Å. For lower doping, such as 1%Ca/Sr doped $LaPO_4$, the maximum inter-ionic bond length is P−O3 with 1.589(14) and 1.640(30) Å, respectively. It is likely that the proton on the 4.2%Ca/Sr-doped $LaPo_4$ prefers to reside on O2, while for 1%Sr/Ca-doped $LaPO_4$ the proton preference site on O3.

5.2 Neutron Powder Diffraction (NPD)

Studying the structure and defect structure of aliovalent (Sr, Ca,) doping on lanthanum orthophosphate ($LaPO_4$) materials by neutrons diffraction provides accurate information about structures, impurities, and the presence of oxygen vacancies under dry or wet atmospheres at various temperatures. The least-squares refinement procedure provides atomic information, such as fractional occupancy and thermal parameters.

The contribution of an atom location in real space to the neutron scan patterns' reflection is determined by the structure factor of that reflection, enabling the Debye-Waller factor to be determined. Refining thermal parameters with X-ray diffraction is challenging, while in neutron diffraction the chances are far better. A neutron powder diffraction analysis of bond lengths and inter-ionic distances is performed to check the XRD results consistency for the $LaPO_4$, and the doped samples as well as to gain more information about the dopant-defect interactions, which play a role in proton mobility. Data were collected at 300 K for the parent compound $LaPO_4$ and dry and hydrated Ca-doped $LaPO_4$. To decrease the incoherent background (in the NPD incoherent signal treated as noise) and to improve the signal to noise, the sample was hydrated using D_2O instead of H_2O. Table 5.3 contains detailed information about the NPD cell parameters and cell volumes for x% Ca-doped $LaPO_4$ ($x = 0, 1$, and 4.2) at room temperature. The NPD results for the sample parameter cells (Table 5.3) and the XRD results (Table 5.1) agree. Comparing the undoped, dry, and hydrated Ca-doped $LaPO_4$ samples (see Table 5.4), a slightly change is seen in the inter-ionic bond

Table 5.3: The NPD cell parameters and cell volume for x%Ca-doped $LaPO_4$ ($x = 0, 1$, and 4.2) at room temperature.

	$LaPO_4$	1% Ca (D_2O)	4.2% Ca (D_2O)	4.2% Ca (Dry)
a (Å)	6.84022(4)	6.84005(4)	6.84088(4)	6.84013(4)
b (Å)	7.07474(4)	7.07364(4)	7.07225(5)	7.07339(5)
c (Å)	6.51227(4)	6.51374(4)	6.51387(4)	6.51348(4)
β (°)	103.2840(5)	103.2965(5)	103.3011(6)	103.2915(6)
V(Å^3)	306.715(3)	306.713(3)	306.690(3)	306.699(3)
ρ (g/cm^3)	5.041	5.010	4.922	4.914

lengths between the phosphorus ions and the oxygen ions in the NPD experiment at 300 K. However, the XRD results are significantly different. Analysis of NPD data gives precise definition of the oxygen location in the presence of the heavier elements, obtained from the relatively large scattering length of oxygen. Although the phosphorus approximately is just twice the weight of the oxygen, still the neutron diffraction provides the most accurate information related to O−P phosphorus bonds than the XRD. The average bond lengths P−P and La−O for undoped, dry, and hydrated samples from the NPD experiment (Table 5.4) agree with the results from the XRD.

Temperature-dependent neutron diffraction on hydrated samples of $La_{0.958}Ca_{0.042}PO_4 \bullet nD_2O$ and $La_{0.958}Sr_{0.042}PO_4 \bullet nH_2O$ was measured under dry air. Observed and calculated patterns of $La_{0.958}Ca_{0.042}PO_4 \bullet nD_2O$ and $La_{0.958}Sr_{0.042}PO_4 \bullet nH_2O$ at 18°C, 26°C, 35°C, 500°C, 800°C and at 60°C, 70°C, 180°C, 260°C, 360°C and 500°C, respectively, are illustrated in Figures 5.6, 5.9 and 5.10. Refinement of the neutron data (including scale factors, background coefficients, profile functions and parameters, atomic position parameters, and atomic displacement parameters) smoothly converged to determine a reasonable solution with a goodness of fit $\chi^2 < 8$ for each datasets. At room temperature, the parameter cells and cell volume of the NPD results (as shown in Tables 5.5 and 5.6) are very consistent with those of XRD.

Table 5.4: The inter-ionic bond lengths (Å) and angles (°) between the phosphorus ions and the oxygen ions in the $LaPO_4$ samples from the NPD experiment at 300 K. Average bond lengths between the Lanthanum and oxygen ion and the distance between the two phosphorus ions are listed for each sample. All the samples sintered at 1200°C.

	$LaPO_4$	1% Ca (D_2O)	4.2% Ca (D_2O)	4.2% Ca (Dry)
P−O1	1.5353(16)	1.5356(17)	1.5360(18)	1.5367(18)
P−O2	1.5558(16)	1.5544(16)	1.5540(17)	1.5559(17)
P−O3	1.5377(13)	1.5372(14)	1.5368(14)	1.5376(14)
P−O4	1.5257(14)	1.5264(14)	1.5266(15)	1.5254(15)
La−O (Å)	2.5889(12)	2.5695(1)	2.6024(1)	2.6022(1)
P−P (Å)	4.1096(17)	4.1106(18)	4.1104(19)	4.1093(19)
(O1−P−O2)	105.10(14)	105.15(14)	105.15(15)	105.04(15)
(O1−P−O3)	113.63(15)	113.53(15)	113.54(15)	113.45(15)
(O1−P−O4)	112.26(14)	112.16(14)	112.13(14)	112.28(14)
(O2−P−O3)	107.78(13)	107.91(14)	107.91(14)	107.85(14)
(O2−P−O4)	113.80(14)	113.91(15)	113.95(15)	113.99(15)
(O3−P−O4)	104.41(14)	104.32(14)	104.31(15)	104.37(15)

Table 5.5: The NPD cell parameters and cell volumes of $La_{0.958}Ca_{0.042}PO_4$ (D_2O) from $T = 18$°C to 800°C under dry air.

T(°C)	a (Å)	b (Å)	c (Å)	β (°)	V(Å^3)
18	6.84046(7)	7.07166(7)	6.51492(7)	103.3131(8)	306.680(6)
RT	6.84137(8)	7.07242(8)	6.51576(7)	103.3138(8)	306.793 (0)
35	6.84157(6)	7.07258(6)	6.51606(6)	103.3136(7)	306.823(5)
500	6.86962(8)	7.09762(8)	6.54700(8)	103.3368(8)	310.609(6)
800	6.89060(30)	7.11540(30)	6.56910(30)	103.3615(9)	313.360(20)

Table 5.6: The NPD cell parameters and cell volumes of $La_{0.958}Sr_{0.042}PO_4$ (H_2O) from $T = 60$°C to 500°C under dry air.

T(°C)	a (Å)	b (Å)	c (Å)	β (°)	V(Å^3)
60	6.84169(8)	7.07405(8)	6.51660(7)	103.3090(8)	306.923(6)
70	6.84249(12)	7.07461(12)	6.51737(11)	103.3092(13)	307.019(9)
180	6.84831(9)	7.08010(9)	6.52450(9)	103.3130(9)	307.850(7)
260	6.85301(9)	7.08438(10)	6.52990(9)	103.3171(10)	308.498(7)
360	6.85894(9)	7.08975(10)	6.53672(9)	103.3225(9)	309.314(7)
500	6.86838(10)	7.09806(11)	6.54733(10)	103.3306(10)	310.596(8)

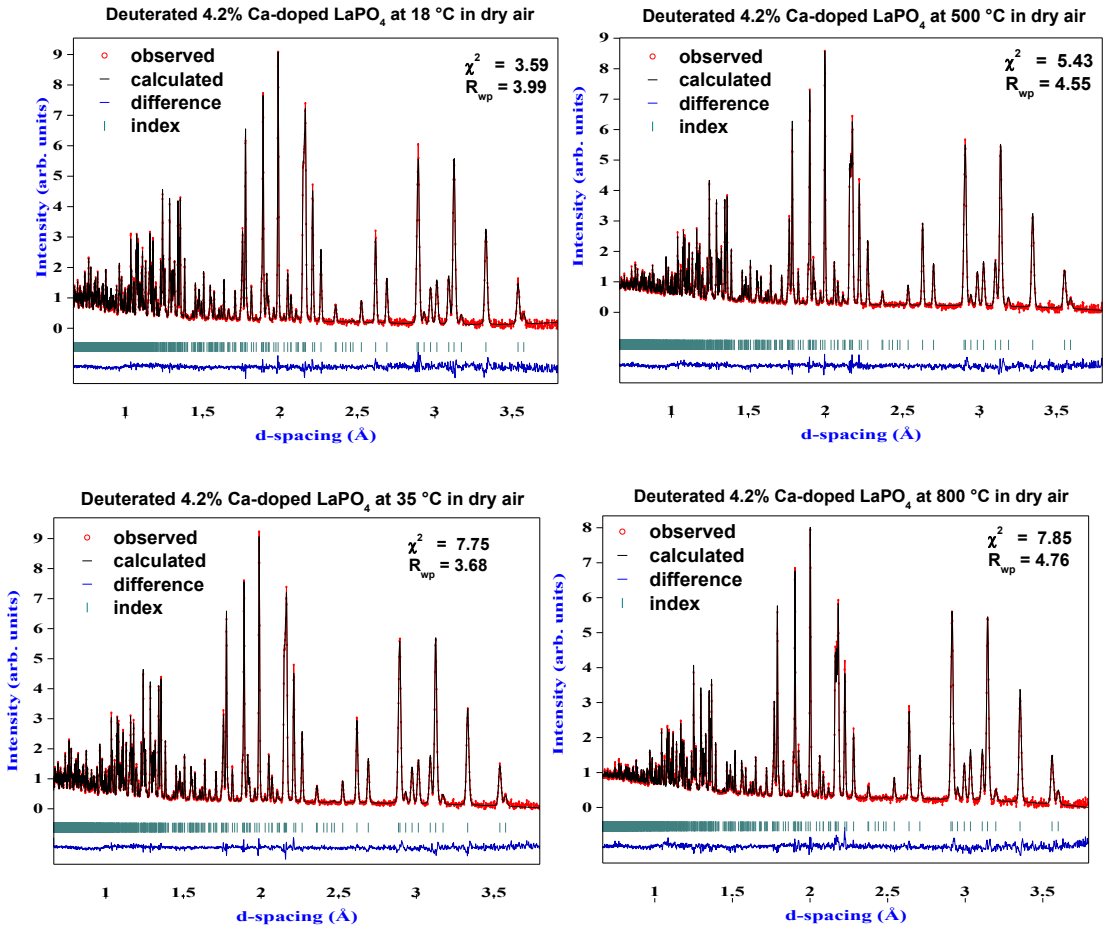


Figure 5.6: Rietveld refinement results obtained from the neutron powder diffraction data for hydrated $La_{0.958}Ca_{0.042}PO_4$ (D_2O) at 18, 35, 500, and 800°C. The NPD patterns were conducted at POWGEN, SNS at ORNL.

As the temperature increases, the cell parameters and volumes expand as shown in figures 5.7 and 5.8.. This expansion's percentage difference from RT to 500°C for Ca-doped samples a, b, c, β and the volume cell values is 0.40%, 0.35%, 0.48%, 0.02%, and 1.24%, respectively. The thermal behavior of the cell parameters a, b, and c axis and volume cell are almost linear as a function of temperature for the Ca and Sr doped $LaPO_4$ as shown in figure 5.7 and 5.8, respectively.

Dense electrolyte samples have the potential to exist as self-supported structures at high temperatures during solid fuel cell operation. Thermal expansion was fitted to a linear model, which was conducted by weighted least-squares fitting. The weight

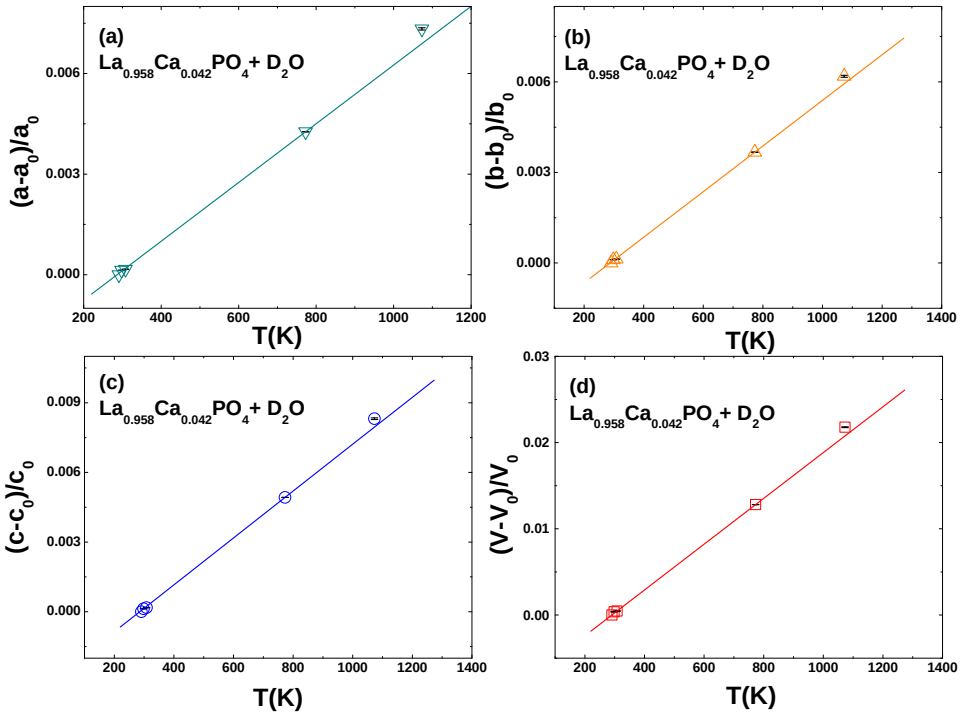


Figure 5.7: Detailed temperature dependence of the lattice constants for $La_{0.958}Ca_{0.042}PO_4$ (D_2O). $\Delta x/x_0$ is $[x(T) - x_0(T = 291\ \mathrm{K})]/\mathrm{x_0(T = 291\ K)}$ where $x = a(\text{Å}), \mathrm{b(Å)}, \mathrm{c(Å)and V(Å^3)}$ for (a), (b), (c) and (d) respectively. The Thermal expansions are linear for cell parameters in the temperature range from RT to 800°C.

for each point was the reciprocal of square error in the fractional expansion. Morgan and Marshall (1995) measured the thermal expansion properties of $LaPO_4$ by using a bar cut from a sample fabricated by hot pressing at 1300°C. They determined the coefficient of thermal expansion to be $7.5 \times 10^{-6\circ}\mathrm{C}^{-1}$ at 20°C and $10.5 \times 10^{-6\circ}\mathrm{C}^{-1}$ at 1000°C and the average thermal expansion over the temperature range was $9.6 \times 10^{-6\circ}\mathrm{C}^{-1}$. The Thermal expansion coefficients of the present study are on the same order as those reported previously for the $LaPO_4$ sample by Morgan and Marshall (1995).

The Sr-doped $LaPO_4$ have higher thermal expansion than Ca-doped $LaPO_4$ as shown in Table 5.7. In general the thermal expansion coefficient is increased with an increase in the fractional ionic character between bonded atoms in crystal structures Matsuda (2004). The fractional ionic character and the electronegativity difference

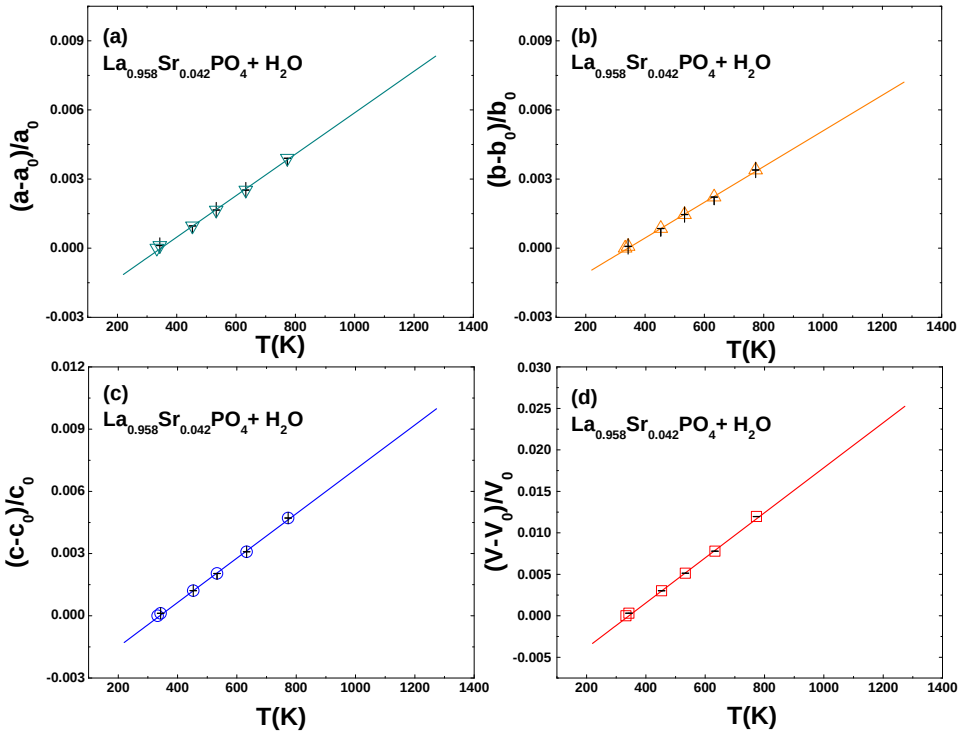


Figure 5.8: Detailed temperature dependence of the lattice constants for $La_{0.958}Sr_{0.042}PO_4$ (H_2O). $\Delta x/x_0$ is $[x(T) - x_0(T = 333\ \text{K})]/\text{x}_0(\text{T} = 333\ \text{K})$ where $x = a(\text{Å}), \text{b}(\text{Å}), \text{c}(\text{Å})\text{and}\text{V}(\text{Å}^3)$ for (a), (b), (c) and (d) respectively. The Thermal expansions are linear for cell parameters in the temperature range from 60°C to 500°C.

Table 5.7: $La_{0.958}Ca_{0.042}PO_4(D_2O)$ and $La_{0.958}Sr_{0.042}PO_4(H_2O)$ thermal expansion coefficients.

Thermal expansion (K^{-1})	$La_{0.958}Ca_{0.042}PO_4(D_2O)$	$La_{0.958}Sr_{0.042}PO_4(H_2O)$
$\alpha_a \pm \Delta\alpha_a$	$(8.75 \pm 0.082) \times 10^{-6}$	$(8.9 \pm 0.22) \times 10^{-6}$
$\alpha_b \pm \Delta\alpha_b$	$(7.55 \pm 0.070) \times 10^{-6}$	$(7.7 \pm 0.14) \times 10^{-6}$
$\alpha_c \pm \Delta\alpha_c$	$(10.09 \pm 0.081) \times 10^{-6}$	$(10.7 \pm 0.23) \times 10^{-6}$
$\alpha_\beta \pm \Delta\alpha_\beta$	$(0.4687 \pm 0.00027) \times 10^{-6}$	$(0.52 \pm 0.016) \times 10^{-6}$
$\alpha_V \pm \Delta\alpha_V$	$(26.5 \pm 0.12) \times 10^{-6}$	$(27.1 \pm 0.64) \times 10^{-6}$

between Sr-site cation and the oxygen are 0.888 and 2.962 while for the Ca-site cation and oxygen is 0.870 and 2.857, respectively Singh et al. (2009). Maybe the higher electronegativity of the Sr compared to the Ca, can be related to the higher conductivity of the Sr- compared to the conductivity of the Ca-doped samples. The fractional ionic character depends upon the electronegativity difference between

Sr/Ca-site cation and the oxide ion through the covalent bond in the tetrahedral structure, which best described by the following equation

$$f_{iO} = 1 - \exp\left(-\frac{(\chi_i - \chi_O)^2}{4}\right) \tag{5.1}$$

where f_{iO} is the fractional ionic character between i = Sr or Ca and O atoms, and χ_i and χ_O are the electronegativities of Sr/Ca and O atoms, respectively.

Table 5.8 and 5.9 give the inter-ionic bond lengths (Å) and angles (°) between the phosphorus ions and the oxygen ions in the 4.2%Ca-doped $LaPO_4(D_2O)$ and

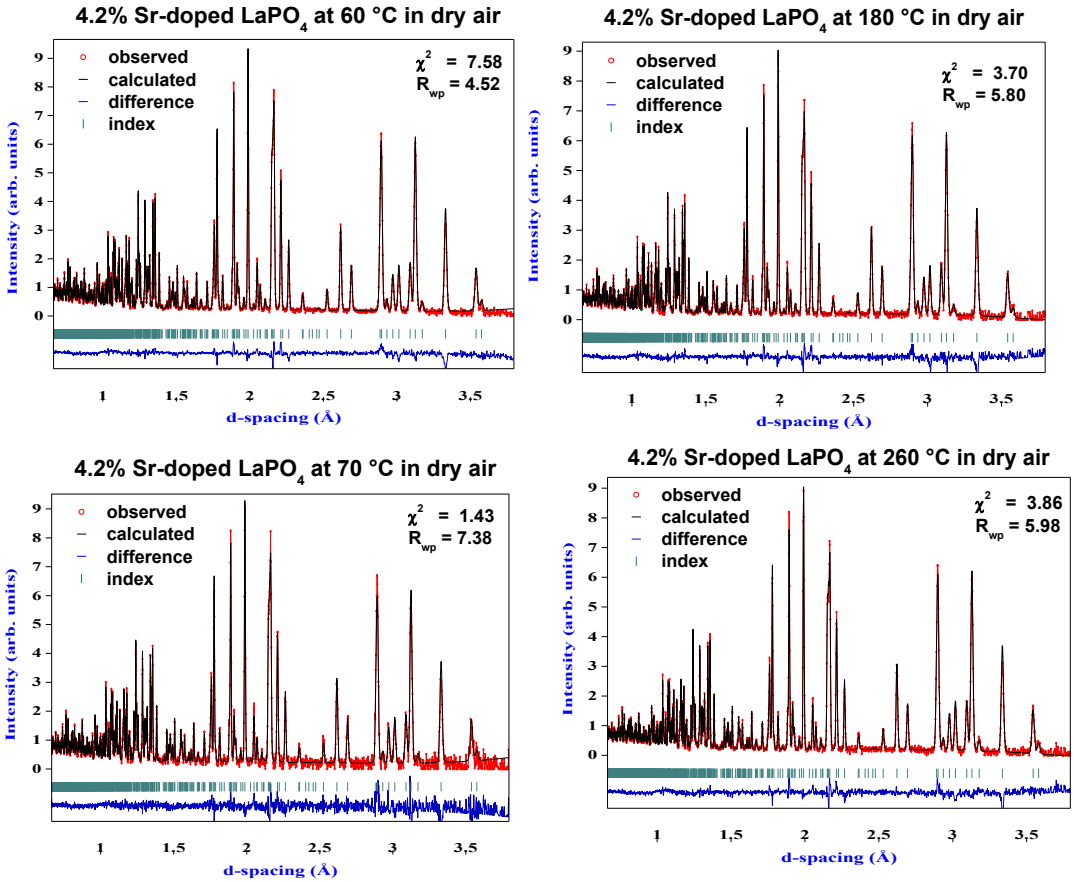


Figure 5.9: Rietveld refinement results obtained from the neutron powder diffraction data for hydrated $La_{0.958}Sr_{0.042}PO_4$ (H_2O) at 60, 70, 180, and 260°C. The NPD patterns were conducted at POWGEN, SNS at ORNL.

4.2%Sr-doped $LaPO_4(H_2O)$ samples from NPD experiment at elevated temperature from 18°C to 800°C and from 60°C to 500°C, respectively. The percent difference of P−O1, P−O2, P−O3, and P−O4 in the 4.2%Ca-doped $LaPO_4(D_2O)$ between 18°C to 800°C are 0.6%, 0.7%, 0.2% and 1.6%, respectively.

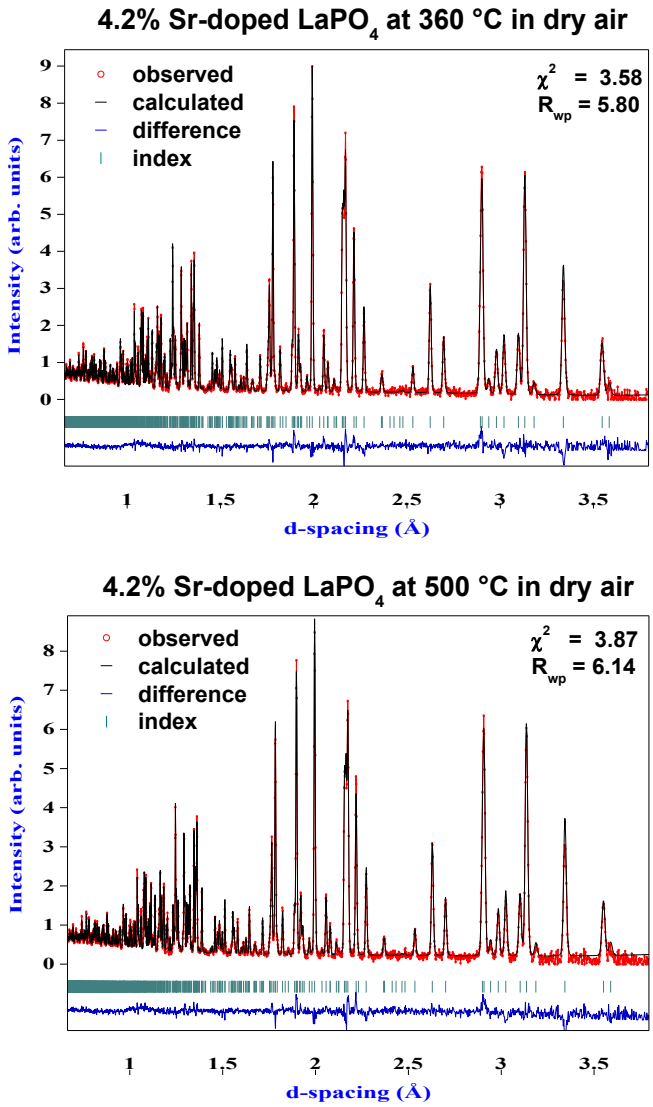


Figure 5.10: Rietveld refinement results obtained from the neutron powder diffraction data for hydrated $La_{0.958}Sr_{0.042}PO_4$ (H_2O) at 360 and 500°C. The NPD patterns were conducted at POWGEN, SNS at ORNL.

Table 5.8: The inter-ionic bond lengths (Å) and angles (°) between the phosphorus ions and the oxygen ions in the 4.2% Ca-doped $LaPO_4(H_2O)$ samples from NPD experiment at elevated temperature from 18°C to 800°C.

4.2%Ca-doped $LaPO_4(D_2O)$					
	18°C	RT	35°C	500°C	800°C
P−O1	1.538(3)	1.538(3)	1.538(3)	1.533(4)	1.529(5)
P−O2	1.546(3)	1.548(3)	1.548(3)	1.549(4)	1.535(5)
P−O3	1.535(2)	1.537(3)	1.536(2)	1.532(3)	1.532(5)
P−O4	1.528(2)	1.525(3)	1.526(2)	1.528(3)	1.552(5)
Angle (°)					
(O1−P−O2)	105.18(16)	105.26(19)	105.27(16)	105.20(30)	105.10(30)
(O1−P−O3)	113.37(17)	113.37(19)	113.43(17)	114.10(30)	114.00(30)
(O1−P−O4)	112.12(16)	112.26(18)	112.29(16)	112.51(18)	112.50(30)
(O2−P−O3)	107.94(16)	107.87(18)	107.89(16)	107.92(18)	108.10(30)
(O2−P−O4)	114.09(16)	114.06(19)	114.04(16)	113.30(30)	113.10(30)
(O3−P−O4)	104.29(16)	104.16(19)	104.05(16)	104.00(30)	104.20(30)

Table 5.9: The inter-ionic bond lengths (Å) and angles (°) between the phosphorus ions and the oxygen ions in the 4.2%Sr-doped $LaPO_4(H_2O)$ samples from NPD experiment at elevated temperature from 60°C to 500°C.

4.2%Sr-doped $LaPO_4(H_2O)$						
	60°C	70°C	180°C	260°C	360°C	500°C
P−O1	1.541(3)	1.538(5)	1.539(4)	1.541(4)	1.541(4)	1.537(5)
P−O2	1.543(3)	1.541(4)	1.540(4)	1.541(4)	1.545(4)	1.544(4)
P−O3	1.530(3)	1.524(4)	1.524(3)	1.526(3)	1.527(3)	1.525(4)
P−O4	1.517(3)	1.525(4)	1.517(3)	1.518(3)	1.516(4)	1.518(4)
Angle (°)						
(O1−P−O2)	105.07(18)	105.10(30)	105.19(19)	105.19(19)	105.10(30)	105.10(30)
(O1−P−O3)	113.40(20)	113.50(30)	113.70(20)	113.70(20)	113.70(30)	113.90(30)
(O1−P−O4)	112.48(18)	112.20(30)	112.40(20)	112.40(20)	112.50(30)	112.50(30)
(O2−P−O3)	107.94(18)	108.30(30)	108.10(19)	108.10(19)	108.10(30)	108.20(30)
(O2−P−O4)	113.83(19)	113.70(30)	113.60(30)	113.60(30)	113.60(30)	113.20(30)
(O3−P−O4)	104.23(18)	104.00(30)	104.10(20)	104.10(20)	104.10(30)	104.00(30)

All the inter-ionic bond lengths (Å) between the phosphorus ions and the oxygen ions in the 4.2%Ca-doped $LaPO_4(D_2O)$ are slightly decreasing except P−O4 is increasing from 18°C to 800°C. The percent difference of P−O1, P−O2, P−O3, and P−O4 in the 4.2%Ca-doped $LaPO_4(D_2O)$ between RT to 500°C are 0.3%, 0.1%,

0.3% and 0.2%, respectively. The percent difference of P−O1, P−O2, P−O3, and P−O4 in the 4.2%Sr-doped $LaPO_4(H_2O)$ between 60°C to 500°C are 0.3%, 0.1%, 0.3% and 0.1%, respectively.

The inter-ionic bond lengths (Å) between the phosphorus ions and the oxygen ions in the 4.2%Ca/Sr-doped $LaPO_4$ are slightly decreasing for P−O1 and P−O3 and slightly increased for P−O2 and P−O4 from RT to 500°C and from 60°C to 500°C, respectively.

The angle percentage difference between (O1−P−O2), (O1−P−O3), (O1−P−O4), (O2−P−O3), (O2−P−O4) and (O3−P−O4) for 4.2%Ca-doped $LaPO_4$ are 0.06%, 0.60%, 0.20%, 0.05%, 0.70%, and 0.15%, respectively between RT and 500°C. The angle percentage difference between (O1−P−O2), (O1−P−O3), (O1−P−O4), (O2−P−O3), (O2−P−O4) and (O3−P−O4) for 4.2%Sr-doped $LaPO_4$ are 0.03%, 0.44%, 0.02%, 0.24%, 0.55% and 0.22%, respectively between 60°C and 500°C.

Table 5.10 and 5.11 give fractional Atomic Coordinates and U is the equivalent isotropic displacement parameters ($Å^2$) for $La_{0.958}Ca_{0.042}PO_4$ (D_2O) and $La_{0.958}Sr_{0.042}PO_4$ (H_2O) at 18°C to 800°C and 60°C to 500°C, respectively, while Table 5.12 shows fractional Atomic Coordinates and U is the equivalent isotropic displacement parameters ($Å^2$) for hydrated and dry $La_{0.958}Ca_{0.042}PO_4$ (D_2O) at 300 K.

5.3 Scanning Electron Microscopy (SEM)

The grain size of the samples ranges from 1 to 2 μm, 1.0 to 2.5 μm, 0.1 to 4.5 μm and, for $LaPO_4$, 4.2% Ca-doped $LaPO_4$, 4.2% Sr-doped $LaPO_4$, respectively. The SEM images indicates a broad range of grain sizes, are presented in figure 5.11.

Table 5.10: $La_{0.958}Ca_{0.042}LaPO_4$ (D_2O): x, y and z are fractional Atomic Coordinates and U is the equivalent isotropic displacement parameters ($Å^2$) at 18°C to 800°C.

T(°C)		x	y	z	U
18	La/Ca	0.28193(14)	0.15950(18)	0.10085(17)	0.0073(3)
	P	0.30480(20)	0.1647(30)	0.6122(3)	0.0084(4)
	O1	0.24960(20)	0.00810(20)	0.44520(20)	0.0113(4)
	O2	0.38090(20)	0.3310(3)	0.49760(20)	0.0113(4)
	O3	0.47410(20)	0.10860(20)	0.8009(3)	0.0122(4)
	O4	0.1292(3)	0.21547(20)	0.7103(3)	0.0104(4)
500	La/Ca	0.28320(20)	0.16030(20)	0.10040(20)	0.0168(4)
	P	0.3051(3)	0.1634(4)	0.6110(4)	0.0168(5)
	O1	0.2493(3)	0.0090(3)	0.4440(4)	0.0244(6)
	O2	0.3801(3)	0.3306(4)	0.4977(3)	0.0236(5)
	O3	0.4734(3)	0.1081(3)	0.7988(4)	0.0267(6)
	O4	0.1313(4)	0.2154(3)	0.7096(4)	0.0242(6)
800	La/Ca	0.2835(3)	0.1608(3)	0.1003(3)	0.0357(4)
	P	0.3058(5)	0.1634(5)	0.6105(5)	0.0375(3)
	O1	0.2501(4)	0.0105(4)	0.4436(5)	0.0481(8)
	O2	0.3806(4)	0.3307(5)	0.4976(4)	0.0448(5)
	O3	0.4738(5)	0.1071(4)	0.7976(6)	0.0496(8)
	O4	0.1318(5)	0.2158(4)	0.7083(5)	0.0464(8)

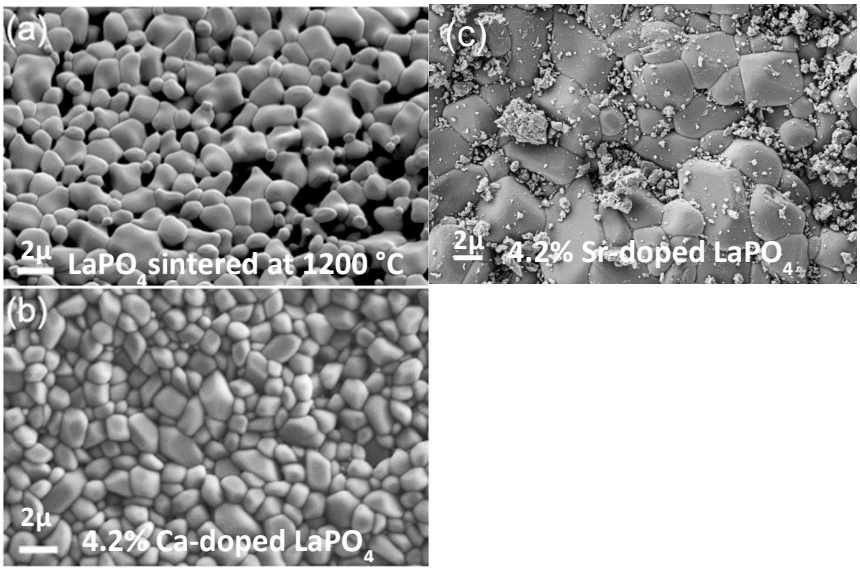


Figure 5.11: The SEM images for (a) $LaPO_4$, (b) 4.2% Ca-doped $LaPO_4$, (c) 4.2% Sr-doped $LaPO_4$.

Table 5.11: $La_{0.958}Sr_{0.042}LaPO_4$ (H_2O): x, y and z are fractional Atomic Coordinates and U is the equivalent isotropic displacement parameters ($Å^2$) at 60°C to 500°C.

T(°C)		x	y	z	U
60	La/Ca	0.2821(1)	0.1593(2)	0.1003(2)	0.01002(3)
	P	0.30460(3)	0.1644(3)	0.6122(3)	0.01002(3)
	O1	0.2496(2)	0.0077(2)	0.4446(3)	0.01392(4)
	O2	0.3804(2)	0.3305(3)	0.4979(2)	0.01346(4)
	O4	0.4734(2)	0.1084(2)	0.8002(3)	0.01456(4)
	O3	0.1307(3)	0.2156(2)	0.7100(3)	0.01375(4)
70	La/Ca	0.2822(2)	0.1594(3)	0.1002(3)	0.01037(5)
	P	0.3052(4)	0.1645(5)	0.6119(4)	0.01132(6)
	O1	0.2495(4)	0.0081(4)	0.4448(4)	0.01484(7)
	O2	0.3799(3)	0.3305(4)	0.4973(4)	0.01418(6)
	O4	0.4729(4)	0.1085(3)	0.7995(5)	0.01467(7)
	O3	0.1305(4)	0.2157(3)	0.7103(4)	0.01406(7)
260	La/Ca	0.2827(2)	0.1597(3)	0.1001(2)	0.0161(4)
	P	0.3051(4)	0.1641(4)	0.6116(4)	0.0154(5)
	O1	0.2495(3)	0.0084(3)	0.4438(4)	0.0226(6)
	O2	0.3800(3)	0.3306(4)	0.4978(3)	0.0214(5)
	O4	0.4730(4)	0.1081(3)	0.7987(4)	0.0235(6)
	O3	0.1321(4)	0.2153(3)	0.7095(4)	0.0222(6)
500	La/Ca	0.2833(2)	0.1600(3)	0.1001(3)	0.0188(5)
	P	0.3055(4)	0.1636(5)	0.6114(4)	0.0188(6)
	O1	0.2498(4)	0.0088(4)	0.4439(4)	0.0263(7)
	O2	0.3798(3)	0.3302(4)	0.4982(4)	0.0253(7)
	O4	0.4726(4)	0.1080(4)	0.7985(5)	0.0285(8)
	O3	0.1326(4)	0.2153(3)	0.7090(5)	0.0271(7)

5.4 Electrochemical Impedance Spectroscopy (EIS)

AC impedance spectroscopy is used to investigate the electrical properties of $La_{0.958}Sr_{0.042}PO_4$ and $La_{0.958}Ca_{0.042}PO_4$ (the samples sintered at 1200°C). The ionic or the protonic conductivity can be determined from the ac conductivity.

Ac conductivity can reveal the microscopic nature of the proton conducting process in the phosphate material Stanguennec and Elliott (1994). When an AC sinusoidal signal is applied to the sample, the impedance can be measured. The impedance can be obtained by dividing vector voltage by vector current from the sinusoidal signal. The impedance of the sample is a complex quantity and it obeys

Table 5.12: Hydrated and Dry $La_{0.958}Ca_{0.042}LaPO_4$ at 300 K: x, y and z are fractional Atomic Coordinates and U is the equivalent isotropic displacement parameters ($Å^2$).

		x	y	z	U
Hydrated	La/Ca	0.0.28179(10)	0.15956(13)	0.10069(12)	0.0041(3)
	P	0.30462(17)	0.1642(2)	0.61235(18)	0.0028(3)
	O1	0.24951(15)	0.00775(16)	0.44548(18)	0.0063(4)
	O2	0.38088(15)	0.33143(19)	0.49708(17)	0.0073(4)
	O4	0.47419(17)	0.10839(15)	0.8015(2)	0.0080(4)
	O3	0.12904(18)	0.21513(14)	0.71016(18)	0.0062(4)
Dry	La/Ca	0.28179(10)	0.15948(13)	0.10073(12)	0.0042(3)
	P	0.30435(17)	0.1643(2)	0.61241(18)	0.0025(3)
	O1	0.24952(16)	0.00788(16)	0.44534(18)	0.0064(4)
	O2	0.38093(15)	0.33154(19)	0.49693(17)	0.0077(4)
	O3	0.47419(17)	0.10829(15)	0.8014(2)	0.0082(4)
	O4	0.12902(18)	0.21536(14)	0.71031(18)	0.0060(4)

Ohms law. The proton conductivity depends on the proton concentration and average mobility. More details of the proton conductivity in general and for Ca-doped $LaPO_4$ in particular will be described in the next chapter. A comparison between the $La_{0.958}Sr_{0.042}PO_4$ and $La_{0.958}Ca_{0.042}PO_4$ conductivity in dry and wet (2.2 mol% water content) air is presented by figure 5.12. The conductivity of Sr is higher than Ca doped sample. Our conductivity results are in the same order to the previous reported studies Norby and Christiansen (1995); Amezawa et al. (2005). The activation energy of the $La_{0.958}Sr_{0.042}PO_4$ from 300°C to 600°C is

$$E_a \pm \Delta E_a = (0.69 \pm 0.02)\text{eV} \tag{5.2}$$

At 800°C the conductivity of 4.2% Sr is 1.6×10^{-4}S/cm while the conductivity of the 4.2% Ca is 1.6×10^{-5}S/cm these result agree with the result that have been obtained by Norby and Christiansen. They reported that the proton conductivity at 800°C in wet air is around 3×10^{-4}S/cm and 6×10^{-5}S/cm for 5% Ca- and 5%Sr-doped $LaPO_4$ Norby and Christiansen (1995).

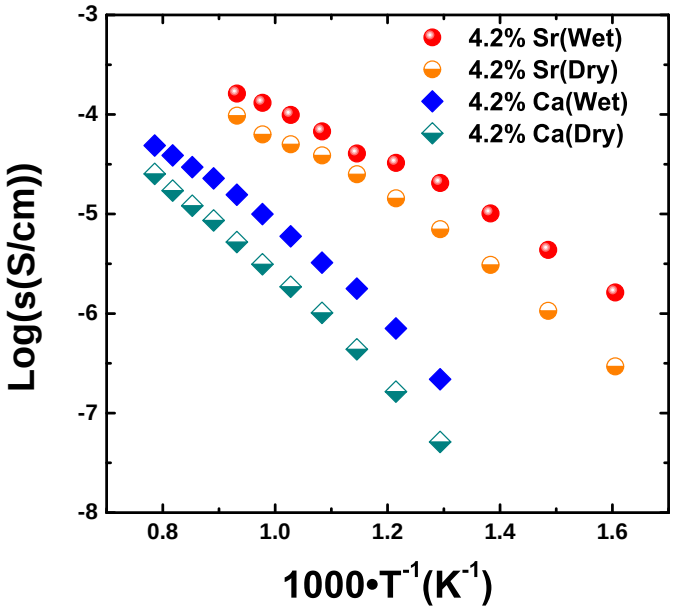


Figure 5.12: Conductivities of the $La_{0.958}Sr_{0.042}PO_4$ and $La_{0.958}Ca_{0.042}PO_4$ in dry and wet (2.2 mol% water content) air.

5.5 Quasi-elastic neutron scattering

For 4.2%Ca-doped $LaPO_4$ sample a more details will be presented in the next chapter which is an article that have been submitted and is being reviewed by Journal Physical Chemistry C. In this section I will present comparing between the proton self-diffusion obtained from the QENS measurement and the conductivity measurement. Haven ratio (H_R) used to correlate between a serial of self-diffusion, D, of atoms jump in the lattice and the ionic diffusion of defects that determined from the conductivity, σ, using the Nernst-Einstein relation Bychkov et al. (2001); Harley and De Jonghe (2010).

$$H_R = \frac{D_\sigma}{D} \tag{5.3}$$

The estimated value of Haven ratio is unity in the case of random walk mechanism. If different correlations happened between the diffusion from the conductivity and the self-diffusion, then Haven ration deviates from unity Scharfenberger et al. (2006). Previous reported studies investigated the H/D isotope effect of the conductivity by

determined by $\sigma_{H_2O}/\sigma_{D_2O}$ (the ratio for proton diffusion process is equal to $\sqrt{2}$) of Sr-, Ca- doped $LaPO_4$ as function of temperature. The studies conclude that the Ca- and Sr-doped $LaPO_4$ conducted protons primarily under humid atmosphere and in particular at low temperature Norby and Christiansen (1995); Amezawa et al. (2005). Thus at 500°C the protons are the dominate charge carrier in the Ca-doped $LaPO_4$. The Haven ratio from the ratio of diffusion (from EIS measurement) and self-diffusion (from QENS measurement) at 500°C is 5.1×10^{-6}.

This ratio is very far away from unity which means that the proton diffusion process from QENS experiment is not correlated with proton diffusion process from EIS experiment. Figure 5.13 present the diffusion of EIS measurement and QENS measurement.

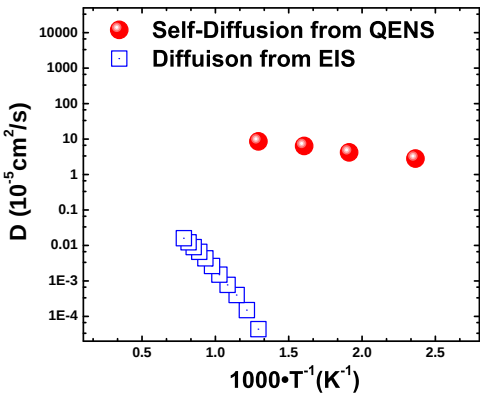


Figure 5.13: The diffusion (in log scale) of EIS measurement (blue symbols) and QENS measurement (red symbols) for 4.2%Ca-doped $LaPO_4$.

Chapter 6

Quasi-Elastic Neutron Scattering Reveals Fast Proton Diffusion in Ca-doped $LaPO_4$

6.1 Introduction

Proton ceramic fuel cells (PCFCs) operating in the intermediate temperature range of 300-500°C offer potentially revolutionary advantages over existing fuel cells because expensive noble metal catalysts would not be needed, and *in situ* reforming of liquid bio-fuels such as ethanol or methanol would be possible Phadke et al. (2012); Haile et al. (2001); Malavasi et al. (2010). The chief obstacle facing intermediate fuel cells is the lack of a suitable electrolyte in the operating temperature range. A good electrolyte is thermally and chemically stable, inexpensive, environmentally friendly, and has a proton conductivity on the order of 10^{-2}S cm^{-1} at 400°C. Rare earth phosphates are an attractive class of materials because they fulfill most of these requirements, and are known to conduct protons in the operating temperature range. If the proton conductivity of phosphates could be raised by 1-2 orders of magnitude, they would become viable materials for applications.

Hydrogen is incorporated into rare earth phosphates by first replacing a fraction of the trivalent rare earth with a divalent ion such as Ca, Sr, or Ba in order to create oxygen defects Norby and Christiansen (1995); Amezawa et al. (2005). When the material is heated in a moist atmosphere, oxygen from the water molecules fills the defects while at the same time introducing two protons into the system**?**. These protons cannot occupy lattice or interstitial sites, but are always embedded in the electron cloud of an oxygen ion, forming hydroxide defects.6 Although it was first thought that protons are transported via hydroxide ions, it is now known that in some materials the protons migrate as lone protons hopping between relatively stationary oxygen ions Cukierman (2006). It is believed that the proton motion involves both localized diffusion and proton transfer. The rate limiting steps of the transport are not well understood, especially considering that quantum fluctuations have recently been shown to have a large effect on the transfer barrier.Kreuer et al. (2004); Vuilleumier et al. (1998); Tuckerman et al. (1997)

First-principles calculations have been reported on the proton diffusion network in $LaPO_4$.Toyoura et al. (2012); Yu and Jonghe (2007) Four possible types of activated proton motion with their related activation energies are discussed: (1) oscillatory motion in which the proton can jump back and forth frequently between the same two oxygen ions on adjacent PO_4 tetrahedra with an activation energy less than 0.1 eV; (2) rotation around a tetrahedron by jumping between local energy minima surrounding a single oxygen ion on the tetrahedron with an activation energy of 0.14-0.15 eV; (3) intra-tetrahedral (where the proton transfers from one oxygen ion to oxygen ion in the same PO_4 tetrahedron) with an activation energy $\sim$ 2 eV; (4) inter-tetrahedral hopping where the proton transfers from one PO_4 tetrahedron to another tetrahedron over a distance of about 3 Å with an activation energy near 0.9 eV. Of these four, it was noted12 that the first two result only in local motion and cannot be responsible for long-range diffusion and conductivity but they could facilitate other transfer modes. The third was deemed to have an energy barrier too high for frequent

proton transfer to occur while the fourth allowed transfer between tetrahedra which is necessary for long-range diffusion and conductivity.12

In this chapter we use incoherent quasi-elastic neutron scattering (QENS) to study the dynamics of proton diffusion in Ca-doped $LaPO_4$. QENS is a powerful technique to probe diffusive motions in the 10^{-12} to 10^{-9} second time range and length scales from ~ 3 to 31 Å. These are the time and length scales of relevance to the diffusion of hydrogen ions and hydrogenous species. QENS measures the dynamic structure factor, $S(\vec{Q},\omega)$, at small energy transfer, ω, and at momentum transfers, $\vec{Q}$, typically less than a few $Å^{-1}$. The neutron scattering signal from a proton is primarily incoherent and the measured $S(\vec{Q},\omega)$ is the Fourier transform in space and time of the self-correlation function. $S(\vec{Q},\omega)$ gives information about the self-diffusive motions.

The very high neutron cross section of protons emphasizes their neutron scattering signal and enables studies of systems with relatively few protons, such as the one considered here. There have been a small number of QENS experiments on proton conducting oxides, and recently a related spin-echo investigation was reported.Karlsson et al. (2010). Most of the previous studies focused on perovskite proton conductors. Karlsson et al. (2009); Braun et al. (2009); Karmonik et al. (1995); Pionke et al. (1997); Matzke et al. (1996); Hempelmann (1996) . while relatively little has been done on materials containing tetrahedral units that are involved in proton transport.Jalarvo et al. (2013a,b). To guarantee a strong neutron scattering signal of QENS measurements we chose the highest possible dopant concentration in order to achieve the highest possible proton uptake. According to Amezawa, et al. the solubility limit of Ca in the $LaPO_4$ lattice was found to be 4.2 mol%, higher than Ba or Sr.5 In this study, we present a detailed investigation of proton conduction in the 4.2% Ca-doped $LaPO_4$ using EIS and QENS. The QENS data reveal fast proton diffusion at intermediate temperatures. This work presents the first QENS investigation of proton dynamics in a rare earth phosphate.

6.2 Experimental

4.2% Ca-doped $LaPO_4$ powders were synthesized by conventional solid-state reaction. The starting materials were calcium phosphate dibasic dihydrate (Fisher Scientific) and lanthanum (III) phosphate hydrate (Strem Chemicals Inc.). The $LaPO_4 \bullet nH_2O$ powder was first dried at 1000°C for 48 h. Mixed stoichiometric amounts of $CaHPO_4 \bullet_2 H_2O$ and $LaPO_4$ powder were calcined at 1000°C for 5 h. The material was finely crushed using an agate mortar, followed by dry ball milling for 45 minutes; this process was repeated 4 times to ensure homogeneous mixing. After pelletizing a 12 mm diameter pellet under a load of 7 metric tons, the samples were sintered at 1200°C in air for 5 h. Pellets were obtained with a relative density of 94% of the X-ray density.

The samples were studied by powder X-ray diffraction (XRD) for phase identification and structure refinement. The XRD patterns of the samples were recorded on a Bruker AXS D2 Phaser diffractometer with Cu Kα radiation ($\lambda = 1.541$ Å). The operating voltage and current were maintained at 30 kV and 10 mA, respectively. Selected higher-quality scans were made with a step size of 0.02° with 12 h scan and a counting rate of 11 s/step.

Scanning Electron Microscopy (SEM) was performed on the samples with Zeiss ULTRA-55 FEG SEM in SE2 detection mode at voltage 10 kV and 5 kV for higher resolution. Sintered pellets similar to those used in EIS measurements prior to electrode fabrication were examined.

Thermogravimetric analysis (TGA) was performed using Netzsch STA 409 PC Luxx, for hydrated sample contained in an alumina crucible. The sample was subject to the following procedure: (1) dehydration by treating the powder in a high-purity dry Ar (99.99%) inside the TGA instrument from room temperature to 1266°C, with a heating rate of 5°C/min and a flow rate of 50 ml/min, followed by an isothermal dwell at 1266°C for 4 h under dry Ar atmosphere; (2) hydration using an isothermal

dwell at 1266°C for 1 h under humid Ar atmosphere, followed by slowly cooling the powder in a humid Ar atmosphere to room temperature at a rate of 2 K/min.

For the electrochemical impedance spectroscopy (EIS) measurements, the sintered pellets were polished to a thickness of 1 mm using SiC paper. The pellets were washed with acetone and then dried at 200°C using a hot plate. The resulting surface was smooth and even. Electrodes were prepared by applying 7 mm diameter circle of Pt paint to each side of the 12 mm diameter pellet and firing at 900°C for 0.5 h in air. The cell was connected by pressing a Pt mesh with Pt wire lead on the surfaces of the two symmetrical porous Pt electrodes. The cell was heated in dry air up to 1000°C for 12 h inside a quartz reactor which was supported in a tube furnace. The dry air was obtained by passing the air gas through the silica-gel dryer with a flow rate of 50 ml/min. Impedance spectra were recorded for one hour at each temperature from 1000°C to 500°C in dry air with cooling rate 5°C/min. The dry air was then switched to hydrated air, with 2.2 mol% water, with a flow rate of 50 ml/min. The cell was heated to 1000°C with heating rate of 5°C/min and held for another 15 h to hydrate the samples. Impedance spectra were recorded in humid air from 1000°C to 500°C with cooling rate of 5°C/min in the frequency range 10^{-2}-10^{6} Hz with signal amplitude of 100 mV using VersaSTAT 4 (Princeton Applied Research) with an internal frequency response analyzer.Bi et al. (2011).

Prior to the QENS experiment, the sample was charged with protons by post-annealing in oxygen atmosphere with a water vapor pressure of 2.2 kPa from a bubbler at 19°C; the sample was then held in a dry oxygen atmosphere at 200°C for several hours to remove any surface water. The sample was kept in sealed container in a vacuum desiccator to avoid any contact with ambient air until the time to conduct the experiment. The sample was mounted in a platinum cylindrical sample holder of annular geometry shortly prior to the QENS experiment. The QENS experiments were performed using the backscattering spectrometer (BASIS) at the Spallation Neutron Source (SNS), Oak Ridge National Laboratory. Mamontov and Herwig (2011). The energy resolution at the elastic line (full width at half-maximum) was

3.4 μeV. In order to minimize multiple scattering the mass and thickness of the sample were limited to $\sim$ 10 g and about 0.24 cm to ensure approximately 90% neutron transmission. The initially hydrated sample, $La_{0.99}Ca_{0.042}PO_{3.979} \bullet 0.021H_2O$, was heated inside the QENS sample cell at 150°C under dry gas for several hours to guarantee there was no surface water on the sample. To maintain sample hydration level during QENS measurements, a wet gas flow system was used. The wet (or subsequently dry) He gas entered the inner quartz tube through the inlet and was delivered to the sample inside the Pt sample holder. The energy spectra were collected at different scattering angles and combined into nine groups resulting in averaged Q values from 0.3 Å^{-1} to 1.9 Å^{-1}. Spectra were taken at 4 temperatures between 150°C and 500°C. The sample was then fully dehydrated by dwelling for 10 hours at 950°C under dry He flowing gas conditions. Spectra were again recorded at the same 4 temperatures in a dry He atmosphere. For background measurement, an empty platinum can inside the flow gas system was measured at 30°C and 500°C under wet and dry He conditions. The data was reduced with BASIS in-house routines. Measured data were normalized to an annular vanadium standard. The DAVE software package and an in-house routine were used to analyze the data. Azuah et al. (2009).

6.3 Results and Discussion

Monoclinic monazite $LaPO_4$ crystallizes in space group $P2_1/n$ (No.14) with a melting point of 2072°C. Hikichi and Nomura (1987); Schatzmann et al. (2009). The crystal structure is composed of isolated PO_4 tetrahedra (Figure 6.1) and La^{3+} coordination polyhedra. The X-ray diffraction (XRD) data in Figure 6.2 demonstrate the phase purity of the QENS sample (hydrated Ca-doped $LaPO_4$). The lack of observed impurity phases in the XRD data suggests that calcium has been successfully doped into the lattice. The pattern was indexed according to the monoclinic structure of the parent compound $LaPO_4$ (PDF 00-032-0493) and the lattice parameters were derived

from a Rietveld refinement of the data using FullProf software. Carvajal (1993). The refined unit cell parameters were $a = 6.8391(2), b = 7.0751(2), c = 6.5097(1)$Å

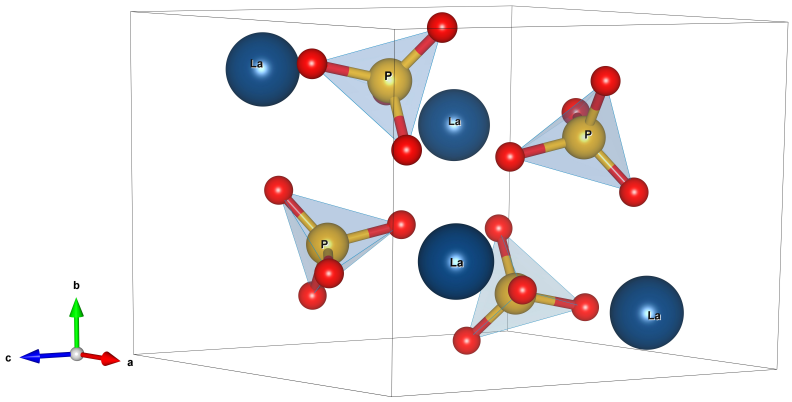


Figure 6.1: The unit cell of $LaPO_4$, which has a monoclinic $P2_1/n$ structure. The unit cell contains La^{3+} cations (blue) and isolated PO_4 tetrahedra (O in red and P in yellow).

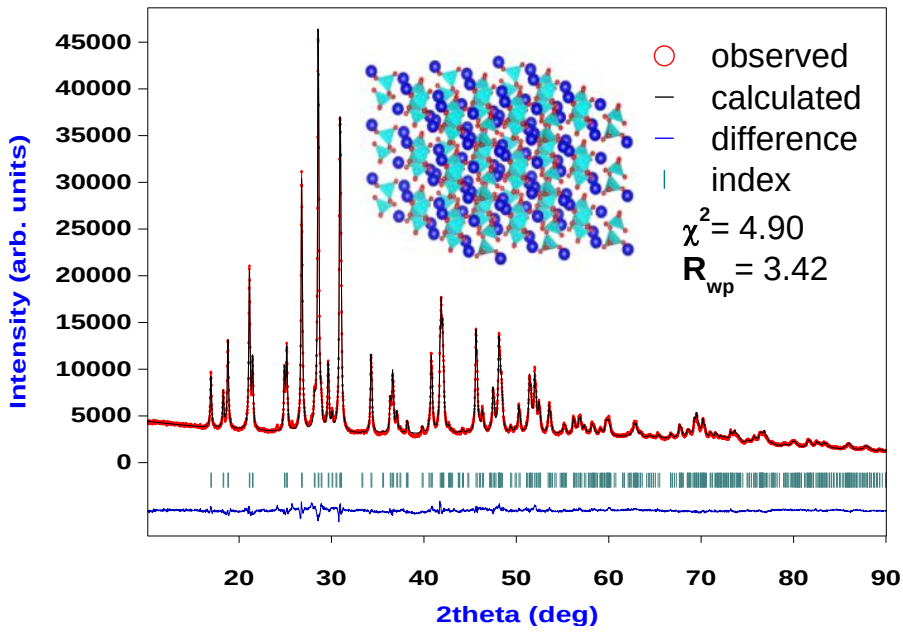


Figure 6.2: Rietveld refinement results obtained from the X-ray powder diffraction data for hydrated $La_{0.958}Ca_{0.042}PO_4$ at room temperature. The XRD pattern was recorded on a Bruker AXS D2 Phaser diffractometer.

and $\beta = 103.29(1)°$. The cell density and volume are 4.98 g/cm^3 and 306.6 Å^3, respectively. The lattice parameters are similar to those of $LaPO_4$, as expected from the similar ionic radii of the La^{3+} and Ca^{2+} cations. The SEM images of 4.2% Ca-doped $LaPO_4$ (Figure 6.3) indicates a broad range of grain sizes, ranging from 1 to 2.5 μm. The grain sizes of $LaPO_4$ range from 1 to 2 μm. Although smooth, the shape of the grains exhibits a variety of angles and length-to-width ratios. In addition, in a higher resolution image, gaps in the $LaPO_4$ sample are up to few hundreds of nanometers. Finally, the overall 4.2% Ca-doped $LaPO_4$ grain sizes and morphology of the sample appeared to be more homogeneous, with a decrease in the number of smaller grains.

According to the model of Amezawa et al., oxygen vacancies resulting from doping of Ca in the monazite-type lanthanum orthophosphate, $LaPO_4$, may lead to the formation of pyrophosphate-type defects $(P_2O_7)^{\bullet\bullet}_{2PO4}$.Amezawa et al. (2001).

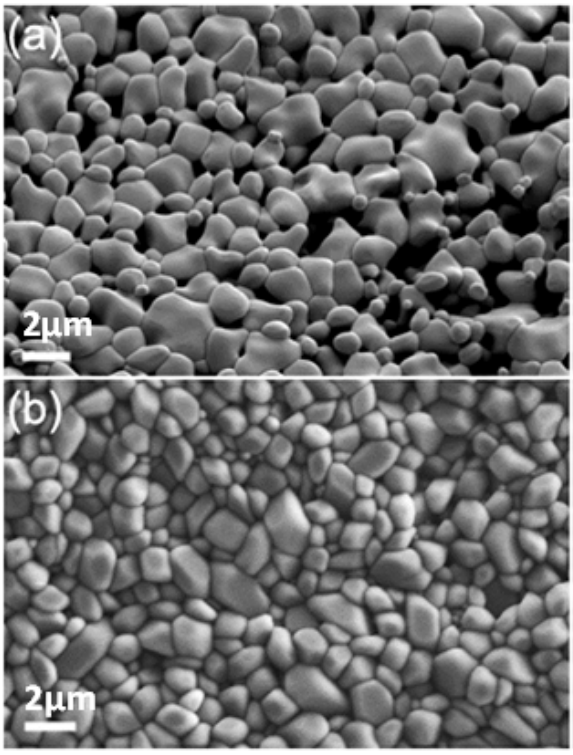


Figure 6.3: Morphology of the $LaPO_4$ sample (a) and 4.2% Ca-doped $LaPO_4$ (b) sintered at 1200°C. The bar scale in both SEM images represents 2 μm.

The signature of P_2O_7 was noticed in Sr-doped $LaPO_4$ by Fourier transform Raman and magic-angle spinning nuclear magnetic resonance spectroscopy experiments.28 When hydrating the pyrophosphate by post-annealing under water vapor, protons dissolve into phosphates forming hydrogen phosphate $(HPO_4)^{\bullet}_{PO4}$. The result is that protons stay at PO_4 tetrahedra in the sample. Toyoura, et al. provided a theoretical study of the proton conduction mechanism in $LaPO_4$ by a first principles approach that supports proton preferential binding to sites around PO_4 tetrahedra.11 They determined the energetically favorable proton sites around PO_4 tetrahedra in the crystal.11 Yu and De Jonghe also investigated the proton-transfer mechanism in $LaPO_4$ on the basis of the density functional calculations.12 Since the low symmetry of $LaPO_4$ allows many computed possible transfer paths, they considered the following classical proton-transfer paths: rotation around an oxygen ion, oscillatory motion between adjacent tetrahedra, transfer between oxygen ions within a single PO_4 tetrahedron (intra-tetrahedral), and jumps between tetrahedra (inter-tetrahedral). The study concluded that the intra-tetrahedral process is forbidden and the inter-tetrahedral transfer with 0.6-1.0 eV potential barriers is the dominant proton-transfer process.12 The energy barrier for forward or backward proton transfer mechanism between two adjacent PO_4 is below 0.1 eV. The interactions between an aliovalent cation dopant, Sr/Ca, and protons in $LaPO_4$ were neglected through the study. More recent theoretical studies have considered the effect of the dopant. The effect of aliovalent dopants in the studies caused a wider range of activation energy barriers for proton transfer. Hatada et al. (2011); Adelstein et al. (2012). In principle the proton concentration $[(HPO_4)^{\bullet}_{PO4}]$ of the material depends on the dopant $[Ca'_{La}]$, and on the concentration of oxygen defects $[(P_2O_7)^{\bullet\bullet}_{2PO4}]$ and is described by:

$$[(HPO_4)^{\bullet}_{PO4}] + 2[(P_2O_7)^{\bullet\bullet}_{2PO4}] = [Ca'_{La}] \tag{6.1}$$

The proton content inside the sample also depends in the partial pressure of water $p(H_2O)$. If the oxygen vacancies are dominant defects, the proton concentration

should be proportional to $p(H_2O)^{1/2}$.5 The TGA dehydration and hydration curves of the Ca-doped $LaPO_4$ are shown in Figure 6.4. To determine proton content, we analyzed the TGA data by assuming that the dehydration/hydration is the main factor responsible for the weight loss or gain in the TGA experiment. The sample was hydrated by post annealing before the TGA experiment. The hydrogen content can be determined from the observed weight gain. The hydration ratio number (molar fraction of H) is $n = 0.042$, which suggests full hydration of the sample. QENS data can be used to quantify the proton content of a sample. From the quasi-elastic scattering intensity, hydrogen cross section and using a known vanadium reference, proton defect concentrations of $4.6 \pm 0.1, 4.9 \pm 0.1, 4.74 \pm 0.1$, and 4.3 ± 0.1 mol% at 150, 250, 350 and 500°C are deduced. These results are in a good agreement with the value of 4.2 mol% from the chemical sample preparation and from the TGA measurements.

Conductivity measurements were undertaken using impedance spectroscopy on both wet and dry samples, and were subsequently analyzed for bulk and grain boundary contributions as a function of temperature. Representative Nyquist plots

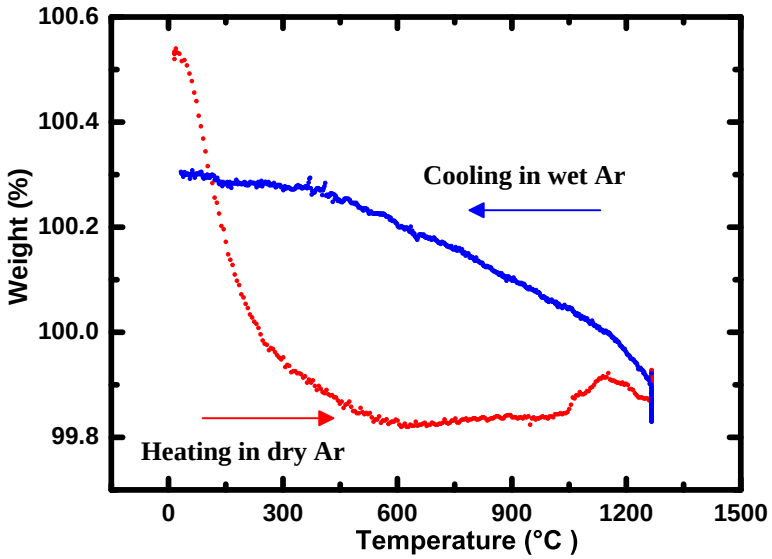


Figure 6.4: TGA data for $La_{0.958}Ca_{0.042}PO_4$ under dry and wet Ar atmospheres. The large hysteresis indicates the clear absorption of H_2O under wet atmosphere.

for the dry ($La_{0.958}Ca_{0.042}PO_{3.979}$) and the hydrated ($La_{0.958}Ca_{0.042}PO_{3.979}\bullet 0.021H_2O$) samples in dry and wet atmospheres, respectively, are shown in Figure 6.5 for data collected at 550°C. Semicircles were observed corresponding to contributions from the bulk, grain boundary, and electrodes. The impedance spectra were fitted with a (R_1Q_1) (R_2Q_2) (R_3Q_3) equivalent electrical circuit. The bulk (R_{bulk}), the grain boundary (R_{gb}) and electrode (R_{e}) resistances are determined in dry air at the geometrical capacitances 8.4×10^{11}, 3.3×10^{9}, and 1.2×10^{-5} F cm^2, respectively. The protons connected to oxygen ions around the PO_4 tetrahedra experience long-range diffusion under the influence of an electrochemical gradient in the system. The long-range diffusion leads to proton conductivity which is temperature dependent. The conductivities, σ(S cm^{-1}), are expressed as:

$$\sigma(T) = qc\mu(T) \tag{6.2}$$

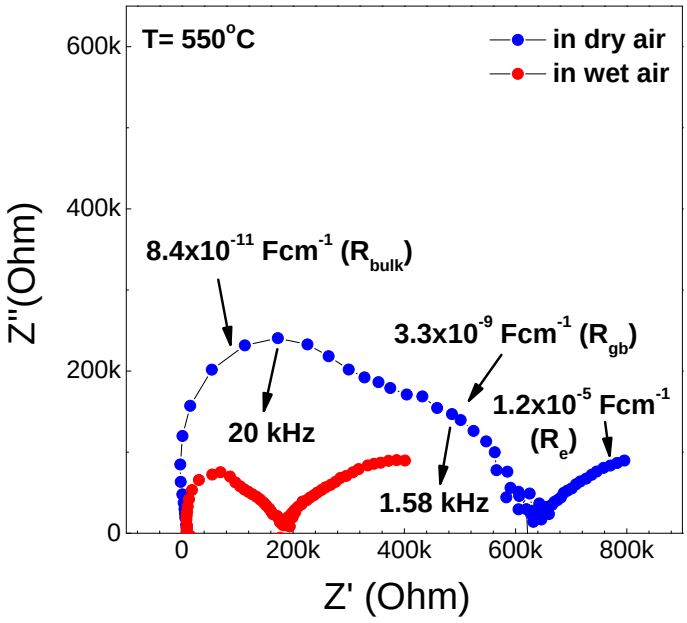


Figure 6.5: AC impedance spectra for 4.2% Ca-doped $LaPO_4$ in wet and dry air at 550°C.

or

$$\sigma(T) = \frac{q^2 c D(T)}{k_B T} \tag{6.3}$$

Here $q, k_B, c, \mu(T), D(T)$ and T are the charge per ion (1.6×10^{-19}C), Boltzmann constant, charge concentration (cm^{-3}), mobility ($\mathrm{cm}^2\mathrm{V}^{-1}\mathrm{s}^{-1}$), diffusion coefficient ($\mathrm{cm}^2\mathrm{s}^{-1}$), and the absolute temperature (K), respectively. The proton charge concentration of the hydrated 4.2% Ca-doped $LaPO_4$ can be estimated to be $5.5 \times 10^{20}\mathrm{cm}^{-3}$ on the basis of 4.2% La substituted by Ca. The AC conductivity in dry and wet air, derived from EIS data, is plotted vs. $(1000/T)$ in Figure 6.6; these data satisfy the Arrhenius relationship (Equation 6.4) over the temperature range 500 to 1000°C:

$$\sigma T = A \exp\left(-\frac{E_a}{k_B T}\right) \tag{6.4}$$

where A is a pre-exponential constant and E_a is the activation energy. In wet air, the conductivity is approximately 1×10^{-4} S/cm at 950°C. Conductivity under dry and wet air, from 500 to 850°C, can be expressed by equations 6.5 and 6.6:

$$\sigma_{\mathrm{Dry}} = \frac{A_{\mathrm{Dry}}}{T} \exp\left(-\frac{1.16 \pm 0.03 \text{ eV}}{k_B T}\right) \tag{6.5}$$

$$\sigma_{\mathrm{Wet}} = \frac{A_{\mathrm{Dry}}}{T} \exp\left(-\frac{1.05 \pm 0.03 \text{ eV}}{k_B T}\right) \tag{6.6}$$

The highest conductivity (under a water vapor pressure of 2.2 kPa) measured for the 4.2% Ca-doped $LaPO_4$ sample was $1.3 \times 10^{-4}\mathrm{S\ cm}^{-1}$ at 1000°C. The difference observed between the conductivities in wet and dry air indicates significant protonic conduction. The measured conductivity was slightly lower but of the same magnitude as previously reported.4,5 Using Equation 6.3, the estimated diffusion coefficients are on the order of $10^{-10}, 10^{-8}$, and $10^{-7}\mathrm{cm}^2\mathrm{s}^{-1}$ at 500, 700, and 1000°C, respectively.

QENS data were collected at 150°C, 250°C, 350°C, and 500°C to obtain further information on proton conduction and to examine models for the mechanism of proton diffusion in the lower temperature regime where the dynamics were found within the

time window accessible by BASIS. The measured $S(\vec{Q},\omega)$ could be separated into elastic (δ-function), quasi-elastic (Lorentzian) and background contributions as shown in Figure 6.7 and expressed as:

$$S(Q,\omega)_{\text{meas}} = [A(Q)\delta(\omega) + B(Q)L(Q,\omega)] \otimes R(Q,\omega) + C(Q) + \omega D(Q) \qquad (6.7)$$

As seen in Figure 6.8, the Lorentzian component of the hydrated sample broadens with increasing temperature and increasing Q, while the signal from the dehydrated sample is essentially elastic, exhibiting no broadening beyond the instrumental resolution. The dehydrated sample exhibited little or no temperature dependence beyond a slight reduction in intensity due to increased Debye-Waller vibrational motion.

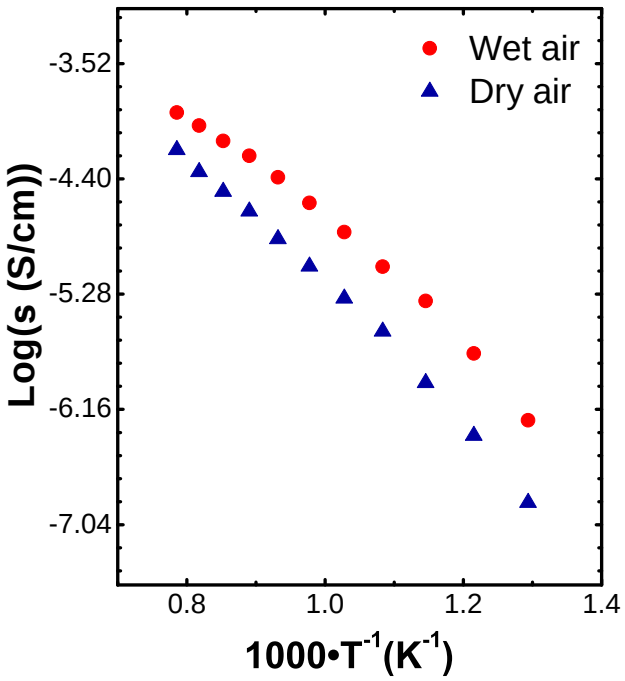


Figure 6.6: Conductivities of the $La_{0.958}Ca_{0.042}PO_4$ in dry and wet (2.2 mol% water content) air.

The signal from diffusing protons alone was obtained by subtracting the dehydrated sample signal from that of the hydrated sample at each temperature as shown in Figure 6.9 for 150°C and 350°C. As hydrogen has a much larger scattering cross-section than any possibly diffusing oxygen ions, the signal is dominated by that from single-proton diffusion. Bée and Mol (2003); Hempelmann (2000) The subtraction resulted in a noisy and sometimes over-subtracted region near the elastic, $\omega = 0$, position. Consequently, data between ± 20 μeV were excluded in the model fitting described below. Figure 6.9 shows a Lorentzian fit to the differenced data at selected Q-values 0.3, 0.5, and 0.9 Å^{-1} at 150 and 350°C. At temperatures above 500°C, the proton motions become so fast that the associated Lorentzian broadens beyond the dynamic range of BASIS and appears as a flat background, even at low-Q where the Lorentzians are narrower. The QENS measurements were unable to track the proton dynamics above this temperature at the measured time scale. As seen in Fig. 6.9, a single Lorentzian line shape was sufficient to describe the data. Figure 10 shows the

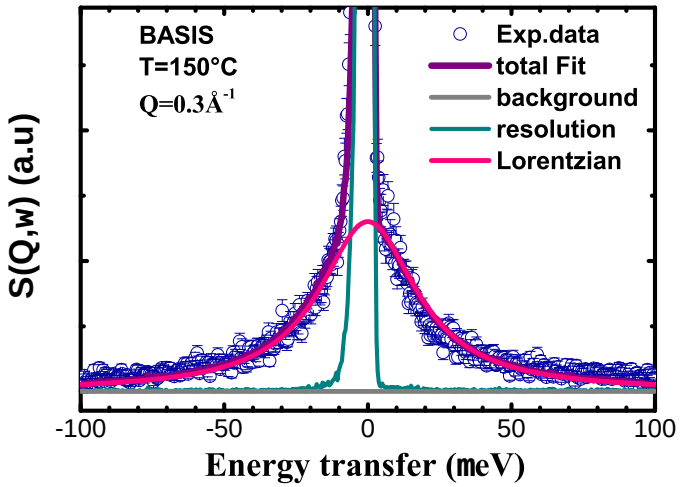


Figure 6.7: Quasi-elastic spectra collected from the hydrated sample at a momentum transfer of 0.3 Å^{-1} and $T = 150$°C. Symbols are the experimental data and the purple solid line is the total fit. The gray, aqua, and the pink solid lines are the background, delta, and Lorentzian components convoluted with energy resolution function of the instrument, respectively as described in Equation 6.7 in the text.

Lorentzian HWHM, $\Gamma(\vec{Q})$, as a function of Q^2 at each measured temperature. The fall-off from DQ^2 behavior at higher Q is an indication of a jump diffusion process.

To better understand the mechanism of proton diffusion, we modeled the scattering data using the isotropic Chudley-Elliott (CE) jump-diffusion model. Chudley and Elliott (1961). This model assumes that diffusive motion occurs via discrete jumps, where the particle resides for a time interval τ at a given site and then jumps in a relatively short (essentially instantaneous) time to a new location a distance ℓ away. In this model, $S(\vec{Q},\omega)$ is simply a Lorentzian whose width varies in

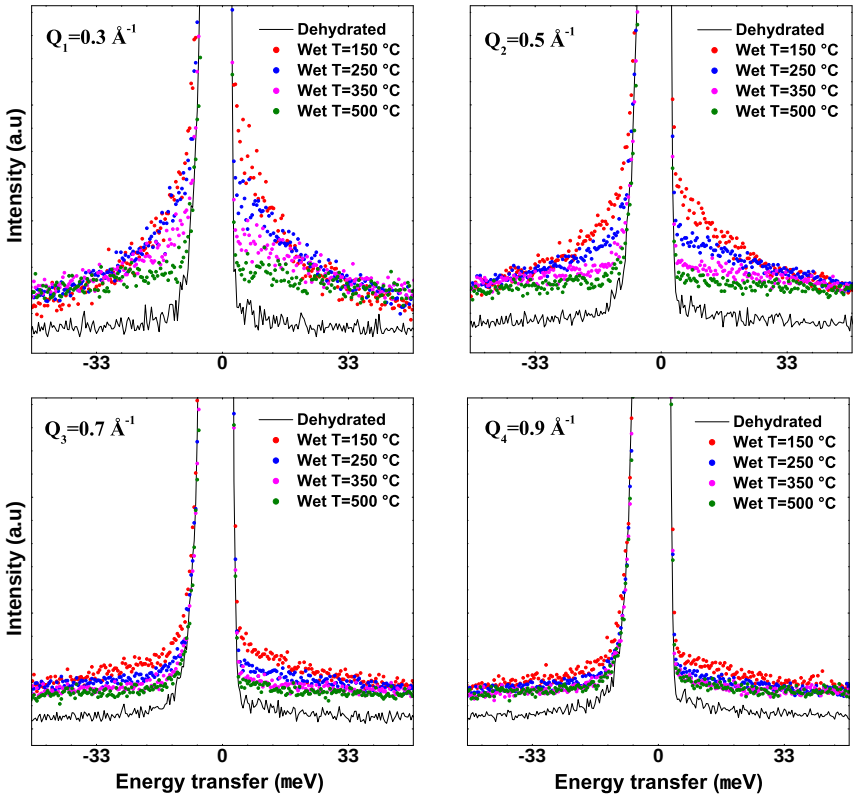


Figure 6.8: Scattering intensities (linear scale) collected on BASIS for 4.2% Ca-doped $LaPO_4$ for hydrated (color symbols) for $Q = 0.3, 0.5, 0.7$, and 0.9 Å^{-1} and for $T = 150, 250, 350$, and 500°C. For reference, the signal from the dehydrated sample is shown at $T = 150$°C.

Q as

$$\Gamma(\vec{Q}) = \frac{\hbar}{\tau}\left(1 - \frac{\sin(Q\ell)}{(Q\ell)}\right) \tag{6.8}$$

and the diffusion coefficient, $D = \ell^2/6\tau$. Figure 6.10 shows fits of the CE model to the Lorentzian half-widths and Table 6.1 summarizes the results. This model with a single jump distance is well-able to describe the Q-dependence of the Lorentzian

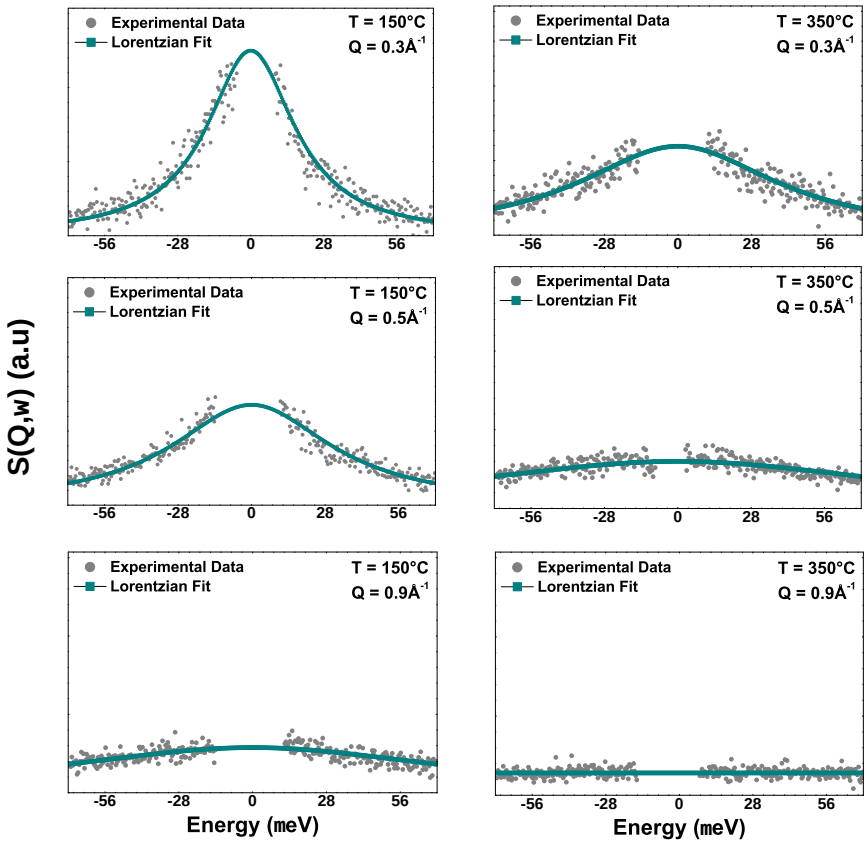


Figure 6.9: The difference spectra between the "wet" and "dry" sample conditions. Symbols are data at the indicated Q-values and temperatures of 150°C (left panels) and 350°C (right panels). Solid lines are Lorentzian fits to the data. The data near the elastic ($\omega = 0$) region were suppressed and not fit due to the imperfect subtraction of the very large elastic signal from the immobile atoms in the crystal structure.

Table 6.1: The fit model parameters result from the first approach. The mean residence time τ(ps), mean jump distance ℓ(Å), self-diffusion coefficient $D(10^{-5}\text{cm}^2/\text{s})$ and the activation energy E_a (eV), are listed respectively. The Q^2-dependence of the half-width-at-half-maximum (HWHM) of the Lorentzians was obtained by fitting with the isotropic Chudley-Elliott model for $T = 150, 250, 350$, and 500°C.)

T(°C)	150	250	350	500
τ(ps)	5.45 ± 0.42	4.48 ± 0.3	3.75 ± 0.14	3.78 ± 0.18
ℓ (Å)	3.02 ± 0.15	3.45 ± 0.15	3.88 ± 0.15	4.96 ± 0.28
$D(10^{-5}\text{cm}^2/\text{s})$	2.79 ± 0.35	4.43 ± 0.48	6.69 ± 0.57	10.85 ± 1.30
$E_a \pm \Delta E_a = 0.11 \pm 0.01$ eV				

Table 6.2: The fit model parameters result from the second approach, the mean residence time τ(ps), mean jump distance ℓ (Å), the mean-square displacement $\langle u^2 \rangle^{1/2}$ (Å), self-diffusion coefficient $D(10^{-5}\text{cm}^2/\text{s})$ and the activation energy E_a(eV), are listed respectively. The isotropic Chudley-Elliott model directly fit to the measured $S(\vec{Q}, \omega)$. This method fit all the Q-spectra at a given temperature simultaneously, including their intensity as normalized to the vanadium standard.

T(°C)	150	250	350	500
τ(ps)	5.5 ± 0.2	4.7 ± 0.1	4.1 ± 0.1	3.6 ± 0.1
ℓ (Å)	3.05 ± 0.06	3.45 ± 0.06	3.99 ± 0.06	4.30 ± 0.05
$\langle u^2 \rangle^{1/2}$ (Å)	0.52 ± 0.03	0.71 ± 0.02	0.76 ± 0.02	0.65 ± 0.01
$D(10^{-5}\text{cm}^2/\text{s})$	2.8 ± 0.58	4.2 ± 0.45	6.3 ± 0.67	8.6 ± 0.88
$E_a \pm \Delta E_a = 0.09 \pm 0.01$ eV				

half-widths. A second modeling approach fit the CE model directly to the measured $S(\vec{Q},\omega)$. This method fit all the Q-spectra at a given temperature simultaneously, including their intensity as normalized to the vanadium standard. In this case, the vibrational motion of the proton between jumps was modeled as a Debye-Waller factor, $\exp(-Q^2\langle u^2\rangle/3)$, that multiplied the Lorentzian of the CE model accounting for the decrease in area with increasing Q. The model parameters determined from this approach and listed in Table 6.2 are in reasonable agreement with those determined from the first approach. Figures 6.11, Chudley-Elliott diffusion model parameters derived from single Lorentzian fits to the data, and 12, Chudley-Elliott diffusion model parameters derived from direct fits to $S(\vec{Q},\omega)$, present the fitting results from both methods as a function of temperature. The mean jump distance increases from about 3 to 4.96 Å over the temperature range of the measurements. This increase far exceeds what might be expected from thermal expansion of the

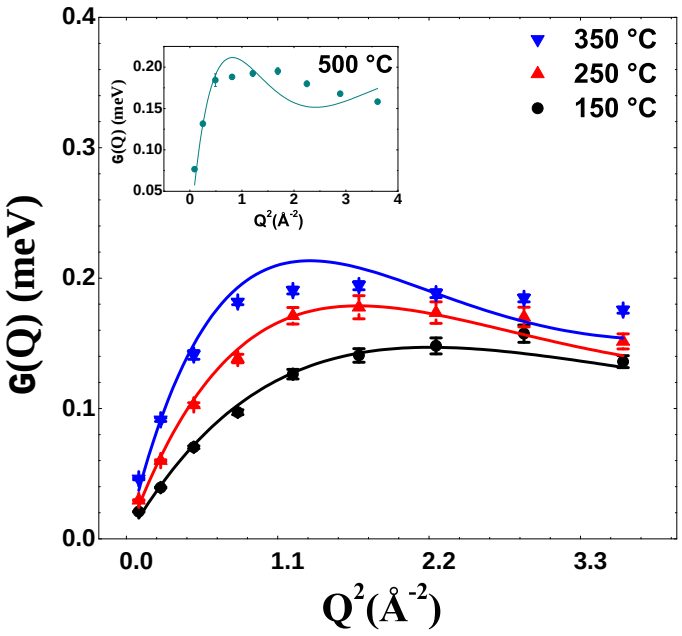


Figure 6.10: Q^2-dependence of the half-width-at-half-maximum (HWHM), symbols, of the Lorentzians obtained by fitting our QENS spectra with the isotropic Chudley-Elliott model, solid lines, for $T = 150, 250, 350$, and 500°C.

lattice (¡0.4%) and so likely indicates an admixture of more than a single diffusional process at the higher temperatures that includes larger length scales. al-Wahish et al. (2014b). Figures 6.11 and 6.12 also show the Arrhenius behavior of the

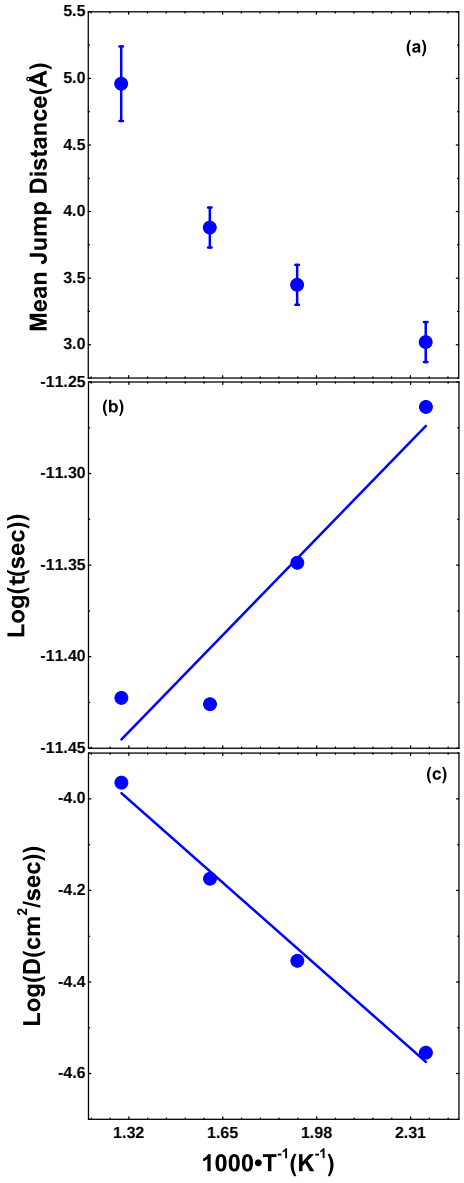


Figure 6.11: Chudley-Elliott diffusion model parameters derived from single-Lorentzian fits to the data: (a) mean jump distance, (b) and (c) are Arrhenius plots of the mean residence time and self-diffusion coefficient, respectively.

diffusion coefficient and the mean residence time. The activation energies of the diffusion coefficient are $E_a = 0.11 \pm 0.01$ eV and $E_a = 0.09 \pm 0.01$ eV from the first and second fitting approaches, respectively. These values are about an order of magnitude lower than determined from the conductivity measurements above and reported elsewhere.4,5 This implies that the diffusive process determined from QENS is not responsible for the proton conductivity seen at higher temperatures. QENS experiments of octahedral perovskite systems have revealed an unusual proton dynamics with low activation energy (0.09 eV)14, much lower than the long-range diffusion activation energy that has been detected by EIS. 14, 15 In fact, if the jump diffusion process measured by QENS had a truly long-range diffusion coefficient of the magnitude reported in Tables 6.1 and 6.2, this material would have exhibited much higher conductivity at lower temperatures. It is important to note that the lowest-Q value at which we had a useful QENS signal was 0.3 Å^{-1} and that this

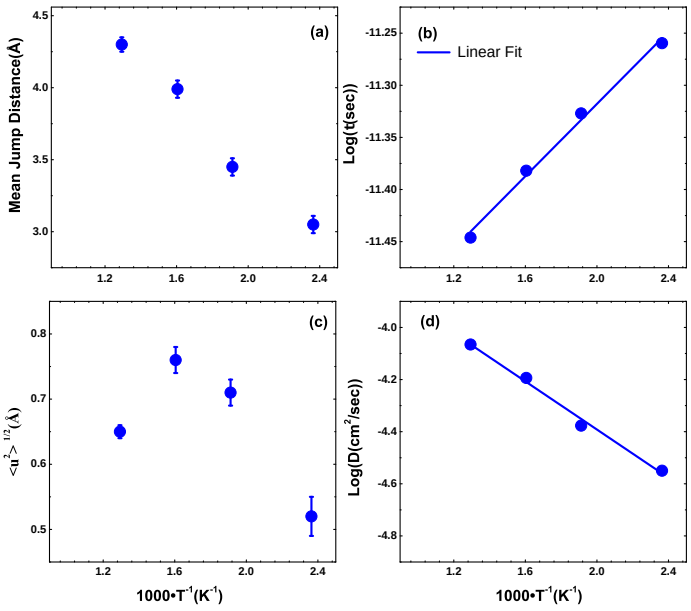


Figure 6.12: Chudley-Elliott diffusion model parameters derived from direct fits to $S(\vec{Q}, \omega)$: (a) mean jump distance, (b) and (d) are Arrhenius plots of the mean residence time and self-diffusion coefficient, respectively, and (c) the mean-square displacement $\langle u^2 \rangle^{1/2}$ (Å) of the Debye-Waller factor.

corresponds to a length scale of about 20 Å. It is likely that processes occurring on length scales greater than this restrict the ability of the proton to exhibit truly long-range diffusion. In fact, there are a number of local (spatially restricted) pathways that can be identified in Toyoura et al.11 that allow the proton to diffuse over a limited distance with a maximum energy barrier of about 0.09 eV, comparable to the activation energy identified from the QENS measurements. Several such pathways are illustrated in Figure 6.13. These pathways will not lead to long-range diffusion and associated conductivity at low temperature due to the high energy barrier that must be crossed on either end for motion to continue. Nevertheless, these pathways may become important as part of a long-range diffusive process and associated conductivity at higher temperatures.

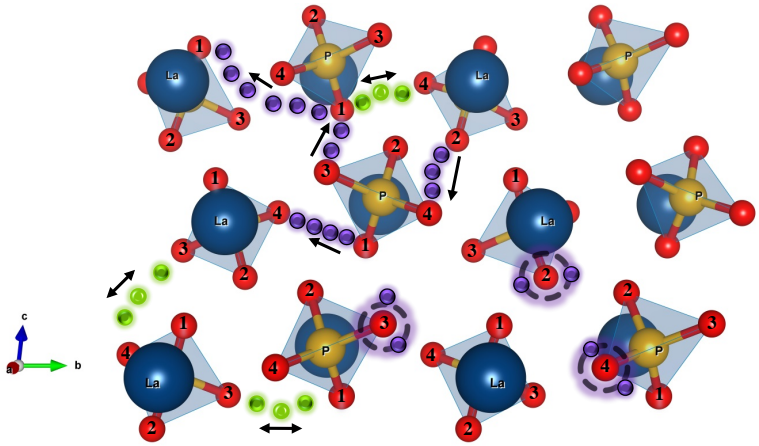


Figure 6.13: Oscillatory proton transfer O1 $\longleftrightarrow$ O4, O3 $\longleftrightarrow$ O1, and O4 $\longleftrightarrow$ O3 with low potential barriers $\leq$ 0.09 eV, and jump length $\ell = 0.6, 0.46$, and 0.41 Å respectively. Rotational migration paths are around O2, O3, and O4 with activation energy 0.05 eV $\leq E_a <$ 1 eV. Inter-tetrahedral hopping paths such as: O3$\rightarrow$O1 with $\ell \approx$ 2.35 Å and 0.2 eV, O1$\rightarrow$O1 with $\ell \approx$ 1.96 Å, and 0.16 eV, O1$\rightarrow$O4 with $\ell \approx$ 2.78 Å and 0.26 eV. O2$\rightarrow$O4 with $\ell \approx 1.89Z$Å and 0.13 eV. The mean jump lengths determined from X-ray Retrieved refinement. The mean jump lengths are correlated to the activation energies from Ref.11. Illustrated by using visualization for electronic and structural analysis software (vesta).

6.4 Conclusion

In summary the proton dynamics in $La_{0.99}Ca_{0.042}PO_{3.979} \bullet 0.021H_2O$ have been investigated using electrochemical impedance spectroscopy (EIS) and quasi-elastic-neutron scattering (QENS). The Q-dependent broadening of the QENS signal is consistent with that predicted by the isotropic Chudley-Elliott model describing jump diffusion. The activation energies inferred from the QENS and EIS measurements were 0.09 eV and 1 eV, respectively. These activation energies were obtained over different temperature ranges, and it is likely that QENS and EIS are probing fundamentally different diffusion processes. If we compare our results to two recent theoretical studies,Toyoura et al. (2012); Yu and Jonghe (2007), it is likely that the EIS data reflect long-range inter-tetrahedral diffusion, whereas QENS probes more local diffusive motions that include oscillatory jumping between adjacent tetrahedra. The magnitude of the self-diffusion coefficients inferred from QENS are considerably higher (10^{-5} to 10^{-4}cm^2/sec, in the temperature window between 150-500°C) than that determined from EIS under wet air, (10^{-10} to 10^{-7}cm^2/sec in the temperature window between 500-1000°C). It is likely that processes occurring on length scales greater than about 20 Å are limiting the long-range diffusion of the proton at the lower temperatures. The activation energy of the diffusive motions identified by QENS is consistent with energy barriers to local pathways of limited length that can be identified from theoretical predictions.

Chapter 7

Instrument design

Most sample environments used in QENS studies allow for temperature investigations below 500 K, a limiting the use of QENS as a probe to study high temperature proton conductors. This limitation arises from two factors: 1.) the type of material used for the sample holder and container. 2.) the escape of protons from inside the samples at elevated temperatures. In previously reported QENS studies, the samples were charged with protons prior to the QENS experiment. To maintain the sample's protoinc stage during the QENS experiment, the samples were tightly sealed inside a can. Most of the time, the can was aluminum Ishikawa et al. (2008); Jalarvo et al. (2013b,a) and sometimes the aluminum can was coated with platinum to prevent corrosion Karlsson et al. (2009). The current article proposes a new sample environment built and used at BASIS SNS ORNL to study the dynamics of diffusion in proton conductors that operate at high temperatures. The gas flow system (GFS) inside the furnace allows measuring temperatures up to 950°C. This system provides both humid and dry environments during the QENS experiment and also facilitates the flow of various gases.

Table 7.1: presents scattering cross-sections (Dianoux and Lander (2003)) and Bragg cut-off wavelength (Gražulis et al. (2012); Gražulis et al. (2009); Downs and Hall-Wallace (2003)) of typical materials used in sample environments.

Material	σ_{coh}	σ_{inc}	σ_{scatt}	σ_{abs}	Bragg cutt-off	Chem. compatibility with H_2O
SiO_2	10.627	0.004	10.631	0.171	8.50852	Yes
Al	1.495	0.008	1.503	0.231	4.67605	No
Pt	11.58	0.13	11.71	10.3	4.53001	Yes
Nb	6.253	0.002	6.255	1.15	4.66747	No

7.1 Design Constraints

This study is interested in quasi-elastic neutron scattering investigation of proton conductor electrolyte materials *in situ* under conditions similar to those of fuel cells. Thus, a GFS design is needed to study the proton incoherent diffusive scattering behavior. The GFS is a versatile system that can be used in any beam line for different experiments such as neutron powder diffraction (NPD), under different atmospheres, and in different temperature ranges using the appropriate sample holder material. To investigate high temperature proton conductors' dynamics by using quasielastic neutron scattering, a new gas flow sample environment system needs to be constructed and must satisfy safety regulations and guard against explosion risks.

7.1.1 Safety Regulations

The instrument design at neutron facilities coupled with the safety standards and safety regulations ensures that the instrumentation is very safe for the users, the neutron staff, the environment, and the neutron facilities. To minimize radiation from the gas flow system, a material is used that has low neutron capture cross-section, such as quartz (SiO_2), Al, Pt, Nb. Table 7.1 presents scattering length of typical materials used in sample environments.

7.1.2 Risk of tightly sealed cans exploding inside the beam

To maintain the proton inside the sample at elevated temperatures, the aluminum can is sealed tightly. Water pressure inside the sealed can increases as a function of temperature. If the sample has enough water, the can will probably explode inside the neutron beam facility. By contaminating the sample and the beam line, this explosion would seriously damage the beam line. The instrument design used at BASIS SNS located at ORNL ensures safety by having an open can inside a quartz tube that has an inlet and an exhaust opening as shown in Figure 7.1.

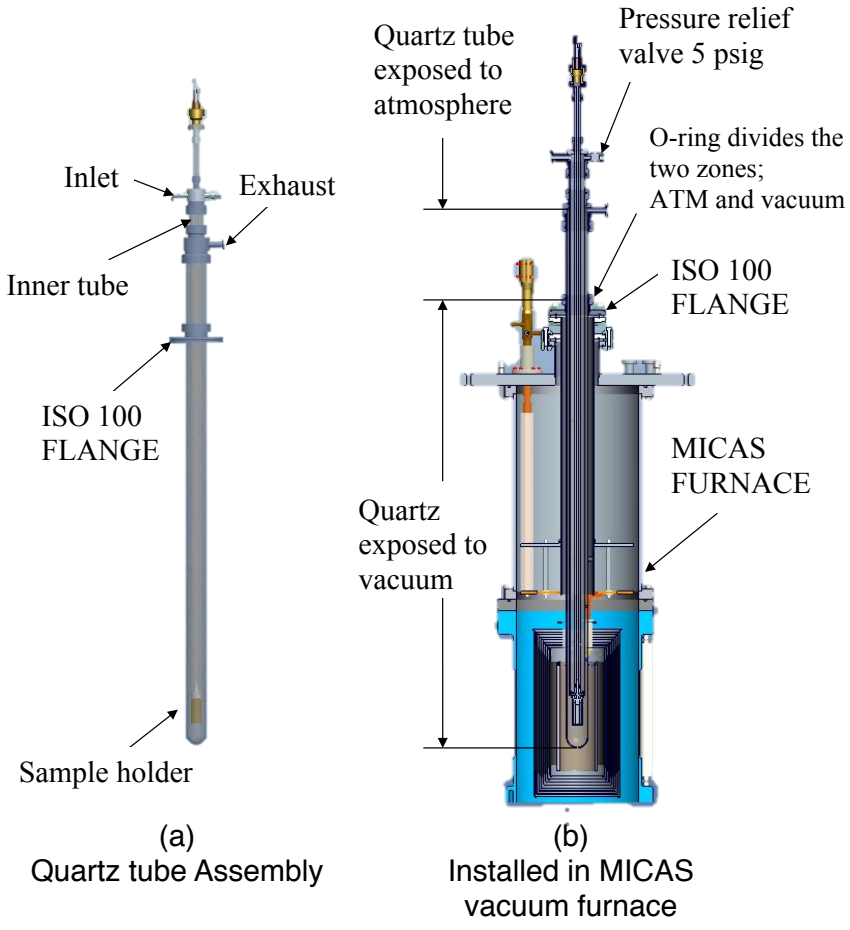


Figure 7.1: (a) The quartz tube. The Pt sample holder connected by inner quartz tube and surrounded by outer quartz tube. (b) The sample cell tube assembly installed in MICAS vacuum furnace at SNS sample environment.

7.1.3 Multiple scattering

An ideal neutron scattering experiment occurs when the neutron incident beams are scattered only once in the sample. In reality, the neutron in the beam may undergo double or multiple scattering before the neutrons depart the sample. Double scattering occurs significantly from the sample and the environment. Multiple scattering occurs within the sample, and its contribution to intensity offers no useful structural information. Instead, it is treated as a frustrating background in the total measured intensity Egami and Billinge (2012). When the sample has a high neutron scattering cross section compared to the absorption cross section, multiple-scattering is a serious problem It is also a serious problem in samples containing a large amount of hydrogen (σ_{inc}(H) = 82 barn and σ_{abs}(H) = 0.33 barns). Especially in the low Q range, multiple-scattering is high, leading to low neutron transmission Lal et al. (1994). Multiple-scattering depends on the sample's thickness and absorption. To overcome multiple-scattering problems, thinner samples are used. In a quasielastic experiment, multiple-scattering is minimized by using a sample thick enough to lead to 90% total neutron transmission. In the case of hydrate 4.2% Ca-doped $LaPO_4$, the cell density and the macroscopic cross-section are approximately 4.98 g/cm^3 and 0.431 cm^2, respectively. A sample which is approximately 0.24 cm thick ensures that 90% of the entire primary neutron beam is transmitted through the sample and sample holder. However, multiple-scattering analytical estimations and corrections are available in most data analysis programs since 1954 Mancinelli (2012); Vineyard (1954); Blech and Averbach (1965); Egami and Billinge (2012). Before obtaining the scattering factor, multiple-scattering intensity must be subtracted from the measured total intensity.

7.1.4 Materials

Aluminum (Al) has very low incoherent scattering and very weakly absorbs neutrons from the beam. (σ_{inc}(Al) = 0.0082 barn and σ_{abs}(Al) = 0.231 barns)Bée

(1988); Kharfi et al. (2006). The melting temperature of pure Al is low at 660°C, compared to other elements such as Nb and Pt whose melting points are 2477°C and 1760°C, respectively. Al works very well for QENS experiments at temperatures below 500°C. For high temperature QENS measurements, thermal stress makes Al susceptible to distortions.

Niobium (Nb) is attractive as a metal used in high temperature QENS experiments because of its high melting point (2477°C). It has a very low incoherent scattering and low thermal neutron capture cross-section (σ_{inc}(Nb) = 0.002 barn and σ_{abs}(Nb) = 1.15 barns), as well as low density (7.9 g/cm^3). Niobium does not react with noble gases, such as He and Ar. It is also highly ductile at room

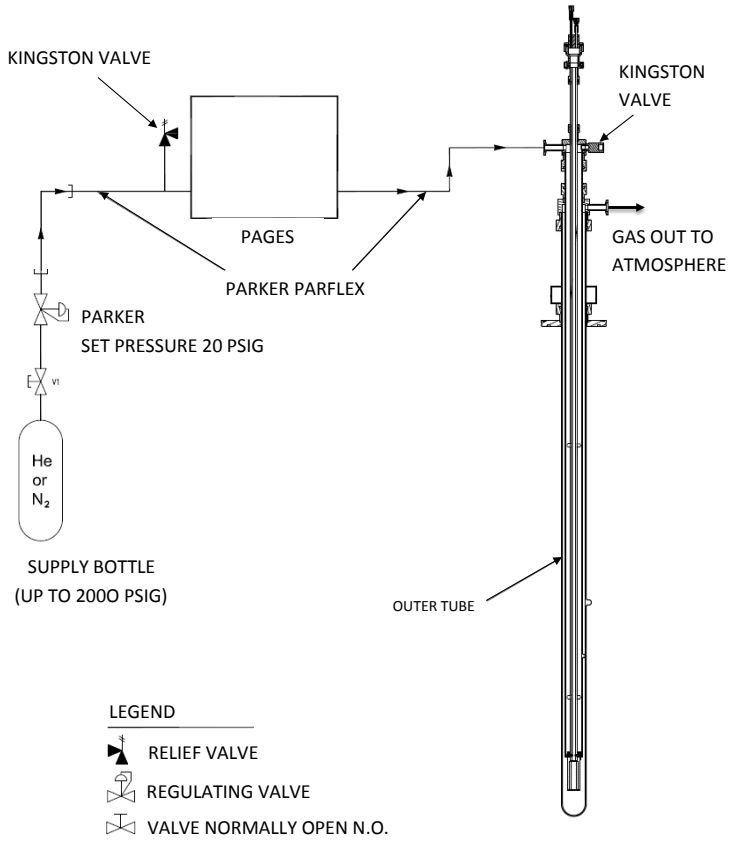


Figure 7.2: Sample cell connected to PAGES. PAGES system is designed to deliver gas to the sample cell via three separate gas channels.

temperature and has excellent formability, making it a suitable material for crucibles. Unfortunately, niobium's corrosion resistance falls with increasing temperature. In contact with water vapor, niobium reacts strongly with oxygen and with hydrogen, increasing hydrogen embrittlement. Hydrogen can easily dissolve and migrate within niobium to make the ductile niobium brittle and vulnerable to fail. In addition, at high temperatures niobium may react with construction parts such as aluminumGroß et al. (2001). For high temperature QENS experiments under humid atmospheres, Nb is not a good choice, as shown in Figure 7.3.

Platinum (Pt) is a very unreactive metal and is chemically stable. It is very resistant to corrosion, even at high temperatures. Pt does not oxidize in study environments at any temperature. Mechanically stable, it has a high temperature melting point of about 1768.3°C. It has also a low incoherent scatterer and has low absorption cross-section to the neutron beams (σ_{inc}(Pt) = 0.13 barn and σ_{abs}(Pt) = 10.3 barns). Compared to gold, silver, and copper, platinum is more ductile. A sample holder made of platinum is ideally suited to study the dynamics of proton conductor electrolytes. Platinum routinely appears as an electrocatalyst in fuel cells Feltham and Spiro (1971). Porous Pt electrodes are used for AC impedance measurements al-Wahish et al. (2014c); Bi et al. (2011)



Figure 7.3: Niobium embrittled by water

Quartz (SiO_2) has a high melting point around 1670°C. It has an extremely low incoherent scattering-cross section around $\sigma_{inc}(SiO_2) = 0.004$ barn and very low neutron absorbtion $\sigma_{abs}(SiO_2) = 0.17138$ barns. Due to its macromolecular structure and very strong Si-O bond, quartz is chemically very stable and does not react with many materials, even at relatively high temperatures. Due to these characteristics, many neutron facilities use quartz to design and build equipment.

7.2 Sample cell design for dynamics measurements of proton conductor materials

The fabricated sample apparatus for SCS was design in accordance with good vacuum practice. The contaminants that result from the fabrication and machining processes (in the form of dirt, grease, and oil) were removed using suitable solvents such as de-ionized water. Helium leak tests were performed on the setup, and the quartz tube insert was assembled into the Micas vacuum furnace. The sample cell setup showed no detectable leak greater than 10^{-7} torr $\cdot$ liters/second using MSLD. In addition, the parts were inspected using visual, dimensional, and liquid penetrant methods.

7.3 Sample holder

The attenuation coefficient is wavelength dependent. It also depends on the shape and geometry of the scattering sample, including the sample holder. To optimize the transmission factor and to obtain an isotropic multiple-scattering distributionZorn et al. (2002); Schmitt and Ouladdiaf (1998), an annular cylinder with a double-walled sample holder was used for the QENS measurements Placed inside an inner quartz tube as shown in Figure 7.4, the sample holder stands perpendicular to the scattering plane defined by the incoming and outflowing neutron beams, which are measured by the Backscattering Spectrometer (BASIS) at SNS. For low temperature measurements

($< 500°C$), the sample holder can be made from aluminum. For high temperature measurements, the sample holder is made from Platinum foil, which can be used for relatively low temperatures. The sample holder is composed of three main parts: an outer cylinder, a movable inner cylinder, and a pivotal support. The pivotal part is made from an annular cylinder with a support quartz rod inside an inner quartz tube. The annular cylinder's dimension is presented in Figure 7.4. The sample's thickness can be controlled using a cylinder with a different inner diameter. In the case of 4.2% Ca-doped $LaPO_4$, the sample thickness was about 0.25 cm to minimize multiple-scattering factors.

7.4 Sample Cell

Figures 7.1 and 7.2 show the gas flow systems created to study the proton conductor material using quasi-elastic neutron scattering under different atmospheres. All the valves, flanges, and O-rings were made from stainless steel and viton, respectively;

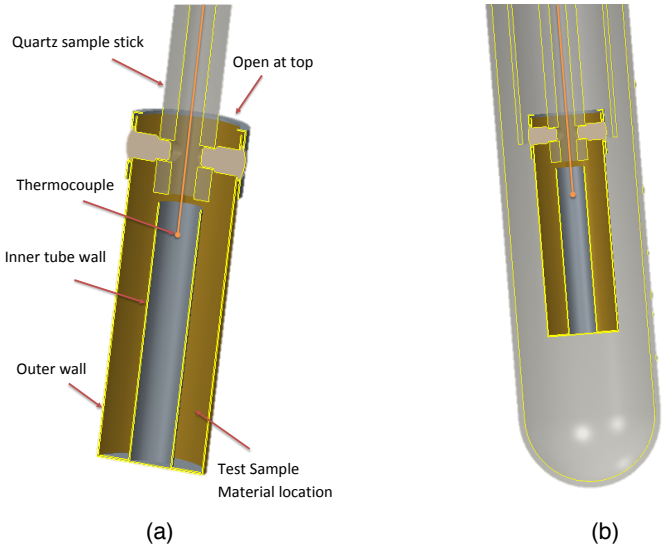


Figure 7.4: (a) The sample holder is composed of three main parts; inner Pt tube wall, Pt outer wall, and quartz sample stick. The polycrystalline sample is held in the annular cylindrical geometry can. A thermocouple is around the sample to measure the equilibrium temperatures. (b) Sample holder shown in quartz tube.

the inner and the outer tubes were made from quartz. An inlet allows the gas to flow through the inner tube and to the sample. The gas exits between the inner and outer tube. To prevent overpressure, a Kingston pressure relief valve is attached to the tube assembly. The outer quartz tube is approximately 61 inches long. The O-ring and ISO 100 flange divide the two zones: the ATM and the vacuum environment. The MICAS furnace and around 48 inches of the quartz tube are exposed to the vacuum. Heat is transferred from the MICAS furnace to the quartz tube by radiation. The sample inside the quartz tube is held in a helium exchange-gas chamber. The wet/dry He gas enters the inner quartz tube through the inlet and is delivered to the sample inside the Pt sample holder. Heat is transferred from the quartz tube to the sample by convection and radiation. The heating process is very rapid sample heating; in a few hours, the sample's temperature can reach up to 950°C. This system is very suitable for a sample in which the proton is hydrated/dehydrated quickly. For safety regulations, the quartz tube's maximum operating temperature is 1000°C. In addition, the outer tube must be replaced after two weeks of operation. One disadvantage of the gas flow system is that it can take only one sample at a time. The sample changing requires that the quartz tube and quartz stick be cooled. The quartz sample stick with the sample holder can be pulled from the quartz tube, while the inner and outer quartz tubes remain in the furnace.

7.5 Micas Furnace Generation I

Micas Furnace Gen I is a radiant heat, vacuum furnace designed and built as the Spallation Neutron Source by the sample environment development and operations teams. Micas is designed to operate at temperatures of up to 1600°C with a set of 8 nested Nb heat shields, an Nb heating element, and a high temperature center stick. After commissioning, the furnace was upgraded to run with a set of 5 nested Vanadium heat shields and a Vanadium heating element, using the same center stick. The system has a 330 Amp 20 VDC power supply which allows for a high current,

Table 7.2: General specification for Micas Furnace Generation I

Minimum temperature	RT
Maximum temperature Nb	1600°C
Maximum temperature V	1200°C
Maximum temperature with quartz insert	1000°C
Inner diameter with standard sample stick	70 mm
Inner diameter with quartz tube insert	$1.2''$
Average vacuum inside furnace	5.0×10^{-6}mbar
Thermocouple type $<$ 1200 Celsius	Type K with nickel sheath
Thermocouple type $>$ 1200 Celsius	Type W/C type (bare wire)

low voltage operation. The heating element surrounds the sample space, and as the current is applied to the element it heats up and radiates heat upon the sample. The temperature is measured close to the sample position, and the output is controlled by that temperature by a Partlow temperature controller. The Micas furnace has safety interlocks that must be within the operating parameters to operate the furnace.

Those safety interlocks are: vacuum, water flow, over temperature and emergency-stop. If any of these interlocks are out of condition, the power supply will not apply any output to the system. For this work, the Micas furnace operated with a quartz tube insert which enabled a wet and dry gas flow of he4 gas across the sample. The sample crucible was made from platinum. The quartz tube setup is made from 3 quartz tubes. The outer tube is closed at the end, and enables the furnace to operate under a vacuum while flowing a gas across the sample. The middle tube is used to flow the incoming gas, and ensuring that the gas flows across the sample, and out of the outermost tube, rather than the gas remaining at the top of the tube. The innermost quart tube is for holding the sample in place, and also houses the thermocouples, which control the temperature of the furnace. The configuration was such that the type K thermocouples were routed through the middle of the quartz center tube, and measured temperature close to the sample position. Table 7.2. lists the general specification.

7.6 Portable Automated Gas Environment (PAGES)

Figures 7.2 and 7.5 present the basic configuration of the Portable Automated Gas Environment (PAGES). The PAGES system is designed to deliver gas to the sample cell via three separate gas channels as shown in Figure 7.5. A mixture of two separate gases at a time can be delivered to the sample by using the mass flow controller (MFC). The gases are mixed prior to entering the sample environment container. Once the gases have been defined, the selected MFC option is activated. The valves required for gas flow to the sample automatically open. PAGES was designed to be controlled manually and remotely using a LabVIEW interface program. Manual system control is done by setting the solenoid valve, which controls the gas flow by using a 1000/100 SCCM mass flow controller. Using the GUI, the gas can be easily exchanged. Following the gas change, the gas correction factor for the chosen gas is automatically undated. Two Thermo CUBE recirculator water lines are connected from the CUBE to the PAGES cabinet and are labeled Humidity Cell, WATER IN, WATER OUT. The temperature controller controls the water temperature. The PAGES system

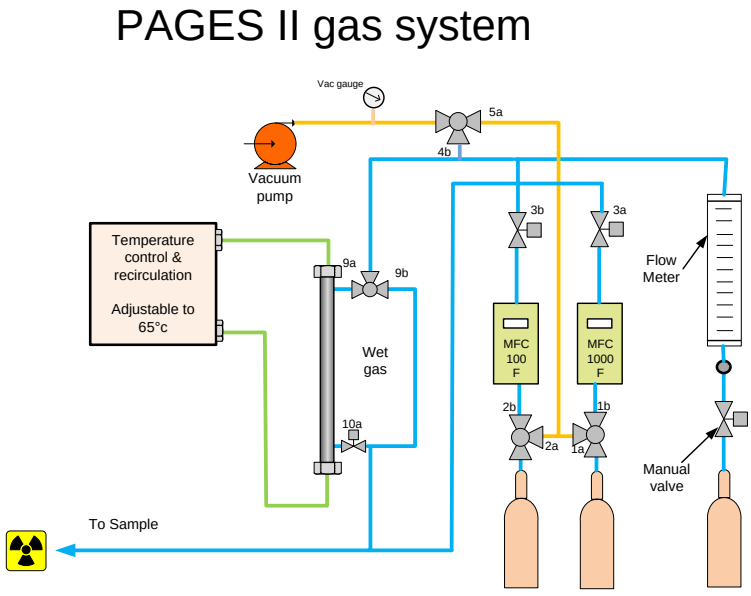


Figure 7.5: The PAGES system is connected with three separate gas channels. These channels deliver gas to the sample cell.

can deliver a gas with high relative humidity to the sample. The relative humidity is approximately 90%. When wet gas is selected, PAGES automatically select the correct valves in sequence to start the process. Approximately one hour is required to reach 90% and one hour when switching back to dry gas.

7.7 Experiment

The QENS experiments were performed using the backscattering spectrometer (BASIS) at the Spallation Neutron Source (SNS), Oak Ridge National LaboratoryMamontov and Herwig (2011). The analyzer wavelength and energy resolution at the elastic line (full width at half-maximum) were 6.267 Å and 3.4 μeV, respectively. To maintain the samples' hydration level during QENS measurements, the wet gas flow system (SCS) was used. The wet (or subsequently dry) He gas entered the inner quartz tube through the inlet and was delivered to the Pt sample holder. The average Q range for the experiments was 0.3 Å^{-1} to 1.9 Å^{-1}. For background measurement, an empty platinum can inside the flow gas system was measured at 11 temperatures between 1000°C and 150°C under dry He. To study the influence of wet/dry atmospheres on the QENS measurement, two scans were done at 150°C and 250°C under wet/dry He conditions. A QENS run for an annular Vanadium standard with 0.127 mm thick run inside the Pt can at $50°\text{C}, 35°\text{C}, 26°\text{C}$, and RT. Measured spectra were normalized to an annular Vanadium standard.

The samples' thickness and mass were calculated prior to the QENS measurement to reduce multiple neutron scattering factors. The samples can be fully hydrated or dehydrated after being inside the SCS for a certain time that depends on the sample. For example, a sample such as Lanthanum Barium Gallate can be dry and wet within a few hours ($\sim$ 2 h) (Jalarvo) The SCS is the perfect instrument for studying the proton's dynamics at elevated temperatures. If a sample, such as $La_{0.99}Ca_{0.042}PO_{3.979}$, needs more time to be charged with proton, it is recommended that the sample be hydrated by post annealing prior to the QENS experiment (Wahish). The initially

hydrated sample, $La_{0.99}Ca_{0.042}PO_{3.979}\bullet 0.021H_2O$, was heated inside the QENS sample cell at 150°C under dry gas for several hours to guarantee no water was on the sample's surface. The energy spectra were collected at different scattering angles and combined into nine groups, resulting in averaged Q values from 0.3 $Å^{-1}$ to 1.9 $Å^{-1}$. Spectra were taken at 6 temperatures between 150°C and 900°C. The sample was then fully dehydrated by purging it with dry He for 10 hours at 950°C. Spectra were again recorded at the same 4 temperatures between 150°C and 500°C in a dry He atmosphere.

7.8 Discussion

A quasi-elastic neutron scattering experiment was performed on proton conductor samples of La0.958Ca0.042PO_4, $La_{0.958}$Sr0.042PO_4, $La_{0.92}Sr_{0.08}PO_4$, and $Sn_{0.9}In_{0.1}P2O_7$ using the gas flow system described above. The nature of the samples of proton conductor materials required a sample cell system that maintains moisture at an elevated temperature inside the sample under QENS investigation. The sample holder, gas, and optical systems should be carefully considered to reduce the background intensity scattering signal. A good sample system enables the materials' dynamics to be studied without contributing to the background intensity scattering. In particular, the quasi-elastic signal from SCS needs to be very small compared to the sample signal. Figure 7.6 presents the neutron scattering intensities collected at BASIS for the quartz tube and the furnace at room temperature, empty Pt sample holder at 500°C and Vanadium inside the Pt sample holder at 35°C for $Q = 0.5$ $Å^{-1}$, it is show no clear quasi-elastic component appears. A QENS measurement was done on the SCS and the empty Pt sample holder at BASIS, for $Q = 0.3$ to 1.9 $Å^{-1}$ with 0.2 step from $T = 1000$°C to 150°C under dry He and 150°C to 250°C under wet He. Figure 7.7 shows the neutron scattering intensities for the empty sample holder in the SCS at BASIS, for $Q = 0.5, 0.7, 0.9$, and 1.3 $Å^{-1}$ from $T = 150$ to 900°C. The SCS's thermal stability is clearly shown with no clear quasi-elastic component appearing at

elevated temperatures. A Vanadium neutron scan was done inside the sample holder as a reference at RT.

The SCS was investigated under neutron scattering in two different conditions: dry He and humid He. Neutron scattering intensities were collected at BASIS for the empty Pt sample holder in the gas flow system under dry and wet He, for $Q = 0.5, 0.7, 0.9$, and 1.1 Å^{-1} at 150°C and 250°C. Figure 7.8 shows the SCS's neutron scattering intensities under dry and wet He at 250°C. As expected, the investigation showed that no difference in the neutron signal between wet and dry He with no quasi-elastic signal contribution from SCS. Figures 10 and 11 show the hydrated/dehydrated 4.2%Ca-doped $LaPO_4$ sample inside the platinum can in SCS under wet He /dry He at 250°C (for $Q = 0.5, 0.7, 0.9$, and 1.1 Å^{-1}) and at 350°C and 500°C (for $Q = 0.3$,

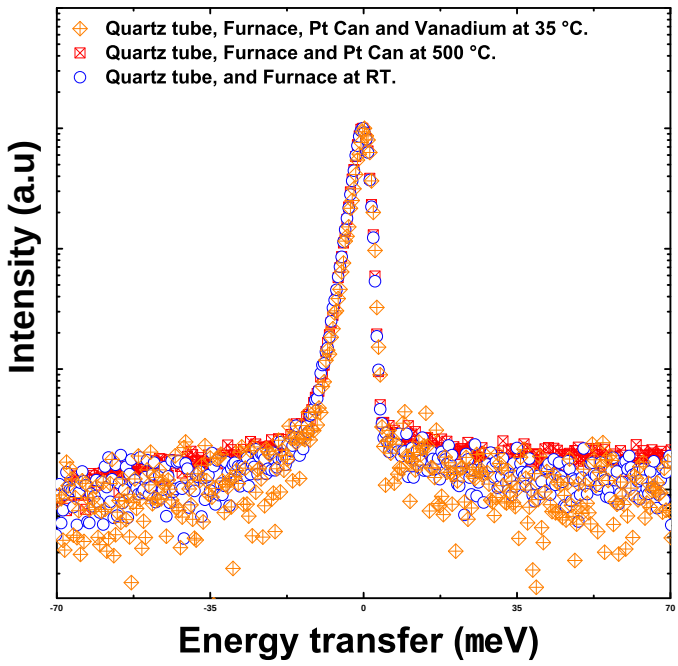


Figure 7.6: Neutron scattering intensities (log scale) collected at BASIS for the quartz tube and the furnace at room temperature, empty Pt sample holder at 500°C and Vanadium inside the Pt sample holder at 35°C for $Q = 0.5$ Å^{-1}. No clear quasi-elastic component appears.

and 0.5 Å^{-1}). The scattering function $S(Q,\omega)$ measures the number of scattered neutrons as a function of Q and ω. The hydrated sample can be separated into elastic δ-function), quasi-elastic (Lorentzian), and background contributions as shown in Figure 7.9. The quasi-elastic component broadens with increasing temperature and increasing Q, while the signal from the dehydrated sample is elastic, exhibiting no broadening beyond the instrumental resolution. Spectra of the dehydrated 4.2%Ca-doped $LaPO_4$ sample were recorded at 4 temperatures between 150°C and 500°C in a dry He atmosphere. As show in Figure 12, the dehydrated sample exhibited little or no temperature dependence beyond a slight reduction in intensity due to increased Debye-Waller vibrational motion.

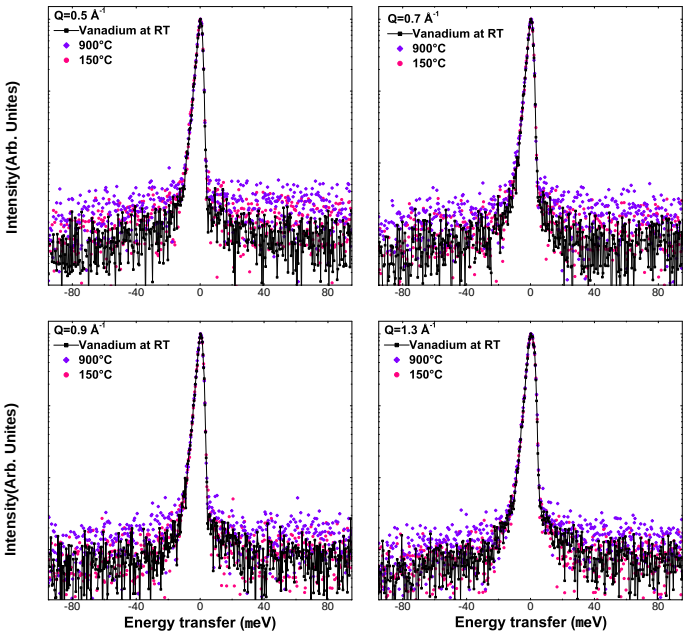


Figure 7.7: Neutron scattering intensities (linear scale) collected at BASIS for the Vanadium inside the Pt sample holder at room temperature (black line) and the empty sample holder in the gas flow system (color symbols) for $Q = 0.5, 0.7, 0.9,$ and 1.3 Å^{-1} and for the temperature window from $T = 150$ to 900°C. No clear quasi-elastic component appears. The sample holder's stability is shown at elevated temperature.

7.9 Summary

The sample cell system (SCS) presented here can be used over wide measurement ranges under different temperatures and various operating conditions, allowing chemical, dynamical, and physical changes *in situ* to be studied. Two quasi-elastic neutron scattering experiments demonstrated SCS's potential. The first experiment was done on an empty sample holder inside the SCS; the second experiment was conducted on a sample placed within the platinum sample holder inside the SCS.

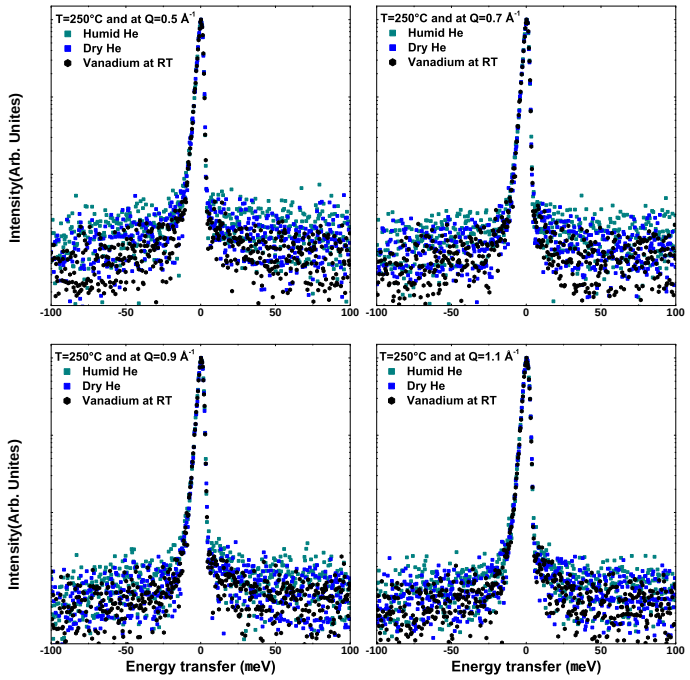


Figure 7.8: Neutron scattering intensities (linear scale) collected at BASIS for Vanadium inside the Pt sample holder at room temperature (black line) and the empty Pt sample holder in the gas flow system (color symbols) under dry and wet He, for $Q = 0.5, 0.7, 0.9$, and 1.1 Å^{-1} at 250°C. No difference is seen between wet and dry He in the neutron signal.

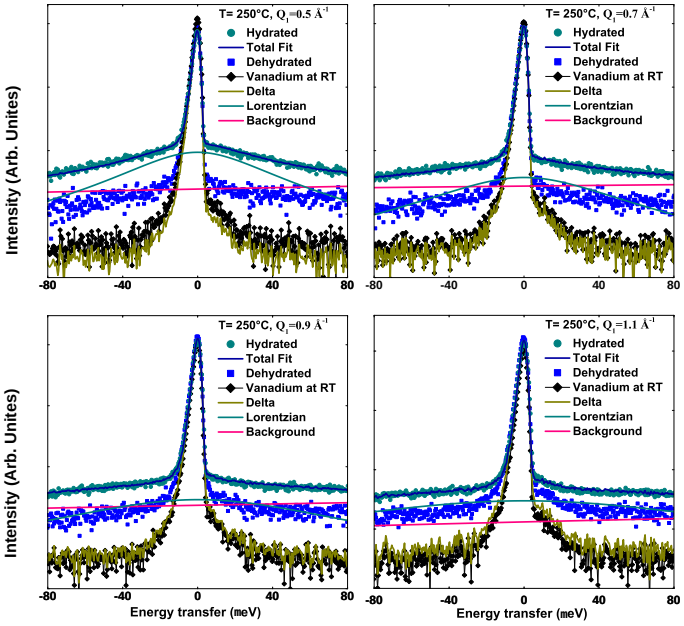


Figure 7.9: Quasielastic spectra (log scale) collected at BASIS for the Vanadium at room temperature (black symbols), the hydrated/dehydrated 4.2%Ca-doped $LaPO_4$ sample, (cyan symbols)/(blue symbols), inside the Pt sample holder in the gas flow system under humid He/Dry He, for $Q = 0.5, 0.7, 0.9$, and 1.1 Å^{-1} at 250°C. The dark-blue solid line is the total fit. The pink, golden, and cyan solid lines are background, delta, and Lorentzian components convoluted with the instrument's energy resolution function.

Chapter 8

Summary, Conclusions and Outlook

Acceptor-doped (Sr and Ca) lanthanum phosphates are attractive candidates for solid electrolytes because they combine thermal and chemical stability with good protonic conductivity. Rare earth phosphates are inexpensive, environmentally friendly, and have proton conductivity on the order 10^{-4} and 10^{-5}S/cm at 800°C for the Sr- and Ca-doped $LaPO_4$, respectively. If the proton conductivity of phosphates could be raised by 1-2 orders of magnitude, they would become viable materials for applications. In recent years, the interest in Sr- and Ca-doped $LaPO_4$ has increased because of its possible application as a high-temperature proton conductor. Most of the studies conducted by electrochemical impedance spectroscopy (EIS) and no quasi-elastic neutron scattering (QENS) experiments have been reported on these systems. The proton transport mechanisms are still poorly understood.

The present work investigated the proton dynamic of phosphate proton conductors by EIS, and QENS from 150°C to 950°C. The structure and defect structure of aliovalent (Sr, Ca) doping on $LaPO_4$ materials were investigated by X-ray diffraction (XRD) and neutron powder diffraction (NPD) from RT to 800°C.

To maintain the proton inside the sample at elevated temperatures during the QENS measurement, a new sample cell environment was designed for our QENS experiments. By using the new sample environment, an *In-situ* neutron experiments under a similar solid oxide fuel cell (SOFC) operational environment can be achieved. The instrument design's details, described in Chapter 7, are in an article that will be submitted to the Review of Scientific Instrument journal. Chapter 1, addressed this work's purposes : to study the proton dynamic properties using QENS and EIS measurements and to explore the structure and defect structure of aliovalent Sr- Ca-doped $LaPO_4$ materials using NPD and XRD; and to find a correlation between the obtained dynamic information from QENS and EIS with the structure and defect structure of the materials. Chapter one provided an overview of proton conduction in $LaPO_4$ materials, a defect structure and a brief review of experimental and theoretical studies.

Chapter 2 reviewed some of the fundamentals of neutron scattering and the characteristics of neutrons that have been described in many neutron textbooks, including Roe (2000); Squires (1978); Lovesey (1984); Bée (1988); **?**. Chapter 3 a brief review of jump diffusion models, in particular Chudley and Elliott model (CE). Chapter 4 described, comprehensive sample synthesis methods and characterization conducted by X-ray powder diffraction (XRD), scanning electron microscope (SEM), thermogravimetric analysis (TGA), electrochemical impedance spectroscopy (EIS), and neutron powder diffraction (NPD) from room temperature to 800°C applied to the samples. The QENS experiment was conducted on the 4.2% Ca-doped $LaPO_4$ sample. High phase purity polycrystalline monazite (monoclinic $LaPO_4$) and aliovalent (Sr, Ca) doping on lanthanum orthophosphate ($LaPO_4$) were conducted via conventional solid state reaction (SSR) and Co-precipitation (CPT) methods. XRD was used to study the samples for phase identification and structure refinement. SEM was used to determine the grain sizes and the samples morphology. The XRD pattern and SEM were conducted at the Center for Nanophase Materials Sciences (CNMS), User Facility at ORNL. To determine proton content, we conducted TGA was conducted for the

samples. The AC conductivity of the samples in dry and wet air was determined by EIS as function of temperature. Neutron powder diffraction (NPD) investigate the crystal structures, and determine accurate information about the atomic displacement parameters (ADPs), structural parameters, inter-atomic distances and angles between ions on the samples, and thermal expansion. Also was examined the chemical and thermal stability of the doped and undoped lanthanum orthophosphate ($LaPO_4$) samples. Time-of-flight (TOF) powder neutron diffraction data were collected using the POWGEN (BL-11A) diffractometer at the Spallation Neutron Source facility, ORNL.

As discussed in chapter 5 XRD data revealed the phase purity of the samples Ca- and Sr-doped $LaPO_4$. Monoclinic monazite $LaPO_4$ crystallizes in space group $P2_1/n$ (No.14). The crystal structure is composed of isolated PO_4 tetrahedra and La^{3+} coordination polyhedral associated with nine oxygen ions. Lack of observed impurity phases in the XRD and NPD data suggests that calcium/ strontium has been successfully doped into the lattice. The pattern was indexed according to the monoclinic structure of the parent compound $LaPO_4$ (PDF 00-032-0493) and the lattice parameters were derived from a Rietveld refinement of the data using FullProf software Carvajal (1993). The lattice parameters obtained from the XRD and NPD are consistent with and similar to those of $LaPO_4$, as expected from the similar ionic radii of the La^{3+} and Ca^{2+}/Sr^{2+} cations.

The fundamentals of proton conductivity in orthophosphate are not well understood. Doping Sr/Ca onto $LaPO_4$ creates pyrophosphate-type defects $(P_2O_7)^{\bullet\bullet}_{2PO4}$ that assists the water vapors dissociation in the unit cell and the formation of hydrogen phosphate $(HPO_4)^{\bullet}_{PO4}$. All PO_4 tetrahedra in the crystal are crystallographically equivalent, unlike the oxygen sites located at the PO_4 tetrahedra. Protons reside at PO_4 tetrahedra. Two questions were raised during this research: Are proton oxygen preference sites on the teterahedra? What are the associations between the structure defects (under dry and wet atmospheres) and proton migration?

According to Phadke et al., the presence of charged defects (oxygen vacancies or protonic defects) in a lattice can cause displacement or relaxation of the positions of the surrounding lattice ions Phadke et al. (2012). Based on the XRD and NPD data's Rietveld refinement , the following are determined the average bond of La−O, the bond length distance between two phosphorus ions (P−P), and the values of the inter-ionic bond length between phosphorus ion and oxygen ion (P−O1, P−O2, P−O3, and P−O4) compared with the ones calculated by Phadke et al. (2012) . Our initial result from XRD indicate that the proton preference site maybe at O2 $La_{0.958}Sr_{0.042}PO_4$ and $La_{0.958}Ca_{0.042}PO_4$ while for $La_{0.99}Sr_{0.01}PO_4$ and $La_{0.99}Ca_{0.01}PO_4$ the proton preference site is at O3. The NPD data show a significant increase on O2 atomic displacement parameter of the dry sample $La_{0.958}Ca_{0.042}PO_4$ relative to the hydrated sample $La_{0.958}Ca_{0.042}PO_4 \bullet nD_2O$ suggesting possible oxygen vacancies on the O2 site. From the temperature-dependent neutron diffraction on hydrated samples of $La_{0.958}Ca_{0.042}PO_4 \bullet nD_2O$ and $La_{0.958}Sr_{0.042}PO_4 \bullet nH_2O$, the thermal expansion coefficients were obtained to cell parameter.

In chapter 6, We have investigated the diffusion dynamics of protons in hydrated 4.2% Ca-doped $LaPO_4$, a candidate electrolyte for proton-conducting intermediate temperature fuel cells. The macroscopic and microscopic dynamics have been studied using electrochemical EIS and QENS, respectively. The conductivity of the hydrated sample was determined in the temperature range 500-850°C by EIS, and showed a clear signature of proton conductivity with activation energy of about 1.0 eV. The QENS experiment revealed a fast dynamical process below 500°C that was not observed by EIS. The activation energy of the fast proton diffusion is 0.09 eV in the temperature range from 150°C to 500°C. This work presents the first QENS investigation of proton dynamics in a rare earth phosphate.

This study results are correlated with some recent theoretical and computational reported studies related to the $LaPO_4$ materials. First-principles calculations have been reported on the proton diffusion network in $LaPO_4$ Toyoura et al. (2012); Yu and Jonghe (2007). Proton-transfer in the phosphate proton conductor can be described as

two dynamic processes: intratetrahedral proton-transfer and inter-tetrahedral proton-transfere. According to Yu and Jonghe (2007) calculation, the intratetrahedral energy barrier is very high around 2 eV and intratetrahedral proton transfer process rarely happens at medium temperatures. The inter-tetrahedral proton-transfer includes the following (1) oscillatory motion in which the proton can jump back and forth frequently between the same two oxygen ions on adjacent PO_4 tetrahedra with an activation energy less than 0.1 eV; (2) rotation around a tetrahedron by jumping between local energy minima surrounding a single oxygen ion on the tetrahedron with an activation energy of 0.14-0.15 eV; and (3) inter-tetrahedral hopping where the proton transfers from one PO_4 tetrahedron to another tetrahedron over a distance of about 3 Å with an activation energy near 0.9 eV Yu and Jonghe (2007).

The Q-dependent broadening of the QENS signal is consistent with that predicted by the isotropic Chudley-Elliott model describing jump diffusion. The activation energies inferred from the QENS and EIS measurements were 0.09 eV and 1 eV, respectively. Our QENS and EIS are probing fundamentally different diffusion processes. The EIS data likely reflect long-range inter-tetrahedral diffusion, whereas QENS probes more local diffusive motions that may include oscillatory jumping between adjacent tetrahedra.

Upon comparison with the QENS result and the two theoretical works on this system Toyoura et al. (2012); Yu and Jonghe (2007) good agreement was found with the predicted activation energy, but poor agreement with the predicted jump length associated with this activation energy. Additional diffusion pathways are not considered in the theoretical works likely play an important role in the proton diffusion of this system.

8.1 Outlook

Work on phosphates is an exciting and active field. This work's contributions can be starting points for many new studies and for seeking answers to unanswered questions.

Future work includes plans to study the doping of silicon in the phosphorus site; the different charge compensation may increase the oxygen vacancies which potentially increase proton concentration on the sample. Example $La_{1-x}A_xP_{1-x}Si_xO_{4-y}$, where A = Sr, Ca, Ba, and Mg.

Another investigation would be to study the proton dynamic in phosphates in single-crystal form. With careful orientation of samples in the neutron beam, the quasielastic signal will provide directional information on the motion of the protons, in turn providing key information on the mechanism by which protons migrate between PO_4 tetrahedra.

Yet another interesting study would focus on the correlation between the thermal expansion of proton conductor $LaPO_4$ and the hydrogen bond network. The hydrogen bond indirectly plays an important role to the proton long range diffusion. Understand why the orientation or reorientation of the proton step is missing from the QENS experiment of the $LaPO_4$ materials. Investigate the intra-tetrahedral transfers and find explanation why the activation energy is very high?

One more direction concerns the dynamics in newberyite ($MgHPO_4 \bullet_3 H_2O$), $SrHPO_4$ and $BaHPO_4$ by quasi-elastic neutron scattering (the data collection and the data analysis have already been completed and a clear result is expected soon).

Finally, since the proton and neutron are fermions it would be very interesting to study the spin diffusion dynamic, the exchange between the proton spin and neutron spin, and to compare that with other techniques such as NMR and QENS spin echo. Such a study would potentially provide accurate information about the crystal structure and dynamics.

Bibliography

Adelstein, N., Neaton, J. B., Asta, M., and De Jonghe, L. C. (2012). First-principles studies of proton-Ba interactions in doped LaPO4. *Journal of Materials Chemistry*, 22(9):3758. 7, 68

al-Wahish, A., Armitage, D., Hill, B., al-Binni, U., Mills, R., Jalarvo, N., Mandrus, D., and Herwig6, K. W. (2014a). Sample cell systems for quasi-elastic neutron scattering instrument design at basis sns. *(submitted to Review of Scientific Instruments)*. 34

al-Wahish, A., Bridges, C., al-Binni, U., Bi, Z., Tang, S., Paranthaman, M. P., Huq, A., and Mandrus, D. (2014b). Neutron scattering and electrochemical impedance spectroscopy investigation of proton diffusion in sr/ca-doped lapo4. *(in preparation)*. 78

al-Wahish, A., Jalarvo, N., Bi, Z., Herwig, K. W., Bridges, C., Paranthaman, M. P., and Mandrus, D. (2014c). Quasi-elastic neutron scattering reveals fast proton diffusion in ca-doped lapo4. *Journal of Physical Chemistry C*. 87

Amezawa, K., Maekawa, H., Tomii, Y., and Yamamoto, N. (2001). Protonic conduction and defect structures in Sr-doped LaPO4. *Solid State Ionics*, 145(1-4):233–240. 6, 9, 42, 43, 67

Amezawa, K., Tomii, Y., and Yamamoto, N. (2005). High temperature protonic conduction in sr2p2o7–lapo4 system. *Solid State Ionics*, 176(1-2):135–141. 2, 7, 29, 30, 57, 59, 61

Azuah, R., Kneller, L., Qiu, Y., Tregenna-Piggott, P., Brown, C., Copley, J., and Dimeo, R. (2009). DAVE: A comprehensive software suite for the reduction, visualization, and analysis of low energy neutron spectroscopic data. *J. Res. Natl. Inst. Stan.*, 114:341. 36, 65

Bée, M. (1988). *Quasielastic neutron scattering*. Adam Hilger. 10, 85, 100

Bée, M. and Mol, L. D. B. (2003). Localized and long-range diffusion in condensed matter: state of the art of QENS studies and future prospects. *Chemical Physics*, 292(2-3):121–141. 73

Bi, Z., Bridges, C. a., Kim, J.-H., Huq, A., and Paranthaman, M. P. (2011). Phase stability and electrical conductivity of Ca-doped LaNb1xTaxO4δ high temperature proton conductors. *Journal of Power Sources*, 196(18):7395–7403. 33, 64, 87

Blech, I. A. and Averbach, B. L. (1965). Multiple scattering of neutrons in vanadium and copper. *Phys. Rev.*, 137:A1113–A1116. 85

Boatner, L. a. (2002). Synthesis, Structure, and Properties of Monazite, Pretulite, and Xenotime. *Reviews in Mineralogy and Geochemistry*, 48(1):87–121. 29, 37

Braun, A., Duval, S., Ried, P., Embs, J., Juranyi, F., Strässle, T., Stimming, U., Hempelmann, R., Holtappels, P., and Graule, T. (2009). Proton diffusivity in the BaZr0.9Y0.1O3δ proton conductor. *Journal of Applied Electrochemistry*, 39(4):471–475. 2, 62

Burggraaf, A. J. and Cot, L., editors (1996). *Fundemantals of Inorganic Memebrane*. Mebrane Science and Technology series. Elsevier B.V. 1

Bychkov, E., Price, D. L., and Lapp, A. (2001). Universal trend of the Haven ratio in glasses : origin and structural evidences from neutron di raction and small-angle neutron scattering. 295:211–219. 58

Carvajal, J. R. (1993). Recent advances in magnetic structure determination by neutron powder diffraction. *Physica B*, 192:55–69. 34, 38, 66, 101

Chathoth, S. M., Mamontov, E., Kolesnikov, a. I., Gogotsi, Y., and Wesolowski, D. J. (2011). Quasielastic neutron scattering study of water confined in carbon nanopores. *EPL (Europhysics Letters)*, 95(5):56001. 22, 24

Chudley, C. T. and Elliott, R. J. (1961). Neutron Scattering from a Liquid on a Jump Diffusion Model. *Proc. Phys. Soc.*, 77:353–361. 22, 25, 74

Cukierman, S. (2006). *Biochim. Biophys. Acta*, 1757:876–885. 2, 61

Dianoux, A.-J. and Lander, G., editors (2003). *Neutron Data Booklet*. Institut Laue-Langevin. xii, 83

Downs, R. T. and Hall-Wallace, M. (2003). The american mineralogist crystal structure database. *American Mineralogist*, 88:247–250. xii, 83

Egami, T. and Billinge, S. J. (2012). *Underneath the Bragg Peaks: Structural Analysis of Complex Materials*. Pergamon Materials Series. 85

Embs, J. P., Juranyi, F., and Hempelmann, R. (2010). Introduction to Quasielastic Neutron Scattering. *Zeitschrift für Physikalische Chemie*, 224(1-2):5–32. 10, 22

et al., B. G. (2009). *Solid State Ionics*, 145(325). 2

Feltham, A. M. and Spiro, M. (1971). Platinized platinum electrodes. *Chemical Reviews*, 71(2):177–193. 87

Fitter, J., Gutberlet, T., and Katsaras, J. (2006). *Neutron Scattering in Biology: Techniques and Applications*. 22, 26

Gallini, S., Jurado, J. R., and Colomer, M. T. (2005). Synthesis and characterization of monazite-type Sr:LaPO prepared through coprecipitation. *Journal of the European Ceramic Society*, 25(12):2003–2007. 30

Gražulis, S., Chateigner, D., Downs, R. T., Yokochi, A. F. T., Quirós, M., Lutterotti, L., Manakova, E., Butkus, J., Moeck, P., and Le Bail, A. (2009). Crystallography Open Database – an open-access collection of crystal structures. *Journal of Applied Crystallography*, 42(4):726–729. xii, 83

Gražulis, S., Daškevič, A., Merkys, A., Chateigner, D., Lutterotti, L., Quirós, M., Serebryanaya, N. R., Moeck, P., Downs, R. T., and Le Bail, A. (2012). Crystallography open database (cod): an open-access collection of crystal structures and platform for world-wide collaboration. *Nucleic Acids Research*, 40(D1):D420–D427. xii, 83

Groß, B., Beck, C., Meyer, F., Krajewski, T., Hempelmann, R., and Altgeld, H. (2001). Bazr0.85me0.15o2.925 (me=y, in and ga): crystal growth, high-resolution transmission electron microscopy, high-temperature x-ray diffraction and neutron scattering experiments. *Solid State Ionics*, 145(1–4):325 – 331. Proceedings of the 10th International Conference on Solid State Protonic Conductors. 87

Haile, S. M., Boysen, D. a., Chisholm, C. R., and Merle, R. B. (2001). Solid acids as fuel cell electrolytes. *Nature*, 410(6831):910–913. 1, 60

Hall, P. L. and Ross, D. (1981). Incoherent neutron scattering functions for random jump diffusion in bounded and infinite media. *Molecular Physics*, 42(3):673–682. 22, 28

Harley, G. and De Jonghe, L. C. (2010). Proton transport in doped La-metaphosphate glasses. *Solid State Ionics*, 181(8-10):424–429. 58

Hatada, N., Nose, Y., Kuramitsu, A., and Uda, T. (2011). Precipitation behavior of highly Sr-doped LaPO4 in phosphoric acid solutions. *Journal of Materials Chemistry*, 21(24):8781. 30, 68

Hempelmann, R. (1996). Hydrogen diffusion mechanism in proton conducting oxides. *Physica B: Condensed Matter*, 226(1–3):72 – 77. 62

Hempelmann, R. (2000). *Quasielastic Neutron Scattering and Solid State Diffusion*. Clarendon Press. 10, 73

Hikichi, Y. and Nomura, T. (1987). Melting temperatures of monazite and xenotime. *J. Am. Ceram. Soc.*, 70(10):C–252–C–253. 37, 65

Ishikawa, a., Maekawa, H., Yamamura, T., Kawakita, Y., Shibata, K., and Kawai, M. (2008). Proton dynamics of CsH2PO4 studied by quasi-elastic neutron scattering and PFG-NMR. *Solid State Ionics*, 179(40):2345–2349. 82

Jalarvo, N., Gourdon, O., Bi, Z., Gout, D., Ohl, M., and Paranthaman, M. P. (2013a). Atomic-Scale Picture of the Ion Conduction Mechanism in a Tetrahedral Network of Lanthanum Barium Gallate. *Chemistry of Materials*, 25(14):2741–2748. 62, 82

Jalarvo, N., Stingaciu, L., Gout, D., Bi, Z., Paranthaman, M. P., and Ohl, M. (2013b). Proton dynamics in La0.8Ba1.2GaO3.9nH2O studied by quasielastic incoherent neutron scattering. *Solid State Ionics*, 252:12–18. 62, 82

Karlsson, M., Engberg, D., Björketun, M. E., Matic, A., Wahnström, G., Sundell, P. G., Berastegui, P., Ahmed, I., Falus, P., Farago, B., Börjesson, L., and Eriksson, S. (2010). Using Neutron SpinEcho To Investigate Proton Dynamics in Proton-Conducting Perovskites . *Chemistry of Materials*, 22(3):740–742. 3, 62

Karlsson, M., Matic, A., Engberg, D., Björketun, M. r. E., Koza, M. M., Ahmed, I., Wahnström, G., Börjesson, L., and Eriksson, S.-G. (2009). Quasielastic neutron scattering of hydrated BaZr0.90A0.10O2.95 (A=Y and Sc). *Solid State Ionics*, 180(1):22–28. 2, 62, 82

Karmonik, C., Hempeimann, R., Cook, J., Giithoff, F., Saarlandes, U., and Langevin, L. (1996). F (Q) = I (l + sin (Qd) ˜ Qd. 2:69–74. 2

Karmonik, C., Matzke, T., Cappadonia, M., Stimming, U., Hempelmann, R., Springer, T., Adams, M. A., and Ch. Karmonik , Th. Matzke , M. Cappadonia , U. Stimming , T. Springer, M. A. . (1995). SOLID lows Quasielastic neutron scattering study of proton diffusion. *Solid State Ionics*, 77(94):152–156. 2, 62

Kharfi, F., Bastuerk, M., and Boucenna, a. (2006). Characterization of weak, fair and strong neutron absorbing materials by means of neutron transmission: Beam hardening effect. *Nuclear Instruments and Methods in Physics Research Section A:*

Accelerators, Spectrometers, Detectors and Associated Equipment, 565(2):416–422. 86

Kim, S.-h., Fu, Z., Niihara, K., and Lee, S.-w. (2011). Processing Research Characterization of 3YSZ / LaPO 4 composites coatings made by an atmospheric plasma spraying method. 12(2):126–131. 37

Kitamura, N., Amezawa, K., Tomii, Y., Hanada, T., Yamamoto, N., Omata, T., and Otsuka-Yao-Matsuo, S. (2005). Electrical Conduction Properties of Sr-Doped LaPO[sub 4] and CePO[sub 4] under Oxidizing and Reducing Conditions. *Journal of The Electrochemical Society*, 152(4):A658. 9

Kreuer, K. (2003). Proton -c onducting oxides. *Annual Review of Materials Research*, 33(1):333–359. 2, 5

Kreuer, K., Paddison, S. J., Spohr, E., and Schuster, M. (2004). *Chem. Rev.*, 104:4637– 4678. 2, 61

Lal, J., Widmaier, J. M., Bastide, J., and Boue, F. (1994). Determination of an interpenetrating network structure by small-angle neutron scattering. *Macromolecules*, 27(22):6443–6451. 85

Lechner, R. E. (1983). *Mass Transport in Solids*. Plenum Press, New York. 10

Lovesey, S., W. (1984). *Theory of Neutron scattering from Condensed Matter*. Oxford Science Publications. 10, 100

Malavasi, L., Fisher, C. a. J., and Islam, M. S. (2010). Oxide-ion and proton conducting electrolyte materials for clean energy applications: structural and mechanistic features. *Chemical Society reviews*, 39(11):4370–87. 1, 60

Mamontov, E. and Herwig, K. W. (2011). A time-of-flight backscattering spectrometer at the spallation neutron source, basis. *Review of Scientific Instruments*, 82(8):–. 35, 64, 93

Mamontov, E., Luo, H., and Dai, S. (2009). Proton dynamics in N,N,N',N'-Tetramethylguanidinium Bis(perfluoroethylsulfonyl)imide protic ionic liquid probed by quasielastic neutron scattering. *The journal of physical chemistry. B*, 113(1):159–69. 2

Mancinelli, R. (2012). Multiple neutron scattering corrections. Some general equations to do fast evaluations. *Journal of Physics: Conference Series*, 340:012033. 85

Matsuda, M. (2004). Influences of ga doping on lattice parameter, microstructure, thermal expansion coefficient and electrical conductivity of la0.6sr0.4coo3y. *Solid State Ionics*, 172(1-4):57–61. 49

Matzke, T., Stimming, U., Karmonikh, C., Soetratmo, M., Hempelmann, R., and Giithoff, F. (1996). Quasielastic Thermal Neutron Scattering Experiment on the Proton Conductor SrCe0.95Yb0.05H0.02O2.985. *Solid State Ionics X6-88*, 86-88(96):621–628. 2, 14, 62

Mogilevsky, P., Boakye, E. E., and Hay, R. S. (2007). Solid solubility and thermal expansion in a lapo4–ypo4 system. *Journal of the American Ceramic Society*, 90(6):1899–1907. 37

Morgan, P. E. D. and Marshall, D. B. (1995). Ceramic Composites of Monazite and Alumina. *Journal of the American Ceramic Society*, 78(6):1553–1563. 49

Norby, T. (2001). The promise of protonics. *Nature*, 410(6831):877–8. 9

Norby, T. and Christiansen, N. (1995). *Solid State Ionics*, 77:240–243. 2, 4, 6, 57, 59, 61

Phadke, S., Nino, J. C., and Islam, M. S. (2012). Structural and defect properties of the LaPO4 and LaP5O14-based proton conductors. *Journal of Materials Chemistry*, 22(48):25388. xiv, 1, 42, 43, 44, 60, 102

Phadke, S. R. and Nino, J. C. (2011). Conductivity Enhancement in Lanthanum Phosphates. *Journal of the American Ceramic Society*, 94(6):1817–1823. 43

Pionke, M., Mono, T., Schweika, W., Springer, T., and Schober, H. (1997). Investigation h mobility by qens. 2, 62

Roe, R.-J. (2000). *Methods of X-ray and Neutron Scattering in Polymer Science*. Oxford University Press. 10, 22, 100

Sata, N., Hiramoto, K., Ishigame, M., Hosoya, S., Niimura, N., and Shin, S. (1996). Site identification of protons in SrTiO3: Mechanism for large protonic conduction. *Physical review. B, Condensed matter*, 54(22):15795–15799. 5

Scharfenberger, G., Meyer, W. H., Wegner, G., Schuster, M., Kreuer, K.-D., and Maier, J. (2006). Anhydrous Polymeric Proton Conductors Based on Imidazole Functionalized Polysiloxane. *Fuel Cells*, 6(3-4):237–250. 58

Schatzmann, M. T., Mecartney, M. L., and Morgan, P. E. D. (2009). Synthesis of monoclinic monazite, LaPO4, by direct precipitation. *Journal of Materials Chemistry*, 19(32):5720. 65

Schmitt, D. and Ouladdiaf, B. (1998). Absorption Correction for Annular Cylindrical Samples in Powder Neutron Diffraction. *Journal of Applied Crystallography*, 31(4):620–624. 88

Shin, S. and Crystal, S. (1990). ˜ B. 41:910–913. 5

Singh, B. P., Baghel, V. S., and Baghel, K. S. (2009). Electronegativity , fractional ionic character and refractive index of binary compounds. 47(November):793–803. 50

Singwi, K. S. and Sjölander, A. (1960). Resonance Absorption of Nuclear Gamma Rays and the Dynamics of Atomic Motions. 120(4). 22, 27

Solomon, J. M., Adelstein, N., De Jonghe, L. C., and Asta, M. (2014). First principles study of pyrophosphate defects and dopant–defect interactions in stronium-doped lanthanum orthophosphate. *Journal of Materials Chemistry A*, 2(4):1047. 42, 43

Squires, G., L. (1978). *Introduction to the Theory of Thermal Neutron Scattering.* Cambridge University Press. 10, 100

Stanguennec, M. L. and Elliott, S. R. (1994). Frequency-dependent ionic conductivity in AgI-AgP03 glasses. 73(94):199–208. 56

Steele, B. C. and Heinzel, a. (2001). Materials for fuel-cell technologies. *Nature*, 414(6861):345–52. 1

Toyoura, K., Hatada, N., Nose, Y., Tanaka, I., Matsunaga, K., and Uda, T. (2012). Proton-Conducting Network in Lanthanum Orthophosphate. *The Journal of Physical Chemistry C*, 116(36):19117–19124. 7, 42, 61, 81, 102, 103

Tuckerman, M. E., Marx, D., Klein, M. L., and Parrinello, M. (1997). *Science*, 275:817–820. 2, 61

Vineyard, G. H. (1954). Multiple scattering of neutrons. *Phys. Rev.*, 96:93–98. 85

Vuilleumier, R., Borgis, and D. (1998). *Chem. Phys. Lett.*, 284:71–77. 2, 61

Wilmer, D., Seydel, T., and Kreuer, K.-D. (2007). Proton diffusion in hydrated acceptor-doped barium zirconate. *Materials Research Society Symposium Proceedings*, 972:15–20. 2

Yu, R. and Jonghe, L. C. D. (2007). Proton-Transfer Mechanism in LaPO 4. pages 11003–11007. xiii, 7, 8, 42, 61, 81, 102, 103

Zorn, R., Frick, B., and Fetters, L. J. (2002). Quasielastic neutron scattering study of the methyl group dynamics in polyisoprene. *The Journal of Chemical Physics*, 116(2):845. 88

Vita

Amal al-Wahish was born in Amman, Jordan to Palestinian parents residing in Jordan. She grew up in Jordan and earned her Bachelors degree (1999) and Masters degree (2003) in Physics from the Hashmite University (Jordan), and subsequently worked as a lab instructor at the University of Jordan (2003-2005).

In 2007 she enrolled in the physics graduate program at the University of Tennessee, and in 2010 joined the research group of David Mandrus who became her PhD advisor. Her doctoral research focused on the investigation of the dynamics of proton conductors. Amal al-Wahish successfully defended her dissertation in condensed matter physics in the Summer of 2014.